Constitutive and Fracture Characterization of High Strength Aluminum Alloys at Low and Elevated Strain Rates

by

M. Taamjeed Rahmaan

A thesis
presented to the University of Waterloo
in fulfillment of the
thesis requirement for the degree of
Doctor of Philosophy
in
Mechanical and Mechatronics Engineering

Waterloo, Ontario, Canada, 2022

EXAMINING COMMITTEE MEMBERSHIP

The following served on the Examining Committee for this thesis. The decision of the Examining Committee is by majority vote.

Supervisors	Michael J. Worswick, Ph.D.
	Professor, University of Waterloo
	Cliff Butcher, Ph.D.
	Assistant Professor, University of Waterloo
External Examiner	Yannis P. Korkolis, Ph.D.
	Associate Professor, The Ohio State University
Internal Examiner	Kyle J. Daun, Ph.D.
	Professor, University of Waterloo
Internal Examiner	John Montesano, Ph. D.
	Associate Professor, University of Waterloo
Internal-External Examiner	Scott Walbridge, Ph.D.
	Professor, University of Waterloo

AUTHOR'S DECLARATION

This thesis consists of material all of which I authored or co-authored: see Statement of Contributions included in the thesis. This is a true copy of the thesis, including any required final revisions, as accepted by my examiners. I understand that my thesis may be made electronically available to the public.

STATEMENT OF CONTRIBUTIONS

The following co-authors have contributed to the current work:

Professor Michael J. Worswick and Professor Cliff Butcher supervised this Ph.D. thesis.

Professor Cliff Butcher developed the original user material subroutine (UMAT), which was modified in this work.

Professor Kyle Daun advised on the development of the methodology to capture temperature rise on the specimen surface at elevated strain rate testing.

Dr. Armin Abedini assisted in the yield function calibrations.

Dr. Ping Zhou assisted in preparing the high strain rate specimens and performing elevated strain rate fracture tests.

Samuel Kim provided the component-scale crash test data and assisted in the crash simulation development.

Sante DiCecco provided the Nakazima dome test data for the AA6013-T6 and AA7075-T6.

The balance of the research is my own work.

ABSTRACT

The present research investigates the constitutive and fracture behavior of three high strength automotive aluminum sheet alloys, AA6013-T6, AA7075-T6, and AA7xxx-T6 under quasi-static and elevated strain rate conditions. The constitutive characterization included room temperature uniaxial tensile tests along seven orientations (0°, 15°, 30°, 45°, 60°, 75°, and 90°) with respect to the rolling direction along with shear and through-thickness compression. The three alloys exhibited significant plastic anisotropy in terms of the measured r–values, while relatively low anisotropy of the stress response. As part of this research, a novel methodology was developed to experimentally characterize the isotropic hardening response to large strains using tensile and shear specimens. Elevated strain rate tensile and shear tests were performed at strain rates spanning 0.001 to 500 s^{-1} with mild positive rate sensitivity observed in each material. The influence of strain rate on the in-plane plastic anisotropy, in terms of the flow stress ratios and r–values, was low. High speed infrared imaging was used to measure temperature rise of up to 40 °C during the elevated rate tests to aid in the modelling of thermal softening on fracture. A phenomenological strain rate and temperature dependent Hockett–Sherby (HS-SRT) constitutive model was developed and shown to accurately capture the hardening behavior. The evaluation of multiple yield functions was performed to select an appropriate one. The Barlat YLD2004 yield function with an associated flow rule was calibrated and accurately captured the anisotropic plasticity response for the range of loading conditions. Quasi-static fracture characterization tests were performed under stress states ranging from shear to equal-biaxial tension for the three alloys. It was observed that all three alloys exhibited appreciable dependency on the stress state, while the ductility found to be lowest in the plane strain stress state. The AA6013-T6 alloy displayed the greater ductility among all three alloys tested, while ductility was lowest for AA7075-T6. A *generalized Drucker-Prager (GDP)* stress state dependent fracture model is proposed that overcomes limitations associated with the Hosford-Coulomb (HC) fracture model (the GDP model admits different fracture limits in uniaxial versus biaxial tension whereas the HC model does not). The calibrated fracture *loci* using the generalized Drucker-Prager (GDP) fracture function exhibited good agreement with the experimental data. The force–displacement and absorbed energy of a structural hat channel section in a three-point bend test was accurately predicted in the simulations conducted using the experimentally-derived fracture *loci* regularized with the biaxial dome test. The effect of strain rate on the fracture strain was characterized for one of the alloys, AA7075-T6, using micro-shear, hole tension, notch tension, and groove tension specimens, at strain rates ranging from 0.01 to 500 s^{-1}. The effect of strain rate on fracture was mild. The ductility for the shear, hole tension, and notch specimens decreased by 5% between strain rates of 0.01 and 10 s^{-1}, but

recovered by 4% for shear specimens and 3% for hole tension and notch tension specimens. A minimal strain rate effect on the fracture strain was observed for the groove tension specimen. Since hole tension, notch tension, and groove tension specimens exhibited through-thickness necking prior to fracture, the fracture strains at the mid-plane of the samples were obtained using hybrid experimental–numerical finite element (FE) modelling. The GDP fracture model was modified to incorporate strain rate sensitivity and was calibrated to the high strain rate fracture tests. FE simulations incorporating the proposed strain rate dependent generalized Drucker-Prager (GDP) fracture model accurately captured the experimental data over the studied range of strain, strain rates, and stress states for the AA7075-T6 sheet alloy.

ACKNOWLEDGEMENTS

friend and continuously helping with the conceptual matters of solid mechanics and many other things. The prompt administrative support from L. Wilfong is much appreciated. The work environment was always helpful and friendly with Amir, Cam T., Hossein, Khizar, Kenneth, Farinaz, Farzad, Negar, Chi, and everybody else around, thanks guys.

Finally, I would like to thank my family. Abbu, as I'm growing up I understand even more how tough your life has been, and how you still ensured an incredibly comfortable and privileged life for us. You taught me how to become humble and I can only wish to reach the height of success that you have achieved in an honest way. Ammu, you are the strength and sustenance of my life. I have seen you tackle the toughest challenges so easily which taught me how to deal with difficulties cleverly. Your unconditional love and guidance are the only reasons I have come this far. You made me, all I am, and all I'll ever be is because of you. Baba, if it weren't for you and your constant motivation, I would have given up a long time ago. The remarkable success you have achieved through your consistent determination, integrity, innovative mindset, passion for growing, endless energy, and kind-heartedness is a genuine inspiration for me to take on new challenges and work really hard to make this world a better place. Maa, you are the most patient and forgiving person I have seen. Your patience and perseverance encourages me to stay calm in difficult times and taught me how to accomplish. I am truly blessed to have your true love and prayer with me. Mamu, you are the most talented, intelligent, and brilliant one in our family, you have me right by your side all your life no matter what. Buin–Dula, I am never afraid to fall because of you. You are my guardian angels, no matter what I did, I could never be wrong in your eyes and you never left my side. You provided me with the support to grow as a confident individual. Sebring–Brother Riz, you inspire me to get back up after a downfall. I get motivated by seeing you defying the odds, and sometimes I wish I could be like you. Last but not least, my lovely wife, if anyone shared this journey with me, it's you. Your love, support, and endurance gives me the courage to aim for the highest without any fear. Your goodness inspires me to be a good human being. You always bring the best out of me. I dare to dream only because I know you are there with me through every thick and thin. We do not choose our family, it is a gift from the God, and I feel incredibly fortunate to have you all in my life.

DEDICATION

To my wonderful and loving family:

Jesmin Rahman, Dr. Lutfor Rahman, Maleka Azim, Engr. Syed A. Reza

Tania Rahman, Raisul Islam, Raisa Tasnia

Sabrin Reza, Rizwanur Rahman

and

Tasnim Reza

TABLE OF CONTENTS

LIST OF FIGURES

LIST OF TABLES

CHAPTER 1: INTRODUCTION

The overall weight of passenger vehicles is increasing with the integration of modern safety and comfort features such as collision safety, self-driving technology, pedestrian protection, infotainment systems and demands for larger interior space. This trend runs at odds with the need to reduced vehicle weight which is identified as one of the most effective means to meet current legislations to increase fuel efficiency and reduce vehicle emissions. It has been reported that for every one hundred kilograms of vehicle weight reduction, there is a corresponding decrease in fuel consumption by 1 km/L with a commensurate reduction of 9 grams of CO_2 emissions per kilometer (Heuss *et al.*, 2012; Sakurai, 2008). Traditionally, advanced lightweight, high strength metal alloys are used within automotive structures and body panels to achieve vehicle weight reduction, while maintaining crash performance and strength. High strength aluminum alloys (such as 6000- and 7000-series aluminum alloys) can provide a higher level of specific strength as compared to conventional high strength steels (US Department of Energy, 2015). A number of vehicle manufacturers have successfully used aluminum alloys in different parts of their commercial vehicles. Examples of the use of aluminum alloys in vehicles are shown in Figure 1. In order to further increase the application of high strength aluminum alloys within the automotive industry, proper understanding of material response under different loading and strain rate conditions is required.
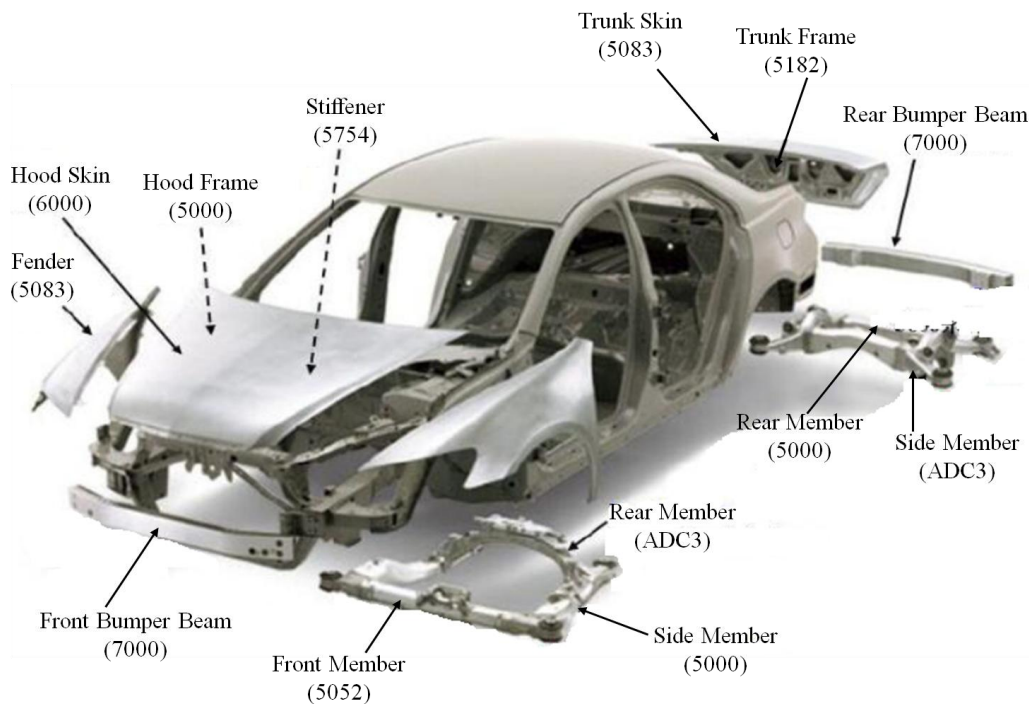
Figure 1: Example of aluminum alloy parts used in a vehicle (Everychina.com, 2021).

During a typical automobile crash event, the rates of strain within structural sheet alloy components are typically on the order of 10^2 s^{-1}, while hinge points and folds locally experience strain rates as high as 10^3 s^{-1} (Salisbury *et al.*, 2006). Most metals exhibit an increase in flow stress (strength) at elevated strain rates. Furthermore, at larger strains and strain rates, thermal softening induced by deformation heating plays an important role in the constitutive and fracture characteristics of materials (Erice *et al.*, 2018; Rittel *et al.*, 2017; Roth and Mohr, 2014). Therefore, it is important to understand the low (10^{-3} – 10^0 s^{-1}), intermediate (10^1 – 10^2 s^{-1}), and high (10^3 s^{-1}) strain rate behavior of aluminum sheet metals in order to develop accurate constitutive models for the simulation of metal forming processes and in-service dynamic loading such as during vehicle crash. In addition, models predicting the onset of fracture at these rates of strain are also required to avoid catastrophic failure of automotive structures during crash events. The fracture strain of a material is typically characterized in terms of the limit strain as a function of stress state, which can be expressed using the combination of the stress triaxiality and Lode parameter. There exist several experimental procedures and specimen geometries to obtain the fracture strains at different stress states but these are primarily limited to quasi-static (low) strain rate conditions.

The present research serves to characterize the constitutive response and fracture behavior of high strength aluminum alloys at strain rates ranging from low (0.001 s^{-1}) to high (1,000 s^{-1}) conditions. Three aluminum sheet alloys are considered, AA6013-T6, AA7075-T6, and a developmental 7000-series alloy, herein referred to as AA7xxx-T76. The targeted application for this research is the development of material models suitable for application in vehicle crash simulations.

This thesis is written using a manuscript format, comprising this synopsis which captures the major results and conclusions and recommendations from this research, along with four peer reviewed journal publications (three published and one under review) that serve to further detail the research methodology and results. The balance of this synopsis is structured in several sections. Chapter 2 serves to present a review of the literature pertinent to this research. Relevant experimental methodology is presented in Chapter 3, followed by an overview of the results in Chapter 4. A summary and conclusions stemming from this research are presented in Chapters 5 and 6, respectively, while Chapter 7 comprises the recommended future work. Further detail pertaining to the experimental methodology, results, and modelling approach is provided in Appendices A-D. Each appendix is a peer reviewed article, either published or submitted for publication:

Appendix A   T. Rahmaan, A. Abedini, C. Butcher, N. Pathak, M.J. Worswick, Investigation into the shear stress, localization and fracture behaviour of DP600 and AA5182-O sheet metal

alloys under elevated strain rates, International Journal of Impact Engineering, 108: 303-321, 2017.

Appendix B   T. Rahmaan, J. Noder, A. Abedini, P. Zhou, C. Butcher, M.J. Worswick, Anisotropic plasticity characterization of 6000 and 7000 series aluminum sheet metal alloys at various strain rates, International Journal of Impact Engineering, 135: 103390, 2020.

Appendix C   T. Rahmaan, C. Butcher, S. Kim, M.J. Worswick, Characterization and prediction of fracture in 6000- and 7000-series aluminum alloy sheet under various stress states, Thin-Walled Structures, 173: 108958, 2022.

Appendix D   T. Rahmaan, C. Butcher, K. Daun, M.J. Worswick, High strain rate fracture characterization of AA7075-T6 sheet alloy under various stress states, Submitted to the International Journal of Impact Engineering, 2022.

CHAPTER 2: LITERATURE REVIEW

2.1 HIGH STRENGTH ALUMINUM ALLOYS

Since pure aluminum is soft in nature, commercial aluminum alloys are produced by adding selected metallic elements. The strength of aluminum alloys depends principally upon composition and thermo-mechanical processing history. For example, the strength of the 7000-series aluminum alloys generally depends on the Zn/Mg ratio (Nishi *et al.*, 2014). Mukhopadhyay (2009) showed that a sufficient amount of solid solubility is required for the principal alloying element, encouraging nucleation of precipitates in the constituent binary system or inducing the nucleation of new binary/ternary precipitates. Aluminum and other alloying elements form compounds with the minor alloying elements, such as Cr, Mn, and Zn, which inhibit grain growth and recrystallization. Four numerical digits are typically used as a notation to designate different aluminum alloys: the first digit indicates the alloy series along with the major alloying elements, the second digit signifies impurity limits and modifications, and the last two digits are used to differentiate the alloy within the same series. Various aluminum wrought alloy series together with their major alloying elements and common characteristics are shown in Table 1 (Kaufman, 2000).

Table 1: Different aluminum alloys with their main alloying element(s) and basic behavioral and performance characteristics (Kaufman, 2000).

Alloy	Main alloying element (s)	General behavioral and performance characteristics
1xxx	Mostly pure aluminum	High ductility and formability, low strength, high corrosion resistance and electrical conductivity
2xxx	Copper [Cu]	Relatively low ductility and high strength, heat treatable, less resistant to corrosion
3xxx	Manganese [Mn]	Relatively high formability and ductility, medium strength, high resistance to corrosion
4xxx	Silicon [Si]	Low to medium strength, less resistant to corrosion, some alloys are heat treatable
5xxx	Magnesium [Mg]	High strength, exceptionally tough, excellent corrosion resistance
6xxx	Magnesium [Mg] and silicon [Si]	Moderate ductility, very high strength, excellent corrosion resistance, heat treatable
7xxx	Zinc [Zn]	Highest strengths of all aluminum alloys, less tough and susceptible to cracking, less resistant to corrosion, heat treatable

7000–series aluminum alloys are alloyed with low temperature, low solid soluble alloying elements, such as zinc (Zn), magnesium (Mg) and copper (Cu). The solubility limit of these elements in the

aluminum matrix is limited at lower temperatures; thus, such alloys become suitable for heat treatment (Gwozdz and Kwapisz, 2008). The unique properties of 7000-series aluminum alloys are typically achieved by using a higher Zn content along with a lower content of copper and other alloying elements (Chakrabarty *et al.*, 2004). The addition of Cu as one of the alloying elements in Al−Zn−Mg alloys (namely Al−Zn−Mg−Cu) further improves the mechanical strength by precipitation hardening (Wu *et al.*, 2014). Mg content in the composition plays an important role in achieving mechanical strength and corrosion resistance of Al-Zn-Mg-Cu series alloys by forming intermetallic compounds such as S (Al_2CuMg), T ($Al_2Mg_3Zn_3$), and η ($MgZn_2$) phases (Wolverton, 2001). Some 7xxx–series aluminum alloys, such as AA7085, typically show better mechanical properties with higher Mg content in the composition than Cu, while superior mechanical properties can be achieved with a Cu/Mg ratio of 0.67 (Wu *et al.*, 2014).

The major alloying elements for 6000–series aluminum alloys are Si and Mg, in addition to Cu, Mn, and Fe. A SEM micrograph image of un-deformed AA6013 is shown in Figure 2. Prillhofer *et al.* (2014) showed that the rolling texture is influenced by high Cu-content and the low Si/Mg ratio in AA6013. It was also found in studies by Prillhofer *et al.* (2014) and Laughlin *et al.* (1998) that a low Si/Mg ratio generates low elongation values, while relatively high Mn–content in AA6013 increases the initial strength of the material.
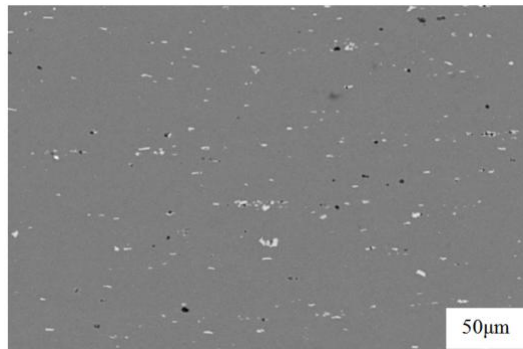
Figure 2: SEM micrograph image of the un-deformed microstructure of AA6013 in T4 condition, 1,000x, black = Al-Mg-Si-Cu particles, white = Al-Fe-Si-Mn-Cu particles [16].

For the heat treatable aluminum alloys, strength can be increased through solution heat treatment followed by aging (natural or artificial) due to the formation of coherent and partially-coherent precipitates which are finely distributed within the material matrix (Ardell, 1985; Nembach, 1997). These precipitates act as obstacles to dislocation motion and increased energy is required to cause deformation; thus, the material gets stronger (Pinlung, 2015). A T-temper designation is used for the heat treated aluminum alloys, and a digit or digits followed by the T designate the specific thermal treatment. The T6 temper indicates that the alloy has been solution heat treated and artificially aged to peak strength, while

T7-type temper indicates the alloy has been solution heat treated and aged in a furnace to an over-aged or stabilized condition beyond peak strength to increase the corrosion resistance. The digit following the T7 indicates the extent of the treatment and the resultant level of corrosion resistance. For example, the T76 indicates a sufficient aging condition to improve resistance to exfoliation corrosion over that of the T6-type temper (Kaufman, 2000).

2.2   HIGH STRAIN RATE MATERIAL BEHAVIOR

The strain rate sensitivity of sheet metal alloys has been widely studied so as to characterize their constitutive response under different strain rate conditions (Dong *et al.*, 2006; He *et al.*, 2005; Li and Meng, 2003; Sligtenhorst *et al.*, 2006). The flow stress of many metals, including aluminum alloys, is often taken to be a function of the logarithm of the strain rate for a certain range of strain rates (Campbell and Ferguson, 1970; Meyers, 1994). It is commonly acknowledged that strain rate-dependent response can be outlined into three strain rate regimes which are demarcated by different mechanisms prevailing the plastic flow. The three regimes of strain rate dependency are shown in Figure 3 for an En3B steel (Campbell and Ferguson, 1970). The behavior in region I is controlled by long-range internal stress fields associated with precipitate particles, grain boundaries and dislocations (Boyce and Dilmore, 2009; Campbell and Ferguson, 1970). Thermally activated dislocation motion generally governs deformation within region II, while the deformation in region III is controlled by drag mechanisms (Meyers, 1994). The transition to a dislocation drag mechanism from a thermal activation mechanism is often construed to be the reason behind the increased strain rate sensitivity for numerous metals at higher rates of strain (Smerd, 2005), on the order of $1\text{x}10^{4}$ s^{-1} (Weertman *et al.*, 1973). For strain rates below $1\text{x}10^{4}$ s^{-1}, the focus of the current research, Follansbee and Weertman (1982) have reported that dislocation draft effects are not rate-controlling. Therefore, the primary governing mechanism for the strain rate sensitivity over the range of strain rates considered in this work (0.001-1,000 s^{-1}) can be attributed to thermally activated dislocation motion.
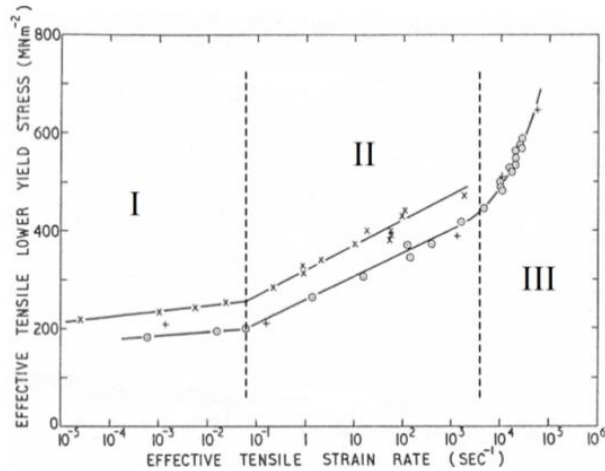
Figure 3: Effective yield stress as a function of strain rate for En3B Steel (Campbell and Ferguson, 1970). The vertical dashed lines and labels are added by the present author.

Tests on different aluminum alloys at various levels of strain rate have been performed by a number of investigators (Chen *et al.*, 2009; Oosterkamp *et al.*, 1999; Rahmaan *et al.*, 2016; Salisbury *et al.*, 2006; Sasso *et al.*, 2015; Smerd *et al.*, 2005). Sasso *et al.* (2015) conducted compression and tensile tests on AA7075 alloy in T6 temper at strain rates ranging from the quasi-static condition up to 2,000 s^{-1}, and reported a mild positive strain rate sensitivity for the flow stress. Similarly, mild positive strain rate sensitivity in tension was reported in (Chen *et al.*, 2009; Jurczak, 2012; Reyes *et al.*, 2006) based on investigations of several different types of 7000–series aluminum alloys.

Smerd *et al.* (2005) and Hadianfard *et al.* (2008) tested the ductility of AA5754 and AA5182 at various strain rates in tension, and demonstrated a small increase in the elongation at fracture. Clausen *et al.* (2004) reported that the fracture strain in tension is rate independent in the dynamic strain aging region for AA5083-H116, while rate sensitivity increases considerably for elevated rates. Sasso *et al.* (2015) conducted compression and tensile tests on AA7075-T6 at strain rates ranging from the quasi-static condition up to 2 x10^3 s^{-1}, and reported that the fracture strain decreases with an increase in strain rate. Similar to previous authors, tension tests performed by Brar *et al.* (2009) on AA7075-T6 at strain rates of 10^0 and 10^3 s^{-1} showed moderate strain rate sensitivity in the flow curves at room temperature conditions. However, Brar *et al.* (2009) disagreed with the conclusion presented by Sasso *et al.* (2015), and reported that the equivalent fracture strain at failure increases with an increase of strain rate in tension tests on smooth tensile specimens at high strain rates (1,700 s^{-1}) and ambient temperature. Quasi-static and dynamic compression tests were carried out on cylindrical specimens of AA7075-T7351 by El-Magd and Abouridouane (2006) at strain rates ranging from 0.001 s^{-1} to 5000 s^{-1} and temperatures between 20 and 500°C. The strain rate sensitivity of the flow curve under compression loading is reported to be mild, while an increase in strain to fracture with increasing rate of strain is presented. In tensile loading, an

opposite behavior was observed in which the strain rate sensitivity of the flow curve is found to be large, while the fracture strain decreased with an increase in strain rate.

6000–series aluminum alloys usually display mild positive strain rate sensitivity in their flow stress and fracture strain (Børvik *et al.*, 2005). Based on compression tests on the AA6082 alloy in tempers T6 and T79 at strain rates ranging from 0.1 to approximately 2,000 s^{-1}, Oosterkamp *et al.* (1999) reported mild positive strain rate sensitivity in the flow stress. Similar rate sensitivity was reported by Chen *et al.* (2009) for extruded 6000–series aluminum alloys in tension loading for strain rates ranging from 10^{-3} to 10^{3} s^{-1}. More recently, Xiao *et al.* (2016) performed hot plane strain compression tests on the AA6013 aluminum alloy at temperatures ranging from 613 to 773 K and strain rates ranging from 10^{-3} to 10 s^{-1}, and reported a considerable increase in flow stress with increasing strain rate.

At strain rates higher than 1 s^{-1}, adiabatic heating begins to cause thermal softening (Cheng *et al.*, 2014; Lee *et al.*, 2007). The temperature is assumed to be constant (isothermal assumption) in the case of quasi-static strain rates since the heat generated within the specimen is assumed to dissipate either through convection to air or through conduction to the test frame grips (Zhang *et al.*, 2013). At higher strain rates, the increase in temperature within the specimen gauge area produces a gradient in the strength of the material which tends to concentrate the strain and leads to localized necking. The effect becomes more pronounced at elevated rates of strain because the flow stress is increased and the dissipation of heat is delayed (Pinlung, 2015; Thompson, 2006). Pérez-Castellanos *et al.* (2012) conducted dynamic compression tests on AA6082 sheet and reported a decrease in strain to localization with increasing strain rate. El-Magd and Abouridouane (2006) showed strong positive work hardening and positive strain rate sensitivity of the flow curve of AA7075 at lower strains (Figure 4); however, strong thermal softening was observed at larger strains for strain rates above 1,000 s^{-1} due to the adiabatic heat generation and temperature rise in the specimen.
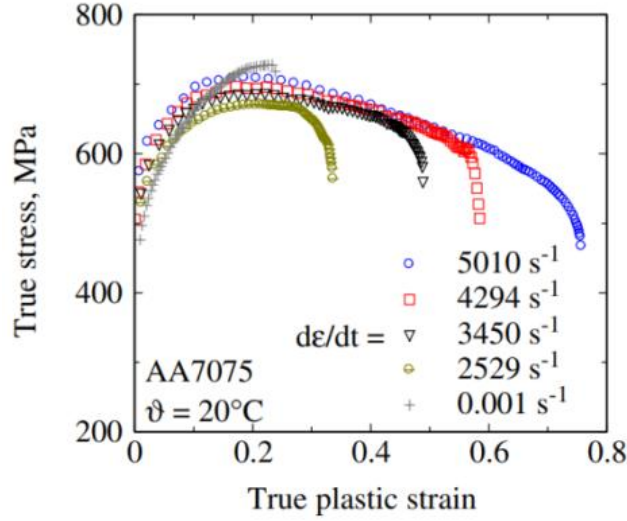
Figure 4: Flow curves of AA7075 at different strain rates (El-Magd and Abouridouane, 2006).

The maximum temperature rise, ΔT due to deformation heating from plastic work can be calculated using Eq. (2.1).

$$\Delta T = \frac{\beta}{\rho \cdot C_p} \int_0^{\varepsilon_p} \sigma \, d\varepsilon_p \qquad \text{Eq. (2.1)}$$

where, C_p is the heat capacity of the material, ρ is the material density, β, the Taylor-Quinney coefficient, is the ratio of plastic work converted into heat, and the remainder is the integral of the flow stress *versus* effective plastic strain (plastic work).

MacDougall (2000) showed the value of β to vary for different materials and found that β increases with plastic strain from approximately 0.5 to 0.9 for AA2011 aluminum alloys. Studies performed on 4340 steels and AA2024 by Mason *et al.* (1994) demonstrated that under tensile states, increases in strain rate can lead to increased values of β for strain rate sensitive materials. More recently, experimental work performed by Rittel *et al.* (2017) on AA5086 and AA2024 cylindrical specimens found a strong dependence of β on strain and strain rate, while the value of β can increase or decrease depending upon the loading mode.

For predicting the plasticity and fracture response of Advanced High Strength Steel (AHSS) sheet under different loading conditions and strain rates, Roth *et al.* (2018; 2014) and Dunand *et al.* (2017) calculated the temperature rise at different strain rates within numerical models by varying the value of β with strain rate through introducing a strain rate dependent factor ω in Eq. (2.1) in a multiplicative form, as shown in Eq. (2.2):

$$\Delta T = \frac{\omega \cdot \beta}{\rho \cdot C_p} \int_0^{\varepsilon_p} \sigma \, d\varepsilon_p \qquad\qquad \text{Eq. (2.2)}$$

in which the limiting cases $\omega = 0$ and $\omega = 1$ correspond to isothermal conditions and adiabatic conditions, respectively. The temperature increase for intermediate strain rates was approximated in an empirical manner through the parametric form

$$\omega = \begin{cases} 0 & \text{for } \dot\varepsilon_p < \dot\varepsilon \\ \dfrac{\left(\dot\varepsilon_p - \dot\varepsilon_{it}\right)^2 + \left(3\dot\varepsilon_a - 2\dot\varepsilon_p - \dot\varepsilon_{it}\right)}{(\dot\varepsilon_a - \dot\varepsilon_{it})^3} & \text{for } \dot\varepsilon_{it} \leq \dot\varepsilon \\ 1 & \text{for } \dot\varepsilon_a < \dot\varepsilon \end{cases} \qquad\qquad \text{Eq. (2.3)}$$

with the parameters $\dot\varepsilon_{it} > 0$ and $\dot\varepsilon_a > \dot\varepsilon_{it}$ defining the limits of the respective domains of isothermal and adiabatic conditions. Although this method of considering temperature rise at different strain rates provided good agreement with the experimental results, the determination of temperature evolution was purely based on mathematical analyses. Experimental data pertaining to temperature rise in sheet metal alloys due to deformation heating at high strain rates is limited in the literature.

While the foregoing discussion confirms that a number of studies are available on the strain rate sensitivity characterization of aluminum alloys, the existing literature is not conclusive and warrants further investigation. Thus, the high strain rate characterization of high strength aluminum sheet alloys is a key focus of the current research.

2.3   CONSTITUTIVE MODELS

The description of the constitutive response of a sheet metal alloy is a critical aspect of finite element analysis (FEA). The flow stress of a specific material is often predicted utilizing constitutive models describing the material hardening response as a function of strain, strain rate, temperature and other state variables. Therefore, the accuracy of finite-element analysis hinges upon the constitutive model.

Many constitutive models have been proposed in the literature with one of the most commonly used being that of Johnson and Cook or JC model (Johnson and Cook, 1983). The phenomenological JC model accounts for the effects of strain hardening, strain rate, and thermal softening in a multiplicative form. An evaluation of predictions using this model was conducted based on cylinder impact tests for several materials including AA2024-T351 and AA7039 aluminum alloys. The model is described as:

$$\sigma = (A + B\varepsilon_p^n)(1 + C \ln \dot{\varepsilon}^*)(1 - T^{*m}) \qquad \text{Eq. (2.4)}$$

in which, σ is the equivalent stress, ε_p is the equivalent plastic strain, $\dot{\varepsilon}$ is the plastic strain rate, $\dot{\varepsilon}^* = \dot{\varepsilon}/\dot{\varepsilon}_o$ is a dimensionless plastic strain rate with respect to a reference strain rate $\dot{\varepsilon}_o$, and T^* is a form of homologous temperature,

$$T^* = \frac{T - T_{ROOM}}{T_{MELT} - T_{ROOM}} \qquad \text{Eq. (2.5)}$$

where, T_{ROOM}, T, and T_{MELT} are the room temperature, temperature condition of the specimen, and melting temperature of the material, respectively. The material constants, A, B, n, C, and m, are fit to the experimental data where the yield stress is described by A, the strain hardening is represented by B and n, C represents the effect of strain rate, and the effect of temperature rise is denoted by m. In order to account for the temperature effect in a test conducted below room temperature, Gray III *et al.* (1994) utilized the homologous temperature, T^*, given as:

$$T^* = \frac{T}{T_{MELT}} \qquad \text{Eq. (2.6)}$$

in which the temperature is specified in Kelvin.

The JC model was fit to experimental data for a number of materials and test conditions by Gray III *et al.* (1994). Figure 5 shows the constitutive fits for AA7039. This work has demonstrated the limitation of the JC model with respect to describing the material response for a range of strain rates and temperatures, which is mainly due to the simplified power law assumption for the material hardening term in Eq. (2.4). In addition, the JC model is unable to capture the flow stress response of complex materials, such as OFHC copper and AA5083, for which the effect of strain rate and temperature on the material hardening is dependent on the strain (Gray III *et al.*, 1994).
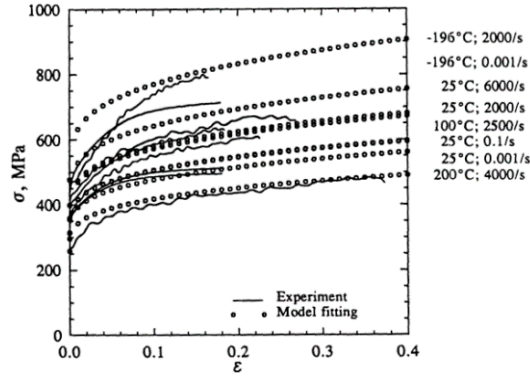
Figure 5: Johnson-Cook model fits to the experimental data of AA7039. The model parameters used in the model fitting are $A = 475$ MPa, , $B = 550$ MPa, $n = 0.275$, $C = 0.0125$, $m = 1.0$, and $T_{MELT} = 933$ K (Gray III *et al.*, 1994).

A dislocation mechanics-based strain rate and temperature dependent constitutive model was proposed by Zerilli and Armstrong (ZA) (1987). The ZA model incorporated the strain hardening, strain rate, and thermal softening into the constitutive function based on thermal activation analysis. The constitutive response for different material structure types which define the rate-controlling mechanisms, such as face-centered-cubic (FCC) and body-centered-cubic (BCC) structures, are captured using different forms of the ZA equations. In general, Liang and Khan (1999) demonstrated that the ZA models have limitations in predicting the hardening response of materials with strong strain rate sensitivity or other complex material behavior. In addition, the power-law type function in the ZA model is not well-suited to aluminum alloys, often exhibiting saturation in work hardening.

Apart from the JC and ZA models, other phenomenological models such as Swift (1952), Ludwik (1909), Hollomon (1945), Gosh (1977), Voce (1948) and Hockett–Sherby (1975) are widely used. Combinations of models such as the Swift–Hockett–Sherby (Kaps *et al.*, 1999) or Swift-Voce (Kessler and Gerlach, 2006) models provide further improved results. Although most of these models were developed utilizing phenomenological approaches, some parameters of the models are directly associated with physical properties of the materials. As an example, the material parameters of the Hockett–Sherby (1975) model are directly related to the yield stress and the strain hardening characteristics of the materials.

Most of the aforementioned phenomenological models alone are neither strain rate sensitive nor temperature sensitive. Therefore, strain rate and temperature dependent terms are typically coupled to capture the changes in hardening response with respect to strain rate and temperature. Following the methods proposed by Camacho and Ortiz (1997) and by Børvik *et al.* (2001), Bardelcik *et al.* (2012a; 2012b, 2010) coupled an exponential-type strain rate function with the Voce model in order to capture the

12

material strain rate sensitivity. Other strain rate sensitivity functions, such as combined logarithmic and exponential type functions can also be integrated with these hardening models.

The majority of available hardening models differ mostly according to their range of validity, which varies with their complexity in terms of capturing strain, strain rate, and temperature effects, for example. Due to a lack of test data over a wide range of strain rate, only a limited number of constitutive fitting efforts have been performed for 7000- and 6000–series aluminum sheet alloys. Thus, one goal of the proposed research is to investigate appropriate constitutive models for low (0.001 s^{-1}) to high (10^3 s^{-1}) rates of strain and propose a strain rate-sensitive term(s) to accurately predict the experimental data.

Traditionally, the hardening response and fracture behaviour at elevated strain rates are characterized using uniaxial tensile tests (Abedini *et al.*, 2015; Bardelcik *et al.*, 2010). Such material hardening data is only valid for strains up to the onset of diffuse necking, as characterized by the Considère criterion (1885). According to the Considère criterion, diffuse necking in uniaxial tension begins when the rate of strain hardening is equivalent to the true stress. The measured true stress response beyond this point is no longer homogeneous uniaxial tension. The ductility of advanced high strength metal alloys is often reduced due to higher strength and lower hardening rate. As a result, the valid range of tensile data for constitutive characterization of a material decreases to uniform elongation strains on the order of 5-10% (Abedini *et al.*, 2015; Bardelcik *et al.*, 2010; Rahmaan *et al.*, 2016; Smerd *et al.*, 2005; Thompson, 2006). The strain levels at fracture are much larger than the level of strains at onset of diffuse necking. For example, the local fracture strain of ultra high strength boron steel under uniaxial tension at a strain rate of 0.001 s^{-1} is approximately 70%, while the material experiences diffuse necking at strains as low as 5% (ten Kortenaar, 2016). Papasidero *et al.* (2015) showed that the fracture of aluminum 2024-T351 in tubular specimens occurs at a higher strain to fracture for torsion (simple shear) than for uniaxial tension (Papasidero *et al.*, 2015). Scales *et al.* (2016) recently reported considerably larger strains at failure than previously reported values for AA6061-T6 tubular specimens based on statistical grain-level measurements. The hardening response at large strains associated with fracture is typically obtained either through inverse finite-element (FE) techniques or by hardening law extrapolation (Rahmaan *et al.*, 2016). However, a linear or simple power-law extrapolation is often not sufficient (Ling, 1996; Rahmaan *et al.*, 2016; Roth and Mohr, 2014). In an inverse modelling technique, a numerical model is developed with a set of initial input parameters, and the model results are compared with the experimental data until a set of input parameters provide model results matching with the desired experimental results. Therefore, inverse finite-element inverse modelling techniques become time-consuming and can produce non-unique solutions, especially for elevated strain rate conditions when strain rate and adiabatic softening must be taken into account.

As an alternative to inverse modelling of tensile tests, simple shear tests can be used to obtain large-strain constitutive data since shear tests since a tensile instability cannot occur. In addition, proportional deformation of simple shear specimens can be achieved until fracture and utilized in the calibration of stress-state dependent fracture *loci*.

2.4   PLASTIC ANISOTROPY

Anisotropy, or directional variation of mechanical properties, exists in automotive sheet metal alloys as a consequence of the rolling process (Banabic, 2000). The anisotropic response of a sheet metal alloy plays critical role during metal forming processes because of its influence on the formability along different sheet orientations. Anisotropy is also considered in crashworthiness simulations of aluminum materials such as 6xxx-series extrusions. A manifestation of the rolled crystallographic texture in sheet alloys appears as a difference in mechanical properties, such as in yield stress, along different sheet orientations with respective to the sheet rolling direction. Furthermore, the ratio of width-to-thickness strain during uniaxial tensile tests, referred to as the *r*–value or Lankford coefficient, is altered by the rolling process which affects the thinning behavior during forming operations. The average r-value is defined as

$$r = \frac{\varepsilon_{width}^{p}}{\varepsilon_{thickness}^{p}} \qquad\qquad \text{Eq. (2.7)}$$

in which ε_{width}^{p} is the true plastic width strain and $\varepsilon_{thickness}^{p}$ is the true plastic thickness strain. For an isotropic sheet alloy, the *r*–value is always unity.

The anisotropic response of AA7075 aluminum sheet was characterized by Tajally and Emadoddin (2011) based on uniaxial tensile tests at room temperature after annealing cold worked samples at different temperatures (270–450˚C). The maximum strengths were observed in the 90° direction and the elongation along the 45° direction was greater than those in the other directions. The r–value along the rolling direction is reported to be between 0.49–0.77, while for the 90˚ and 45˚ directions it was reported to be 0.52–0.79 and 0.79–1.02, respectively. The r–value was found to be the highest along the diagonal (45˚) direction for any given annealing condition.

In addition to obtaining the material stress-strain response over a range of strain rates, it is also necessary to identify the dependency of anisotropy (*r*–value) of automotive sheet metals on strain rate to develop an accurate plasticity model. Currently, only a limited amount of experimental data is available characterizing the anisotropic response of 6000- and 7000-series aluminum alloys across a broad range of strain rates and different sheet orientations. Thus, the current research includes a series of tests to

14

characterize the anisotropic response of AA6013-T6, AA7075-T6, and AA7xxx-T76 sheet for a range of strain rate.

2.5 YIELD CRITERIA

Defining an accurate description of yielding behavior is important to model the anisotropic response of sheet metal alloys in FE simulations. The continuum yield behavior can be captured through two different approaches: physical-based models and phenomenological models. The crystal structure and crystallographic texture are the basis of physical-based models, in which the material is assumed to be a polycrystal. In physical-based approaches, it is assumed that a relatively large number of grains composes each point of the polycrystal at the continuum level in which dislocation glide occurs on certain slip systems (Barlat et al., 1997; Beaudoin et al., 1994; Becker, 1993). Physically-based models within FE codes have been used successfully to predict the anisotropic response of different metal alloys (Hua *et al.*, 2008; Inal *et al.*, 2002; Plunkett *et al.*, 2006; Van Liempta and Sietsmaa, 2016). However, the crystallographic textures and microstructural material parameters are typically the key input for these models, and measuring such material data is complex. In addition, the computing time needed to carry out physical-based FE simulations can be expensive, which limits the application of these approaches for industrial problems.

In the phenomenological approach, the plastic yielding behavior is assumed to be defined by a yield surface in stress space that evolves with plastic deformation. The computational time required for phenomenological yield functions is considerably less than that for the physical-based crystal plasticity approach (Barlat *et al.*, 1997). The implementation of phenomenological models into the FE code is less complex as well. Hence, the phenomenological approach to describe yielding has gained popularity for industrial applications and was adopted in the current research in an effort to ensure applicability to industrial applications.

The isotropic maximum shear stress yield function proposed by Tresca (1864) is known to be the oldest phenomenological yield criterion; however, the von Mises (1913) quadratic yield function is the most widely used isotropic yield function. The graphical representations of the Tresca and von Mises yield criteria are shown in Figure 6. , Hershey (1954) and Hosford (1972), as shown in Eq. (2.8), introduced a non-quadratic isotropic yield function utilizing an exponent, a, based on the results of polycrystal calculations to obtain better accuracy compared to the quadratic von Mises yield criterion. Further improvements to the original Hosford model were developed to increase the accuracy for shear and plane stress conditions, as well as to account for a six component stress state in isotropic materials (Barlat *et al.*, 1991; Barlat and Lian, 1989; Barlat and Richmond, 1987; Hosford, 1992).
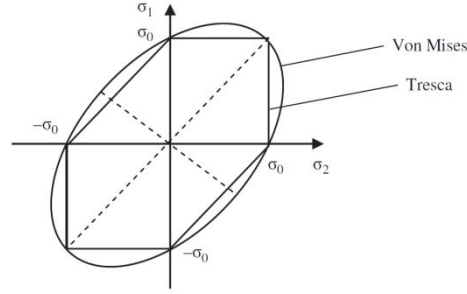
Figure 6: Graphical representation of the Von Mises and Tresca yield criteria (Banabic, 2010).

$$\bar{\sigma}_{Hosford} = \left\{\frac{1}{2}((\sigma_1 - \sigma_2)^a + (\sigma_2 - \sigma_3)^a + (\sigma_1 - \sigma_3)^a)\right\}^{\frac{1}{a}} \qquad \text{Eq. (2.8)}$$

A phenomenological extension of von Mises to model anisotropic materials was proposed by Hill (1948), known as the Hill48 model, has been widely used in FE simulations due to its simple form but is seldom able to sufficiently describe anisotropy of aluminum (Mellor, 1981; Mellor and Parmar, 1978).

A series of phenomenological anisotropic yield functions were proposed by Barlat *et al.* (Aretz and Barlat, 2013; Barlat et al., 2005, 2003, 1997, 1991; Barlat and Lian, 1989). Barlat and Lian (1989) proposed a generalized form of their original isotropic yield function based on the linear transformation of the stress tensor in order to predict the yield response of the materials exhibiting planar anisotropy. This so–called Barlat YLD89 model (Barlat and Lian, 1989) became the basis of future proposed models. The Barlat YLD89 provided a reasonable prediction of the yield locus for aluminum alloys but the model was not able to accurately predict the biaxial yield stress for aluminum alloys with pronounced anisotropy (Banabic, 2010). To improve accuracy relative to the Barlat YLD89 yield locus, further improvement was proposed in the next three consecutive yield functions: Barlat YLD91 (Barlat *et al.*, 1991), Barlat YLD94 and YLD96 (Barlat *et al.*, 1997). The plane stress Barlat YLD2000–2D (Barlat *et al.* 2003) model incorporates eight coefficients that are identified from uniaxial tension tests, shear tests, and biaxial tension tests (Banabic, 2010).

A methodology similar to YLD2000–2D was followed by Aretz and Barlat (2004) and Barlat *et al.* (2005) to develop the Barlat YLD2004-18p yield criterion to account for 3–D stress states by considering all six components of the stress tensor. Two stress transformations are used and each transformation requires 9 coefficients, totaling 18 coefficients. The Barlat YLD2004 yield function has been successfully used in forming simulations of aluminum alloys despite being computationally expensive and involving a complex calibration process (Fourmeau *et al.*, 2013, 2011; Grytten *et al.*, 2008; Ha *et al.*, 2019; Yoon *et al.*, 2006).

As shown in the above literature review, a number of yield functions are available to predict the anisotropic plastic behavior of sheet metals. The challenge is to select the appropriate one (with the least parameters) while maintaining accuracy and performing the required tests and calibrations which is discussed further in Chapter 4 for the AA7075, AA7xxx-T76, and AA6013 alloys.

2.6   DUCTILE FRACTURE

The fracture of metals of materials can be divided into two categories: ductile and brittle. Only a small amount of plastic deformation caused by a sudden failure occurs during brittle fracture. Ductile failure, exhibits rough surfaces with gross plastic deformation (Hashemi, 2006). Accurate prediction of ductile fracture in sheet metal alloys is critical in order to understand the formability and crashworthiness of automotive and aerospace structural and body components. Mechanical models to predict ductile fracture can also be divided into two categories: micromechanical damage models and phenomenological models.

2.6.1   MICROMECHANICAL MODELS OF FRACTURE

Micromechanical damage models are physically based, and attempt to model the different stages of microscopic ductile fracture (as shown in Figure 7). At a microstructural level, ductile fracture is induced by the nucleation, growth, and coalescence of voids, followed by material softening and fracture. As shown in Figure 7a, material contains voids, as well as inclusions and second-phase particles which are the sites for nucleation of additional voids. Additional voids are then nucleated by particle cracking or debonding with plastic deformation (Figure 7b). The voids grow with further deformation (Figure 7c) leading to a rapid link-up to form microscopic cracks that propagate throughout the material causing failure (Figure 7d). The role and evolution of voids during plastic deformation has been studied by McClintock (1968) and Rice and Tracey (1969). These studies assumed failure initiates when a critical value of the void volume fraction is reached for each specific material, while neglecting the hardening effects, the coalescence process, and interaction between micro voids.
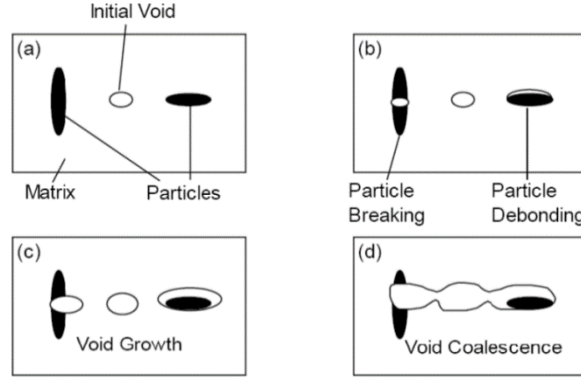
Figure 7: Different stages of microscopic ductile fracture, (a) initial state, (b) void nucleation, (c) void growth, and (d) void coalescence (Chen, 2004).

The widely used micromechanical Gurson model (1977) is based on a porous-plastic yield function. Tvergaard and Needleman (1984) proposed the Gurson-Tvergaard-Needleman (GTN) model, to account for the void nucleation and coalescence. The GTN model struggles with fracture prediction in shear where there is no void growth which was remedied by Nahshon and Xue (2009) and Nielsen and Tvergaard (2010). The shear-modified GTN models can better predict fracture in shear-dominated stress states but the empirical modifications compromise the micromechanical foundation of the Gurson model (Dunand and Mohr, 2011; Ghahremaninezhad and Ravi-Chandar, 2013). The large number of parameters involved in the GTN models causes the calibration process to be difficult and less suitable for industrial applications (Bao, 2003). Alternative phenomenological models that are more computationally efficient and contain fewer parameters, such as the Modified Mohr Coulomb (MMC) model, can be used to obtain as good or better accuracy than recent forms of the Gurson model.

2.6.2   PHENOMENOLOGICAL MODELS OF DUCTILE FRACTURE

Ductile fracture is strongly influenced by the stress state. Before reviewing phenomenological models, it's important to review the concepts in the characterization of loading conditions in terms of the stress invariants. The triaxiality and Lode (1926) angle parameter can be used to quantify all forms of isotropic loading conditions (stress state). The stress triaxiality (η) is defined as the ratio of mean stress, or hydrostatic pressure, to the von Mises equivalent stress (Bhadauria *et al.*, 2009), as shown in Eq. (2.9).

$$\eta = \frac{\sigma_{hyd}}{\bar{\sigma}} \qquad \text{Eq. (2.9)}$$

in which $\bar{\sigma}$ is the von Mises equivalent stress and σ_{hyd} is the hydrostatic pressure. The Lode angle parameter (θ) is a function of the second and third invariant of the stress deviator, as shown in Eq. (2.10).

$$\theta = \frac{1}{3}\cos^{-1}\left(\frac{3\sqrt{3}}{2}\frac{J_2}{J_3^{3/2}}\right), 0 \leq \theta \leq \frac{\pi}{3} \qquad \text{Eq. (2.10)}$$

where J_2 and J_3 are the second and third invariants of the stress deviator, respectively. It is to be noted that the use of the dimensionless Lode angle parameter ($\bar{\theta}$), defined in Eq. (2.11), is more common in the literature.

$$\bar{\theta} = 1 - \frac{6\theta}{\pi}, -1 \leq \bar{\theta} \leq 1 \qquad \text{Eq. (2.11)}$$

A relationship between triaxiality and Lode angle parameter is described by Bai and Wierzbicki (2008) for plane-stress conditions, as shown in Eq. (2.12).

$$\cos\left[\frac{\pi}{2}(1 - \bar{\theta})\right] = -\frac{27}{2}\eta\left(\eta^2 - \frac{1}{3}\right) \qquad \text{Eq. (2.12)}$$

in which, $\bar{\theta}$ is the dimensionless Lode angle parameter and η is the stress triaxiality. In the principal stress space, the Lode parameter can be defined as:

$$\mu_L = \frac{2\sigma_2 - \sigma_1 - \sigma_3}{\sigma_1 - \sigma_3} = \frac{3(\sigma_2 - \sigma_{hyd})}{\sigma_1 - \sigma_3} \qquad \text{Eq. (2.13)}$$

The values of stress triaxiality and Lode parameter corresponding to different characteristic loading conditions are shown in Table 2.

Table 2: Values of stress triaxiality and Lode parameter for different plane stress loading conditions (Chen and Butcher, 2013).

Loading condition	Triaxiality (η)	Lode parameter (μ_L)
Pure shear and Simple Shear	0	0
Uniaxial tension	0.333	-1
Plane strain tension	0.577	0
Equal–biaxial tension	0.667	1

The fracture model proposed by Cockcroft and Latham (1968) proposed assumed that fracture occurs when the plastic work per unit volume reaches a critical threshold , D_{CL}, as

$$\int_0^{\varepsilon_f} \bar{\sigma} \left(\frac{\sigma^*}{\bar{\sigma}} \right) d\bar{\varepsilon} = D_{CL} \qquad \text{Eq. (2.14)}$$

where $\bar{\sigma}$ is the equivalent stress, $\bar{\varepsilon}$ is the equivalent strain, ε_f is the equivalent fracture strain, and the effect of the highest tensile stress, σ^*, is represented by a non-dimensional stress-concentration factor, $\sigma^*/\bar{\sigma}$. Oh et $al.$ (1979) later introduced the normalized maximum principal stress $\sigma_1/\bar{\sigma}$ as the weighting function to the Cockcroft and Latham (1968) model, and proposed a modified version:

$$\int_0^{\varepsilon_f} \frac{\langle \sigma_1 \rangle}{\bar{\sigma}} d\bar{\varepsilon} = D_{CL} \qquad \text{Eq. (2.15)}$$

the Macaulay bracket, $\langle \cdot \rangle$, indicates that only the positive part of principal stress, σ_1, is taken. The Cockcroft-Latham model requires calibration of only one fracture parameter, D_{CL}, making it an attractive failure criterion for industrial applications.

The Johnson and Cook fracture model (Johnson and Cook, 1985), as shown in Eq. (2.16), one of the most commonly adopted phenomenological fracture models, accounts for the effect of strain rate, stress triaxiality, and temperature on fracture strain. Fracture is predicted to occur when the damage parameter D_{JC} in Eq. (2.17) reaches unity. Eq. (2.16) describes the equivalent strain to failure, ε_f, under monotonic loading conditions. The first term in Eq. (2.16) articulates that the strain to fracture decreases as the triaxiality increases, while the second term accounts for the effect of strain rate and the third term captures the effect of temperature on failure strain.

$$\varepsilon_f(\eta) = (D_1 + D_2 e^{D_3 \eta})(1 + D_4 \ln \dot{\varepsilon}^*)(1 + D_5 T^*) \qquad \text{Eq. (2.16)}$$

$$D_{JC} = \int \frac{d\varepsilon_p}{\varepsilon_f} < 1 \qquad \text{Eq. (2.17)}$$

Note that D_1 to D_5 are material constants that are calibrated based on measured data, η is the stress triaxiality, $\dot{\varepsilon}^*$ is a non-dimensional plastic strain rate term, and T^* is a form of homologous temperature, as defined in Eq. (2.5). The exponential dependence of the Johnson-Cook with the triaxiality was later found to be problematic in that it does not capture the increase in the fracture strain in plane stress biaxial stretching. For sheet metals, this trend is inaccurate since the lowest failure strain typically corresponds to

plane strain loading conditions (Bai and Wierzbicki, 2015, 2008; Roth, 2015; Roth and Mohr, 2014). The limitation of the JC model is that it omits a dependence upon the Lode parameter.

The Mohr–Coulomb (MC) yield criterion (Coulomb, 1776; Mohr, 1914) was developed to model the yield behavior of granular and brittle materials with tension-compression asymmetry. Ductile metals typically have minor tension-compression asymmetry in the yield behavior but have significant asymmetry in fracture. The fracture limits in compression and shear tend to far exceed the limits in tension. The MC criterion is formulated when the shear stress and normal stress reaches a critical value, according to

$$(\sigma_I - \sigma_{III}) + c_1(\sigma_I + \sigma_{III}) = \beta \qquad \text{Eq. (2.18)}$$

in which σ_I and σ_{III} are the maximum and the minimum principal stresses. The material constants c_1 and β are referred to as friction and shear resistance coefficients, respectively. In the limiting case of $c_1 = 0$, the Mohr–Coulomb criterion reduces to a maximum shear stress criterion that assumes fracture will occur when the maximum shear stress reaches a critical value. Bai and Wierzbicki (2010) proposed using the MC yield criterion as a ductile fracture criterion. The so-called modified Mohr Coulomb (MMC) criterion was formed using power law hardening and recasting the MC criterion into the equivalent strain, triaxiality and Lode parameter

$$\varepsilon_f(\eta, \theta) = \left\{ \frac{A}{c_2} \left[c_3 + \frac{\sqrt{3}}{2 - \sqrt{3}}(1 - c_3) \left(\sec\left(\frac{\bar{\theta}\pi}{6}\right) - 1 \right) \right] \left[\sqrt{\frac{1 + c_1^2}{3}} \cos\left(\frac{\bar{\theta}\pi}{6}\right) + c_1 \left(\eta + \frac{1}{3}\sin\left(\frac{\bar{\theta}\pi}{6}\right) \right) \right] \right\}^{-\frac{1}{n}} \quad \text{Eq. (2.19)}$$

in which, *A* and n are two power law coefficients, c_1, c_2, and c_3 are three fracture parameters.

Bai and Wierzbicki (2008, 2015) assessed the capability of the Cockcroft-Latham (1968) and Johnson-Cook (1985) fracture models for AA2024-T351 under different loading conditions. Since the fracture criteria for both of these models are not dependent on the Lode angle parameter ($\bar{\theta}$), the models reasonably capture the influence of stress triaxiality (η) on fracture strain (ε_f) but were unable to predict the non-monotonic trend of fracture strains under different loading conditions, as shown in Figure 8(a and b). On the other hand, the MMC type fracture models, such as Bai and Wierzbicki (2008, 2010), consider the effect of both triaxiality and Lode parameter on the fracture strain; thus, the dependency of fracture strain as a function of loading condition is well captured, as shown in Figure 8c for the Bai and Wierzbicki (2010) fracture model. Lou *et al.* (2012, 2014) and Kubík *et al.* (2016) have also proposed phenomenological models to describe the fracture loci in terms of the triaxiality and Lode parameter.
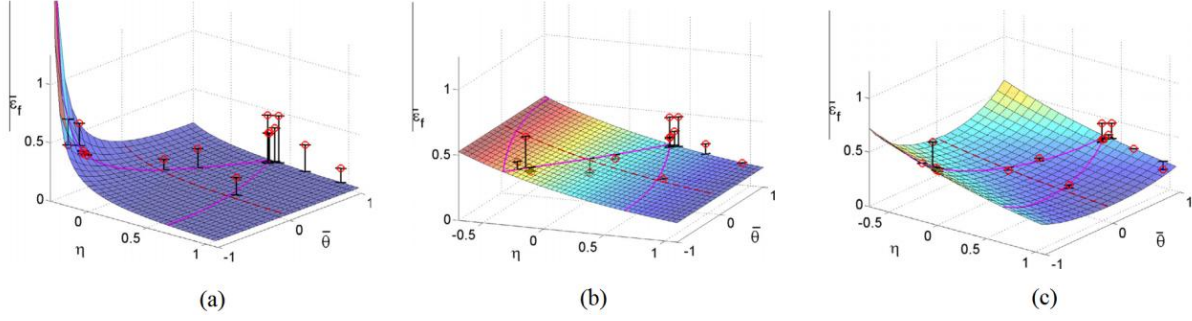
Figure 8: Fracture *loci* of AA2024-T351 alloy calibrated by (a) Cockcroft-Latham (1968) (b) Johnson-Cook model (1985) and (c) Bai and Wierzbicki (2010) fracture models (Bai and Wierzbicki, 2015).

From the localization analysis of a porous unit cell containing an initially spherical void in tensile and shear loading, Mohr and Marcadet (2015) proposed the Hosford–Coulomb (HC). The shear and normal stresses at the onset of void coalescence were fit to reasonable agreement with the MC model but a dependence upon the intermediate principal stress was observed. The HC model was arrived at by replacing the maximum shear stress (or Tresca equivalent stress) in the MC criterion of Eq. (2.18) with that of the Hosford form. The HC model is

$$\bar{\sigma}_{Hosford} + c(\sigma_I + \sigma_{III}) = \beta \quad \text{or} \quad \bar{\sigma}_f = \frac{\beta}{g_{HC}[\boldsymbol{\sigma}/\bar{\sigma}]} \qquad \text{Eq. (2.20)}$$

here, σ_I and σ_{III} are the maximum and the minimum principal stresses, and σ_f is the fracture stress. The invariant form of the Hosford-Coulomb function, $g_{HC}[\boldsymbol{\sigma}/\bar{\sigma}]$, is

$$g_{HC}[\boldsymbol{\sigma}/\bar{\sigma}] = \left\{ \frac{1}{2} \left((f_1 - f_2)^a + (f_2 - f_3)^a + (f_1 - f_3)^a \right) \right\}^{\frac{1}{a}} + c(2\eta + f_1 + f_3) \qquad \text{Eq. (2.21)}$$

The functions f_{1-3} are Lode angle parameter dependent trigonometric functions related to the principal stresses to Haigh–Westergaard coordinate transformation and defined as:

$$f_1(\bar{\theta}) = \frac{2}{3} \cos \left[\frac{\pi}{6}(1 - \bar{\theta}) \right], f_2(\bar{\theta}) = \frac{2}{3} \cos \left[\frac{\pi}{6}(3 + \bar{\theta}) \right], f_3(\bar{\theta}) = -\frac{2}{3} \cos \left[\frac{\pi}{6}(1 + \bar{\theta}) \right] \qquad \text{Eq. (2.22)}$$

in which, the Hosford exponent, a, governs the deviatoric stress measure with the limiting cases of Tresca ($a = 1 \; or \; a = \infty$) and von Mises ($a = 2 \; or \; a = 4$), β is related to the fracture stress in shear, and material constant c controls how the fracture response from shear to compression region behaves. The HC

model is formulated in stress space for direct coupling with the yield function and hardening behavior in contrast to the MMC model. An equivalent strain-based form for power law hardening can be obtained as in Mohr and Marcadet (2015) as expressed

$$\varepsilon_f(\eta, \bar{\theta}) = \beta(1+c)^{\frac{1}{n}} \left(\left\{ \frac{1}{2}((f_1 - f_2)^a + (f_2 - f_3)^a + (f_1 - f_3)^a) \right\}^{\frac{1}{a}} + c(2\eta + f_1 + f_3) \right)^{-\frac{1}{n}} \qquad \text{Eq. (2.23)}$$

Roth and Mohr (2014) extended the HC formulation to incorporate the strain rate effect on fracture through the multiplier parameter, β, as shown in Eq. (2.24). A hybrid experimental-numerical approach was followed to evaluate the strain rate dependent Hosford-Coulomb model (Roth and Mohr, 2014). Although the strain rate dependent Hosford-Coulomb model provided good agreement with the available experimental data for several AHSS sheet alloys, it required an extensive amount of inverse modeling.

$$\beta = \beta_0 \left(1 + \gamma \ln\left(\frac{\dot{\varepsilon}}{\dot{\varepsilon_0}}\right) \right) \quad \text{when } \dot{\varepsilon} > \dot{\varepsilon_0} \qquad \text{Eq. (2.24)}$$

A recently developed phenomenological stress-state-dependent damage model is called the Generalized Incremental Stress State dependent damage Model (GISSMO) (Haufe *et al.*, 2010; Neukamm *et al.*, 2009). This model is implemented in the commercial finite element software LS-DYNA (Livermore Software, 2012) and has been used extensively by industry to predict fracture in vehicle crashworthiness simulation. For constant stress states, the damage rate can be integrated to get a relation of actual equivalent plastic strain and damage, as shown in the following Eq. (2.25):

$$D = \left(\frac{\varepsilon_p}{\varepsilon_f}\right)^{D_{exp}} \qquad \text{Eq. (2.25)}$$

in which ε_p and ε_f are the instantaneous equivalent plastic strain during plastic deformation and equivalent plastic strain at failure, respectively, and D_{exp} is a damage exponent. An incremental description of damage accumulation, including softening and failure, can also be defined by the GISSMO damage model. The model for an incremental formulation of damage accumulation is shown in Eq. (2.26), while Eq. (2.26) is integrated to determine the current damage value, as shown in Eq. (2.27). Failure occurs once the value of the current damage reaches unity.

$$\Delta D = \frac{D_{exp}}{\varepsilon_f} D^{\left(1 - \frac{1}{D_{exp}}\right)} \Delta \varepsilon_p \qquad \text{Eq. (2.26)}$$

$$D = \int \frac{D_{exp}}{\varepsilon_f} D^{\left(1 - \frac{1}{D_{exp}}\right)} \Delta \varepsilon_p \qquad \text{Eq. (2.27)}$$

in which, ΔD is the incremental damage, D_{exp} is a damage exponent used for introducing non-linearity, $\Delta \varepsilon_p$ is the incremental plastic strain, and ε_f is the plastic strain at failure which is a function of Lode angle and stress triaxiality. The value of D is between 0 and 1. Unlike the JC fracture model, the GISSMO damage model has the capability to include the effect of both triaxiality and Lode parameter by defining ε_f using any triaxiality and Lode parameter dependent fracture criterion.

It is critical to perform tests for performing calibration of a fracture model considering different stress states (Kubík *et al.*, 2018). There are many fracture characterization tests available in the literature ranging from simple shear using mini-shear (Peirs *et al.*, 2012) or so-called "smiley" specimens (Roth and Mohr, 2015) to uniaxial tension tests utilizing hole expansion and hole tensile experimental procedures (Butcher *et al.*, 2013; Dunand and Mohr, 2010; Pathak *et al.*, 2017; Roth, 2015), as well as plane strain tension using tight-radius bend tests (Cheong *et al.*, 2017; Roth and Mohr, 2016) or dome tests with notched specimens (ISO-12004-2, 2008). Tests for combined shear and tension have also been developed using butterfly-type specimens (Anderson *et al.*, 2017; Dunand and Mohr, 2011; Mohr and Henn, 2007) and modified Arcan tests (Gruben *et al.*, 2011). Nakazima dome tests are more common for equal-biaxial tests (ten Kortenaar, 2016), though notch tension tests (Erice *et al.*, 2018) can also be performed to obtain fracture response under biaxial tension loading. The width of most of these test specimens is larger than the typical grip size of the elevated strain rate experimental equipment normally available for such work; therefore, the development of suitable specimen geometries for high strain rate fracture tests along with the development of proper experimental methods has been a part of the current research.

2.7   SUMMARY AND CURRENT DEFICITS IN LITERATURE

High strength aluminum alloy sheet has gained considerable interest in the automotive industry because of its low density and good specific properties. Numerical simulation is of key importance and it is necessary to accurately simulate these alloys prior to their introduction into vehicle structures. The accuracy of models for the simulation of aluminum alloys is dependent on the proper characterization of the material behavior. Thus, there exists a critical need to characterize and understand the response of high strength aluminum alloys under the elevated strain rate conditions associated with automotive crash

events. This need encompasses both constitutive response at elevated strain rate, including the effect of strain rate on flow stress and anisotropy, as well as the fracture behavior.

Several studies have reported a positive effect of strain rate on the constitutive response (strength) of 6000- and 7000-series aluminum alloys (Brar *et al.*, 2009; Chen *et al.*, 2009; Jurczak, 2012; Sasso *et al.*, 2015; Xiao *et al.*, 2016). The effect of plastic anisotropy on the constitutive behavior of the 6000- and 7000-series has also been examined (Choi *et al.*, 2021; Fourmeau *et al.*, 2011; Ha *et al.*, 2018; Prillhofer *et al.*, 2014; Tian *et al.*, 2017) but there is an evident need for further studies on this topic. Large plastic strains are often involved in sheet metal forming processes and techniques to extend measurements of work hardening beyond the onset of tensile necking instability are also needed. In the present research, shear tests will be utilized to examine work hardening at large strain levels, focusing on several high strength aluminum sheet alloys, AA6013-T6, AA7075-T6, and AA7xxx-T76.

At high rates of strain, the thermal softening effect due to deformation heating becomes significant because the heat generated by the high level of flow stress cannot be dissipated immediately due to the higher rate of deformation (Odeshi *et al.*, 2005; Pérez-Castellanos and Rusinek, 2012; Rusinek and Klepaczko, 2009; Vazquez-Fernandez *et al.*, 2019). The increase in temperature within the specimen gauge area produces a gradient in the strength of the sheet alloy which tends to increase the local strain and leads to localized necking. The temperature rise due to deformation heating at high rates needs to be characterized in order to develop accurate constitutive models. Infrared thermography to directly measure the temperature rise has been used by Pérez-Castellanos and Rusinek (2012) for an AA6082 extrusion, Nie *et al*. (2020) for AA7075-T6 plates, and Vazquez-Fernandez *et al*. (2019) for an austenitic stainless steel sheet alloy. Experimental data pertaining to the temperature rise in 7000-series aluminum sheet metal alloys due to deformation heating at high rates of strain has received only limited attention in the literature.

A clear influence of stress triaxiality and Lode angle on the ductile fracture strain is shown by Jang *et al*. (2020) and Chandran *et al*. (2021) for DP980 and DP1000 sheet, respectively. Similarly, Thomesen *et al*. (2020) and Lou *et al*. (2013, 2018) have shown a strong influence of stress state on the fracture behavior of 6000-series aluminum alloys and 2000- and 7000-series aluminum alloys, respectively. Studies conducted by Fang *et al.* (2021), Rahman *et al.* (2016), Hadianfard *et al.* (2008), and Higashi *et al.* (1991) have demonstrated that the fracture strain under tensile states increases with the increasing strain rate for aluminum alloys whereas the ductility of steels can increase or decrease depending upon the alloy system (Roth and Mohr, 2014; Winkler *et al.*, 2008). Roth *et al.* (Erice *et al.*, 2018; Roth and Mohr, 2014) and Mohr and Marcadet (2015) have reported the failure *loci* of steel alloys to shift upwards with strain rate for all stress triaxiality levels. It is important to note that the fracture behaviour of 6000- and

7000-series aluminum sheet alloys is largely unexplored for both low and high strain rate conditions which create the need for a systematic study of the fracture response of high strength aluminum alloys.

Studies by Roth *et al.* (2014, 2015, 2018) have considered the strain rate effect on the fracture strain of advanced high strength steels (DP590, DP980, TRIP780, CP980 and CP1180). In addition, a number of modelling approaches (Erice *et al.*, 2018; Roth and Mohr, 2015, 2014) for predicting fracture strain at high rates of strain have been proposed that make considerable use of a hybrid experimental–numerical modelling approach. Ha *et al.* (2018) investigated the plasticity and ductile fracture of bake-hardened AA6013 aluminum sheet under quasi-static condition and concluded that the fracture strain determination through a hybrid experimental–numerical modelling approach is highly sensitive to the constitutive model adopted. A thorough experimental-numerical investigation is needed to understand insights to reduce vehicle weight while preserving safety, ultimately promoting a positive environmental impact for the automotive industry.

From the consideration of the literature review and needs identified in this chapter, the specific research objectives are defined as follows:

- Develop a novel experimental methodology to obtain the hardening response up to larger levels of strain using tensile and shear tests incorporating detailed digital image correlation (DIC)-based strain measurements.
- Systematically investigate the constitutive response of the AA7075-T6, AA7xxx-T76, and AA6013-T6 sheet alloys from low (0.001 s^{-1}) to high (10^3 s^{-1}) rates of strain and utilize the experimental data for the development of a strain rate-sensitive constitutive model suitable for vehicle crash CAE models.
- Evaluate anisotropic yield functions based on a set of comprehensive experimental data for the three sheet alloys and propose appropriate yield criteria for FE simulation of high strength aluminum sheet alloys.
- Develop a fracture model to accurately capture the fracture strains of all three sheet alloys for stress states ranging from shear to equi-biaxial tension.
- Develop experimental methods to determine the temperature increase due to deformation heating within the specimen gauge region at elevated strain rates, and propose strain rate-sensitive constitutive and fracture models taking the adiabatic heat rise into account.

CHAPTER 3: EXPERIMENTAL METHODOLOGY

This chapter provides an overview of the adopted experimental techniques, which included constitutive and fracture characterization of three aluminum alloys under both quasi-static and dynamic conditions. The materials selected for this research include AA6013 in T6 temper, an intermediate strength 6000-series alloy, and two high strength alloys, AA7075 in T6 temper and a developmental 7000-series alloy, designated AA7xxx in T76 temper. Today, 7000-series alloys are used primarily in aerospace and armor applications; however, they have significant potential for application within light-weight automotive structural components. The developmental AA7xxx-T76 alloy has lower quench sensitivity, making it more appropriate for hot forming applications, as discussed by Omer *et al.* (2018). The as-received alloys have a nominal thickness of 2 mm, and Table 3 presents the typical chemical compositions of these alloys.

Table 3: Typical chemical composition of AA7075, AA7xxx, and AA6013 aluminum alloys (wt%) (Jabra *et al.*, 2006; Kafali and Ay, 2009).

	Zn	Mg	Cu	Ti	Mn	Si	Fe	Zr	Cr	Al
AA7075	6.35	1.92	1.46	0.03	0.02	0.05	0.1	-	0.1	bal.
AA7xxx	7.0–8.0	1.2–1.8	1.3–2.0	0.06	0.04	0.06	0.08	0.08–0.15	0.04	bal.
AA6013	0.04	0.92	0.86	0.02	0.34	0.7	0.28	<0.01	0.03	bal.

3.1   QUASI-STATIC CONSTITUTIVE CHARACTERIZATION

3.1.1   UNIAXIAL AND SHEAR TESTS

Both uniaxial tensile and shear tests were performed as part of the constitutive characterization effort. This section of the synopsis provides an overview of the test techniques and specimen design, while further details of the methodologies can be found in Appendices A and B.

The uniaxial tensile tests were performed on mini-dogbone specimens (Figure 9), developed to facilitate both low and high strain rate testing (Bardelcik *et al.*, 2012; Smerd *et al.*, 2005; Thompson, 2006). The samples were fabricated and tested with the tensile axis at seven different orientations with respect to the sheet rolling direction (0°, 15°, 30°, 45°, 60°, 75°, and 90°).
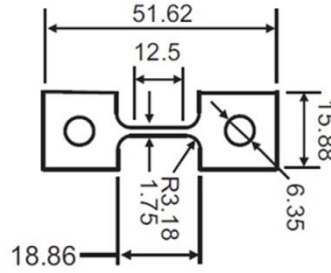
Figure 9: Miniature dogbone specimen used for uniaxial tensile tests.

Diffuse necking occurs at relatively low strain levels in the tensile tests, preventing the accurate measurement of the flow stress *versus* effective plastic strain response at larger strains. On the other hand, the material response can be obtained up to large plastic strains from shear tests without experiencing localized necking until fracture. The so-called "mini-shear" specimen geometry developed by Peirs *et al.* (2012, 2011a, 2011b), as shown in Figure 10, was used for the shear tests in the present work, along with DIC measurements to obtain the local shear strain. The advantage of this geometry is that a relatively uniform shear strain distribution can be achieved and the specimen does require through-thickness machining, making the fabrication relatively simple. Recently, Abedini *et al.* (2017, 2015) have compared the mini-shear specimen of Peirs *et al.* (2012, 2011a, 2011b) and butterfly-type shear specimen of Mohr and Henn (2007, 2004), and demonstrated that the mini-shear specimen can be used for both fracture and constitutive characterization. To account for the principal directions in the shear test being located at ±45° to the applied shear direction and the 11° eccentricity between the notches, the shear specimens were extracted at −56° to the rolling direction.
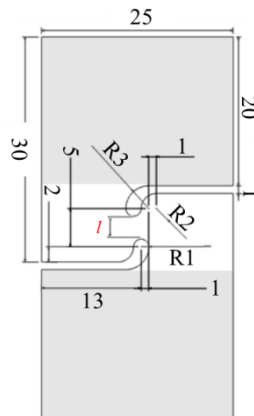
Figure 10: Mini-shear specimen geometry (Peirs *et al.*, 2012, 2011a, 2011b). The shear region, $l = 3$ mm, and the grip region is indicated with the shaded regions. Dimensions are in mm.

A primary focus in this work was the development of a novel methodology to experimentally obtain the stress-strain behaviour to large levels of strain (without inverse modelling techniques) in which the shear

tests were utilized to extend the uniaxial test data. Although the current research was focused on high strength aluminum alloys, preliminary studies for the shear to equivalent stress-strain data conversion technique were undertaken using more ductile sheet alloys (AA5182-O and DP600), as described in Appendix A, and later implemented for the current 6000- and 7000-series aluminum alloys, as shown in Appendix B. In the current work, a process to convert the measured experimental shear data to tensile data was developed which avoids the need to select a yield criterion although it does assume isotropic hardening of the material. An equivalent plastic work methodology was adopted, as detailed in Appendix A. For a given plastic work, the ratio of stress under shear loading to the stress under uniaxial tensile loading along the sheet rolling direction $(\sigma_{shear}/\sigma_{eq})$ was determined. Once this ratio was determined (averaged) for the range of plastic work in the tensile test (up to diffuse necking), it was assumed to be constant and was then applied to convert the entire shear stress-strain curve to uniaxial data using Eq. (3.1) and Eq. (3.2) (Butcher and Abedini, 2017).

$$\sigma_{eq} = \left(\frac{F}{A_s}\right)\left(\frac{\sigma_{eq}}{\sigma_{shear}}\right) \qquad \text{Eq. (3.1)}$$

$$\varepsilon_{eq}^p = 2\left(\frac{\sigma_{shear}}{\sigma_{eq}}\right)\sinh\left(\varepsilon_1 - \frac{\sigma_{shear}}{2G}\right) \qquad \text{Eq. (3.2)}$$

The shear extrapolation results using this approach are presented in Section 4.1.2 of this synopsis, as well as in Appendices A and B.

3.1.2 CHARACTERIZATION OF BIAXIAL YIELD CONDITIONS

As an alternative to cruciform (Kuwabara *et al.*, 1998) or hydraulic bulge (Young *et al.*, 1981) tests to characterize biaxial yield response, the through-thickness compression test is a simple method to measure the work hardening behavior in the biaxial stretching state, as discussed by Steglich *et al.* (2014). Specimens built from adhesively-bonded layers of sheets (Figure 11) were used for through-thickness compression testing. The cubic specimens were fabricated by adhesively bonding six layers of sheet using J-B-Weld® adhesive. Prior to applying adhesive, Acetone was used to carefully clean the sheet mating layers. Once the adhesive was cured for 24 hours, the specimen surfaces (both top and bottom) that contact the compression platens were polished to a mirror-finish.
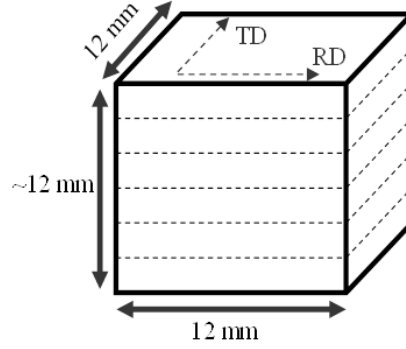
Figure 11: Through-thickness compression specimen used to characterize the work hardening behavior in the biaxial stretching state.

Teflon® spray was applied on the specimen surfaces as a lubricant to reduce friction, and friction coefficients of 0.075, 0.061, and 0.077 were used for AA7075-T6, AA7xxx-T76, and AA6013-T6, respectively, based on data reported by Noder (2017). A correction process developed by Dieter *et al.* (2003) was applied to the compression test data to account for frictional effects when calculating the true flow stress, σ_{True}, as shown in the following equation:

$$\sigma_{true} = \sigma_{measured}\left(1 + \frac{fD}{3\sqrt{3}h}\right)^{-1}$$

Eq. (3.3)

where, $\sigma_{measured}$ is the measured stress data from the tests, h is the current height of the specimen in the compression direction, D is the area-equivalent diameter, and f is the interface friction coefficient, taken as 0.08, 0.06, and 0.08 for AA7075-T6, AA7xxx-T76, and AA6013-T6, respectively, (Noder, 2017).

To determine the average equal-biaxial *r*–values of sheet alloys, 10 mm diameter single layer circular disks were compressed in the through-thickness direction. The change in diameter was used to obtain the in-plane strains and biaxial *r*–value. Barlat *et al.* (2003) and Tian *et al.* (2017) have demonstrated this method to work well to determine the equal-biaxial *r*–values for AA2090-T3 and AA6022-T4 sheet alloys, respectively. Teflon® spray was used to lubricate the discs that were compressed between two hardened steel plates. The change in size of the disk specimens along the rolling and transverse sheet directions were measured by interrupting the compression test at different load levels. The logarithmic strains were calculated from the measured disc diameters, followed by the calculation of the average *r*–value under an equal-biaxial loading condition, using Eq. (3.4):

$$r_{EB} = \frac{\varepsilon_{TD}^{p}}{\varepsilon_{RD}^{p}}$$

Eq. (3.4)

3.2   HIGH STRAIN RATE CONSTITUTIVE CHARACTERIZATION

Uniaxial tension tests with dog-bone specimens, as shown in Figure 9, along different sheet orientations were used for constitutive characterization of the materials at dynamic strain rates ranging from 10 to 1,000 s^{-1}. The experimental data from the dynamic tensile tests provided the effected of strain rate on the flow stress, as well as on the plastic anisotropy.

Peirs *et al.* (2012, 2011a, 2011b) showed that the mini-shear specimen can also be adapted to high rate tests. However, the grip size of the elevated strain rate testing apparatus available at the University of Waterloo was smaller than the 25 mm width of the mini-shear specimen. Therefore, a miniature version of the mini-shear specimen geometry of Peirs *et al.* (2012, 2011a, 2011b), referred to as the "micro-shear specimen", was developed with a 16 mm width and utilized in the high rate tests. The geometry of the micro-shear specimen is shown in Figure 12. A thorough validation study was performed for the micro-shear specimen as a part of this work, in this case using more ductile AA5182-O sheet metal alloys (see Appendix A for further details of the specimen design process). The test data obtained with the micro-shear and mini-shear specimens demonstrated very good agreement under quasi-static conditions, as shown in Appendix A.
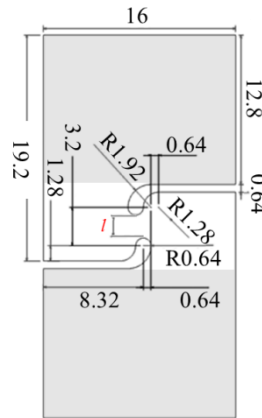
Figure 12: Micro-shear specimen geometry. The shear region, *l* = 1.92 mm, and the grip area is indicated by the shaded regions. Dimensions are in mm.

3.3   QUASI-STATIC FRACTURE CHARACTERIZATION

Quasi-static tests were performed to characterize the fracture strain of the selected high strength aluminum alloys as a function of stress triaxiality and Lode angle parameter. The particular fracture tests were chosen to encompass four characteristic stress states, namely, shear, uniaxial tension, plane strain tension, and biaxial tension.

In the present study, the quasi-static shear fracture strains were measured from the simple shear tests using the mini-shear specimen, as shown in Figure 10. In simple shear tests, the principal strain components, ε_1 and ε_2, were measured within the gauge area (length l in Figure 10), while the maximum shear strain (ε_{12}^{max}) was calculated using Eq. (3.5). These strain components are not dependant on the choice of yield function and are valid for plastic deformation until fracture, as discussed in Appendix A.

$$\varepsilon_{1,2} = \pm\varepsilon_{12}^{max} = \pm\sqrt{\varepsilon_{11}^2 + \varepsilon_{12}^2} \qquad \text{Eq. (3.5)}$$

To obtain uniaxial tensile failure strains, a conical hole expansion test using a conical punch was used. A constant proportional loading induced by a conical punch at the top edge of the expanding hole up until material fracture produces a consistent stress state that remains close to uniaxial tension (Stachowicz, 2008). Therefore, this test has been commonly utilized to characterize material fracture response for uniaxial tensile loading cases (Pathak, 2015; ten Kortenaar, 2016). The specimen geometry for this test is shown in Figure 13. The specimen incorporates a 10 mm diameter reamed hole (to avoid the effect of a sheared edge) at the centre of a 127 mm x 127 mm (5" x 5") blank. The punch side of the specimen was lubricated with a thin layer of petroleum jelly before placing on a MTS formability press to minimize the friction effect. Further detail regarding the preparation of the specimen for conical hole expansion tests is provided in Appendix C. The equivalent fracture strain was determined for the hole expansion test utilizing the initial diameter of the hole (D_i) and the measured outer diameter of the hole at the moment of crack initiation $\left(D_{f,outer}\right)$, as shown in Eq. (3.6):

$$\varepsilon_1 = \varepsilon_{eq} = \ln\frac{D_{f,outer}}{D_i} \qquad \text{Eq. (3.6)}$$

a. Top view (un-deformed)   b. Side view (deformed)
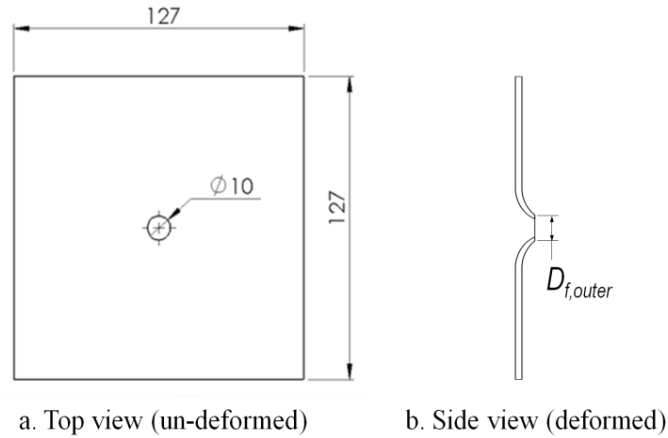
Figure 13: (a) Top view of un-deformed specimen geometry used for the hole expansion test. All dimensions are in mm. (b) a side view schematic of the deformed specimen indicating the outer diameter of the hole where fracture strain is measured.

   The plane strain notch tension test is one of the common methods for fracture characterization of sheet metal under plane strain tension loading condition. Due to the onset of diffuse necking, the stress state at fracture in the notch test is best described as plane strain tension under a triaxial (3D) stress state than plane stress. As an alternative to the traditionally used Nakazima plane strain dome tests (Nakazima *et al.*, 1968), Roth and Mohr (2016) employed a tight radius v-bend experiment based on the VDA238-100 (2017) specifications for plane strain fracture characterization, and showed that for advanced high strength steels a constant stress state can be maintained throughout the entire loading history up to the fracture initiation. Cheong et al (2019; 2018) reported that the presence of through-thickness strain gradient in the v-bend specimen effectively suppresses necking. In the present work, v-bend tests were performed to identify the fracture strain in plane strain stress state. Figure 14 shows a schematic showing the details of the v-bend experimental setup. The v-bending tests were performed following the standardized procedure developed by Cheong *et al.* (2019; 2018) with the specimens consisted of 50 mm x 50 mm blanks and a punch with a 0.43 mm tip radius. The VDA method (Cheong, 2019; Cheong *et al.*, 2018) with 30N load drop criteria to obtain the fracture strain data from the v-bend tests.
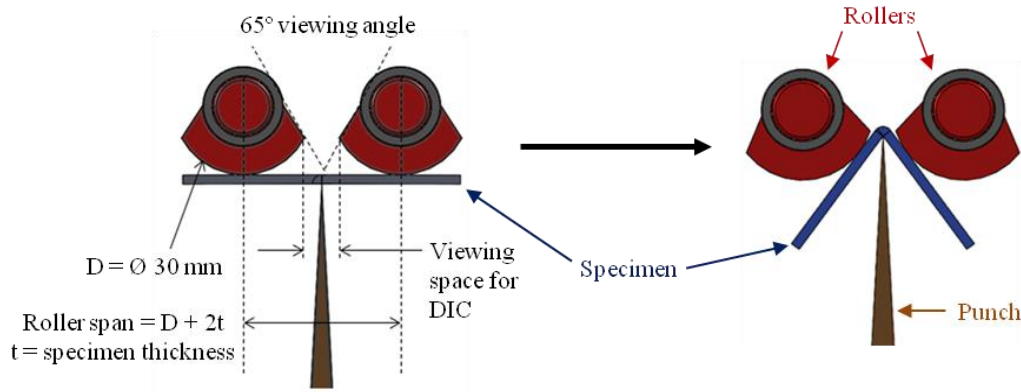
Figure 14 : A schematic showing the experimental setup for the VDA238-100 bend test (Cheong *et al.*, 2018).

Equal-biaxial dome tests were performed on all three sheet alloys using the miniature punches developed by Cheong *et al.* (2019; 2018) with punch radii of 5, 10, and 25mm. With the classical 50.8 mm punch radius used in Nakazima tests, the amount of bending is less severe and a tensile instability (necking) can arise prior to fracture which alters the stress state. Three smaller punch radii were considered to identify the punch size that suppressed necking due to the imposed biaxial bending and produced an approximate linear strain path of equal-biaxial stretching for the sheet alloys considered herein. The equal-biaxial samples were prepared with 203.2 mm x 203.3 mm blanks. In order to minimize the friction effect and maintain consistency in the experimental results, three layers of Teflon sheet along with petroleum jelly were applied between the specimen and the punch. In this work, the equal-biaxial fracture strains for material fracture characterization were selected from the test condition that provided the strain path nearest to the theoretical strain path and exhibited a fracture location reasonably close to the dome apex.

Figure 15: Punches used for equal-biaxial dome tests. From left to right: 5 mm, 10 mm, 25 mm, and 50.8 mm in radius Cheong *et al.* (2019; 2018).

The work-conjugate equivalent strain for the plane strain and equal-biaxial tests in plane stress proportional loading can be calculated using Eq. (3.7):

$$\varepsilon_{eq} = \frac{\sigma_1}{\sigma_{eq}} \varepsilon_1 (1 + \alpha\rho) \qquad \text{Eq. (3.7)}$$

where the ratio of principal stresses, α, and the ratio of principal strains, ρ, are defined as:

$$\alpha = \frac{\sigma_2}{\sigma_1} \qquad \text{and} \qquad \rho = \frac{\varepsilon_2}{\varepsilon_1} \qquad \text{Eq. (3.8)}$$

To obtain equivalent strain data for anisotropic yielding for the plane strain and equal-biaxial tests, a relatively simple methodology was developed using a closed form equation based on the Hosford yield criterion, as shown in Eq. (3.9). The Hosford yield criterion was selected due to its simple analytical form. The strain ratio is a function of the tensile r-values and yield exponent

$$\rho = \frac{r_0 \alpha^{a-1} + r_0 r_{90} |\alpha - 1|^{a-1}}{r_{90} + r_0 r_{90} |1 - \alpha|^{a-1}} \qquad \text{Eq. (3.9)}$$

in which the exponent $a = 8$ for FCC materials. The derivation of Eq. (3.9) is provided in Appendix C.

3.4 HIGH STRAIN RATE FRACTURE CHARACTERIZATION

The high strain rate fracture characterization was limited to the AA7075-T6. The high rate shear tests utilized the micro-shear geometry, a scaled down version of the mini-shear required for the high rate apparatus, shown in Figure 12. Hole tension (HT), notch tension (NT), and groove tension (GT) specimen geometries, as shown in Figure 16, at strain rates ranging from 0.01 to 500 s^{-1} were also performed to obtain stress states between uniaxial tension to biaxial tension. All specimens were CNC machined with the rolling direction aligned with the axial loading direction. These new samples were adopted for the high rate tests since the quasi-static sample geometries could not be easily adapted for dynamic testing. Further description of the dynamic fracture tests is given in Appendix D.
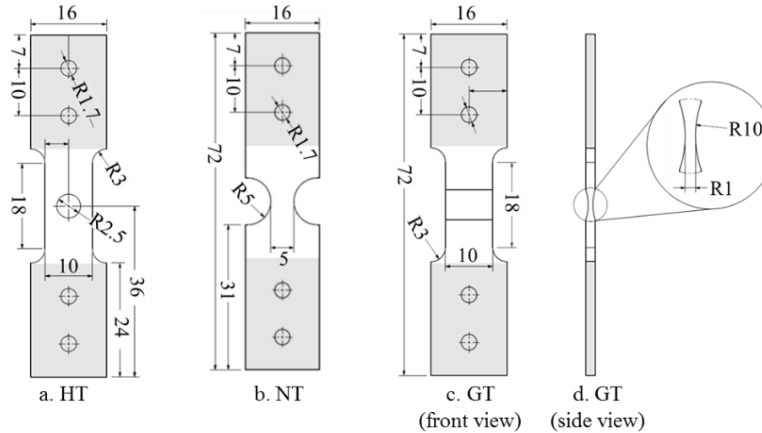
Figure 16: Specimen geometries used for the tests ranging from low to high: (a) hole tension specimen, (c) notch tension specimen, (d) front view of the groove tension specimen and (d) the front view of the groove tension specimen. Grip area is shown with the shaded regions. Dimensions are in mm.

3.5   APPARATUS, STRAIN AND TEMPERATURE MEASUREMENT

The quasi-static uniaxial tensile and shear tests were performed using a servo-mechanical MTS criterion model 45 testing frame fitted with a 100 kN load cell. An Instron model 1331 servo-hydraulic testing machine was used to perform the through-thickness compression and disc compression tests. An MTS formability press consisting of a 106 mm inner diameter die with a profile radius of 6.35 mm and a 106 mm inner diameter binder was used to perform the conical hole expansion tests, as well as the dome tests. The die set did not have a lockbead and a 640 kN clamping load was found to be sufficient to mitigate material draw-in.

The intermediate strain rate (10 and 100 s^{-1}) uniaxial tensile tests and the intermediate (10 s^{-1}) and high strain rate (500 s^{-1}) shear, hole tension, notch tension, and groove tension tests were performed using a Hydraulic Intermediate Strain Rate (HISR) apparatus developed at the University of Waterloo. A KISTLER piezoelectric load cell with a sampling rate of 250,000 samples/s was used to measure the load. A detailed description of the HISR apparatus can be found in the work presented by Bardelcik (2012).

A tensile split Hopkinson bar (TSHB) apparatus was used to perform the uniaxial tensile tests at a strain rate of 1,000 s^{-1}. For brevity, the apparatus is not described here in detail, but the testing arrangement and analysis of the data follows the classical Hopkinson bar technique (Gray III, 2000) that enables acquisition of the engineering stress-strain curves and strain rate history from each test. The reader is referred to the work presented by Smerd *et al.* (2005) and Salisbury (2001) for a detailed description of the apparatus and data reduction methods.

In situ digital image correlation (DIC) measurements were used to record strains up to the onset of failure. The DIC technique was employed to capture the strains on the surface of the specimens using the Vic-3D-7 software from Correlated Solutions Inc ("Vic-3d Software Manual," 2021). The DIC data acquisition system was employed to simultaneously acquire the load cell signal and synchronize with the video images. The measured strains from the DIC software were then used to calculate the equivalent strains. Point Grey Research GRAS-50S5M-C cameras and Photron FASTCAM SA5 high speed cameras were used for the quasi-static and dynamic strain rate conditions, respectively. The DIC hardware and analysis parameters corresponding to each specimen and strain rate tests are shown in detail in Appendices A-D.

The full-field logarithmic (true) strains were acquired and calculated using the incremental correlation option available in the Vic-3D software to account for severe local strains. A Virtual Strain Gauge (VSG), as defined in Eq. (3.10), value of 0.7 mm was used for all of the DIC analysis to maintain consistency among the reported strain values. Further detail concerning the DIC extraction process and data analysis methods for the fracture strains can be found in Appendices C and D.

$$VSG\ (mm) = Image\ Scale\ (mm/px) \times [(Step\ Size\ (px) \times (Strain\ Filter - 1))$$
$$+ Subset\ Size\ (px)]$$

Eq. (3.10)

One of the critical aspects of the present work was to correctly account for the heat converted from the plastic work at dynamic strain rate levels. This task included the development of an experimental procedure to capture the temperature increase at large strains and strain rates due to plastic deformation using a high speed infrared camera. A mid-wavelength (λ = 3–5μm) Telops IRC-TS series high speed infrared radiation (IR) camera was used to measure the temperature changes on the specimen surface due to the plastic deformation in the dynamic strain rate tests. The camera parameters for each specimen and strain rate are given in Table 4.

Table 4: Summary of IR camera system parameters.

Stain Rate (s⁻¹)	10				500			
Tests	SH	HT	NT	GT	SH	HT	NT	GT
Camera Manufacturer and Model	Telops IRC TS-IR-2K							
IR Software name and Manufacturer	HypIR, Telops							
Lens Manufacturer, Model, focal Length	Telops bayonet mounted lens, f/2.3, 150 mm							
Painting Technique	Black paint with Rust-Oleum Ultra Cover Flat Primer							
Frame Rate (fps)	5,000	8,400		6,000	40,000	38,000		28,000
Image Size (px)	128 x 128	64 x 196	128 x 128	128 x 188	64 x 24	64 x 28		64 x 52

The surface of the specimen viewed by the IR camera was painted black with Rust-Oleum® Painter's Touch 340g Ultra Cover Flat Primer to achieve a surface closer to a blackbody. The temperature of the surrounding (T_{surr}) is taken as 23ºC herein, while the captured temperatures of the specimen (T_b) using the Telops IRC-TS series high speed infrared radiation (IR) camera has been input to Eq. (3.11) to measure the actual temperatures of the specimen (T_S) specimens during deformation. A detailed derivation of Eq. (3.11) is provided in Appendix D. A Bruker FT-IR spectrometer was used to measure the directional hemispherical reflectance of the unpainted AA7075-T6 sheet surface, as well as for the AA7075-T6 sheet painted in black. The emissivity (ε^r) and reflectivity (ρ) are related by $\varepsilon^r = 1 - \rho$. The average emissivity of AA7075-T6 specimen with black paint is found to be approximately 0.95, and approximately 0.05 for the unpainted surface, which is similar to what has been reported by Touloukian and DeWitt (1970) and Minkina and Dudzik (2009) for aluminum alloys.

$$T_S = \left[\frac{1}{\varepsilon^r} (T_b^4 - \rho T_{surr}^4) \right]^{1/4} \qquad \text{Eq. (3.11)}$$

CHAPTER 4: RESULTS

4.1   CONSTITUTIVE CHARACTERIZATION

This section presents the key results of the low and high rate constitutive characterization tests, including the shear extrapolation of the uniaxial tensile data and the biaxial yield (through-thickness compression) test results. Note that a more detailed narrative describing this data is presented in Appendices A and B.

4.1.1   EFFECT OF STRAIN RATE ON CONSTITUTIVE BEHAVIOR

The effect of strain rate on the flow stress versus effective plastic strain measured along the rolling direction of the AA7075-T6, AA7xxx-T76, and AA6013-T6 samples is shown in Figure 17(a-c). (Note that the presentation here focuses on flow stress data using true stress-strain data. The trend in the engineering stress-strain behavior was found to be similar for all sheet orientations at all of the strain rates, as shown in Appendix B.) All three materials exhibited a mild increase in strength with increasing rate of strain. The hardening response, or the shape of the flow stress curve, does not change significantly with strain rate and the yield strength scales upwards with the strain rate. The average true stress as a function of strain rate at 6% equivalent plastic strain is plotted for the three alloys in Figure 17d, with the error bars indicating the minimum and maximum measured data points from the population of three to five repeat tests. Slightly higher error bars are observed for the 1,000 s^{-1} strain rate condition due to minor oscillations within the stress signal as measured using the TSHB apparatus. The effect of strain rate on the true stress was similar for all other test orientations.
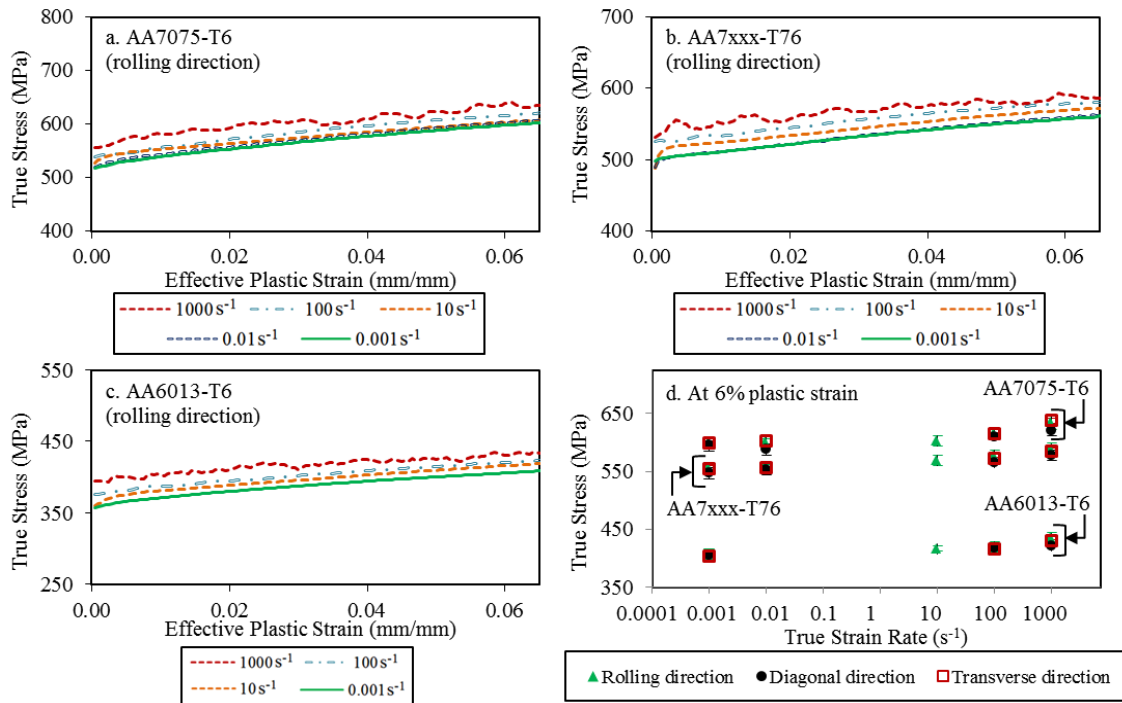
Figure 17: Averaged flow stress curves at room temperature and strain rates from 0.001 s^{-1} to 1,000 s^{-1} along rolling direction for (a) AA7075-T6 (b) AA7xxx-T76 and (c) AA6013-T6 sheet alloy and (d) variation of true stress with true strain rate at 6% effective plastic strains for all three sheet alloys along rolling direction (RD), diagonal direction (DD) or 45° to RD, and transverse direction (TD) or 90° to RD.

The AA7075-T6 and AA7xxx-T76 sheet alloys demonstrated much higher strength as compared to the AA6013-T6 sheet material, while the peak aged AA7075-T6 exhibited the highest strength. The level of anisotropy evident in the flow stress data (Figure 17d) was low.

Figure 18 summarizes the variation in *r*–value with orientation for each alloy. Although all three materials exhibited relatively low anisotropy in the flow stress, significant normal and planar anisotropy was observed. The *r*–value was largest in the TD for each alloy. The largest variation in *r*–value was observed for the AA7xxx-T76, ranging from 0.56 at 15° to 1.87 at 90 °.

40
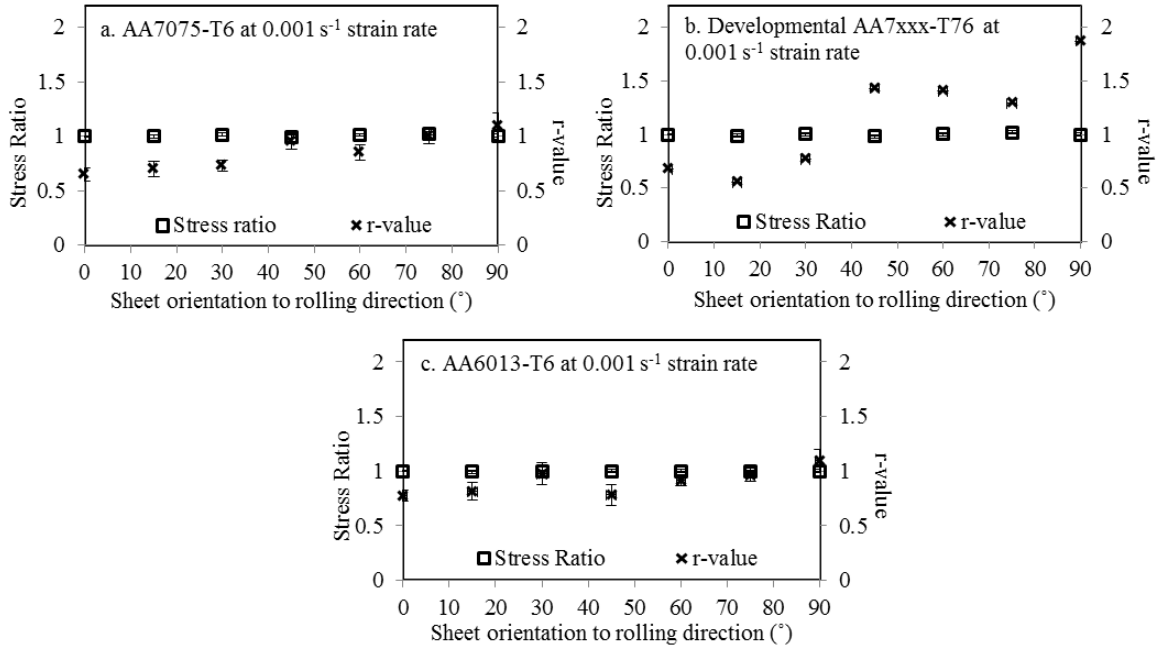
Figure 18: Stress ratio and r–value along different sheet orientations (0˚ to 90˚ to the rolling direction) for (a) AA7075-T6, (b) AA7xxx-T76, and (c) AA6013-T6 at 0.001 s^{-1} strain rate.

The measured flow stress and *r*–values at various strain rates were further investigated to understand the effect of strain rate on anisotropy. Figure 19(a) shows the true stress under uniaxial tension in each material direction normalized by the true stress in the sheet rolling direction (the data corresponds to that shown in Figure 17). The flow stress data were taken at an effective plastic strain of 0.06 for all three materials. As shown in Figure 19, a definite trend with respect to strain rate has not been observed, suggesting that the dependence of anisotropy on strain rate is not significant. As shown in Figure 19(b), the magnitude of the r-values and stress ratios at elevated strain rate remain close to the quasi-static result. Although the hardening behavior is dependent upon the strain rate, anisotropy in terms of the relative yield stresses and r-values can be assumed to be independent of the strain rate. Consequently, the anisotropic yield loci calibrations (presented in Section 4.2.2) were based on quasi-static data.
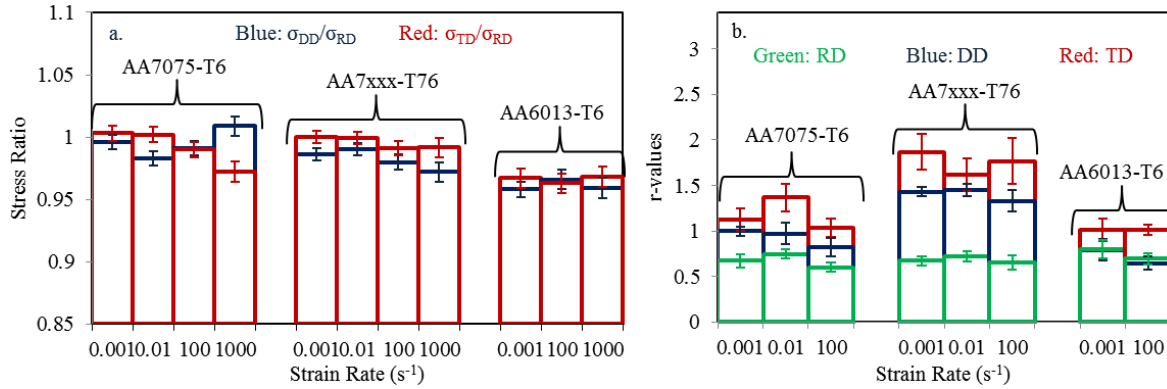
Figure 19: Variation of (a) in-plane anisotropy (stress ratios) and (b) r-value with strain rate for AA7075-T6, AA7xxx-T76, and AA6013-T6 sheet metal alloys. The r-value determination for the AA6013-T6 sheet alloy was limited to strain rates of 0.001 and 100 s^{-1}.

4.1.2   SHEAR EXTRAPOLATION OF STRESS-STRAIN CURVES

A key advantage of shear tests is the potential to obtain constitutive data beyond the strain to necking experienced in uniaxial tensile tests. This difference is illustrated in Figure 20 which shows tensile and shear stress-strain data for AA7075-T6, AA7xxx-T76, and AA6013-T6.
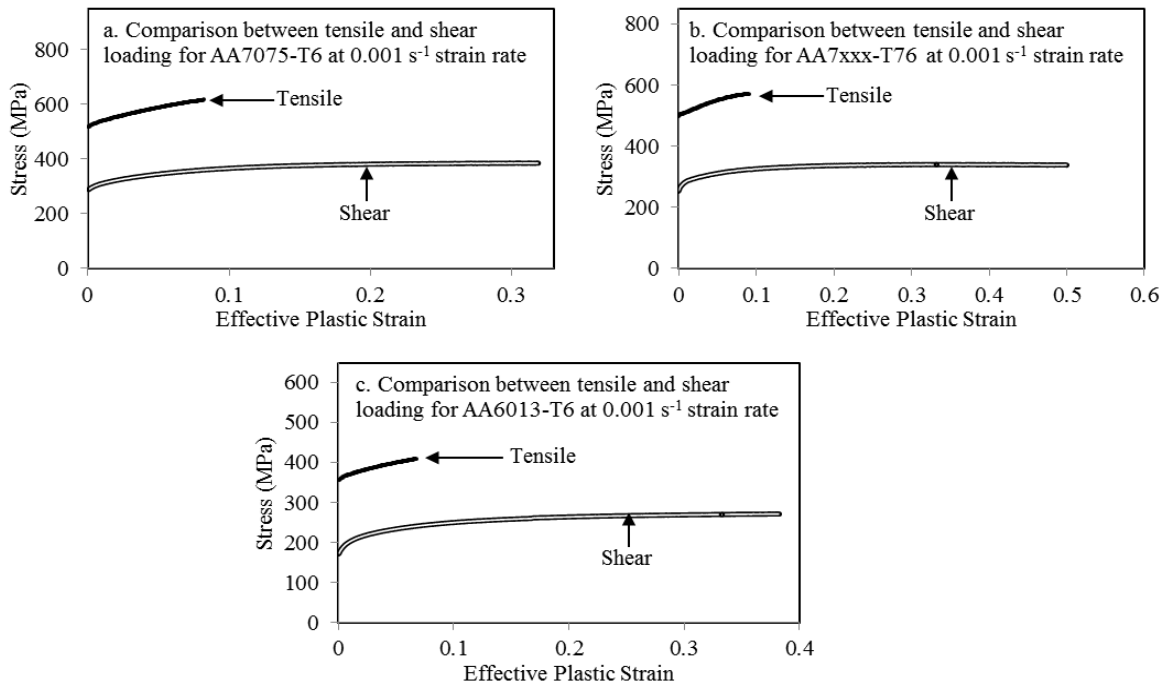
Figure 20: Comparison between tensile and shear experimental data showing much larger effective strain levels in shear testing than that achieved during uniaxial tensile testing for (a) AA7075-T6, (b) AA7xxx-T76, and (c) AA6013-T6 sheet alloy.

42

Using the data in Figure 21, the average shear stress ratios were found to be approximately 0.58 for AA7075-T6 and AA7xxx-T76 and 0.57 for AA6013-T6 in close accord with the value of 0.577 using a von Mises yield assumption. Utilizing these values in the shear to equivalent stress-strain conversion method, Eq. (3.1) and Eq. (3.2), the shear stress-strain data measured for the AA7075-T6, AA7xxx-T6, and AA6013-T6 was converted to equivalent stress-strain data. The shear conversion method is independent of yield function, as shown in Appendix A. Good agreement is seen between the shear-derived effective stress-strain and uniaxial tensile responses up to the limit of the tensile data, as seen in Figure 21, for all three sheet alloys tested at a strain rate of 0.001 s^{-1}.
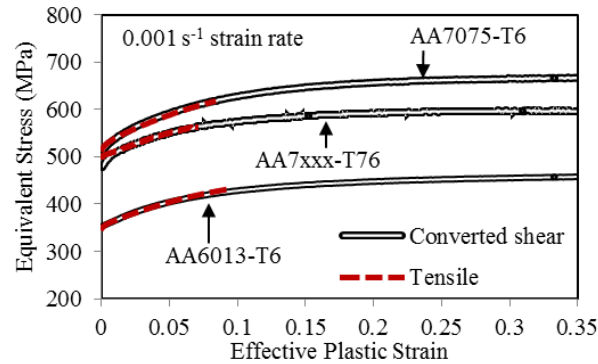
Figure 21: Comparison of the effective stress-effective plastic strain response derived from shear and uniaxial tensile tests at a strain rate of 0.001 s^{-1}.

Shear tests of the AA7075-T6 were also performed using the micro-shear specimens for strain rates ranging from 0.01 to 500 s^{-1}. Figure 22 compares the uniaxial tensile data (up to UTS) with the converted shear data at comparable von Mises equivalent strain rates. The agreement between the hardening response from the shear and uniaxial tension tests is found to be reasonable for the AA7075-T6 sheet for most of the strain rates considered, with a somewhat lower agreement at the highest strain rate. Similar to the uniaxial tensile data (shown in Figure 17), the converted shear data exhibited mild positive strain rate sensitivity in the equivalent stress-strain response at the beginning of the plastic deformation, as seen in Figure 23. However, as the level of equivalent plastic strain increases beyond approximately 20%, the effect of strain rate on the hardening response of the material drops as the strain level increases. The reduced rate sensitivity is largely attributed to thermal softening effects as deformation becomes more adiabatic with increased rate of strain.
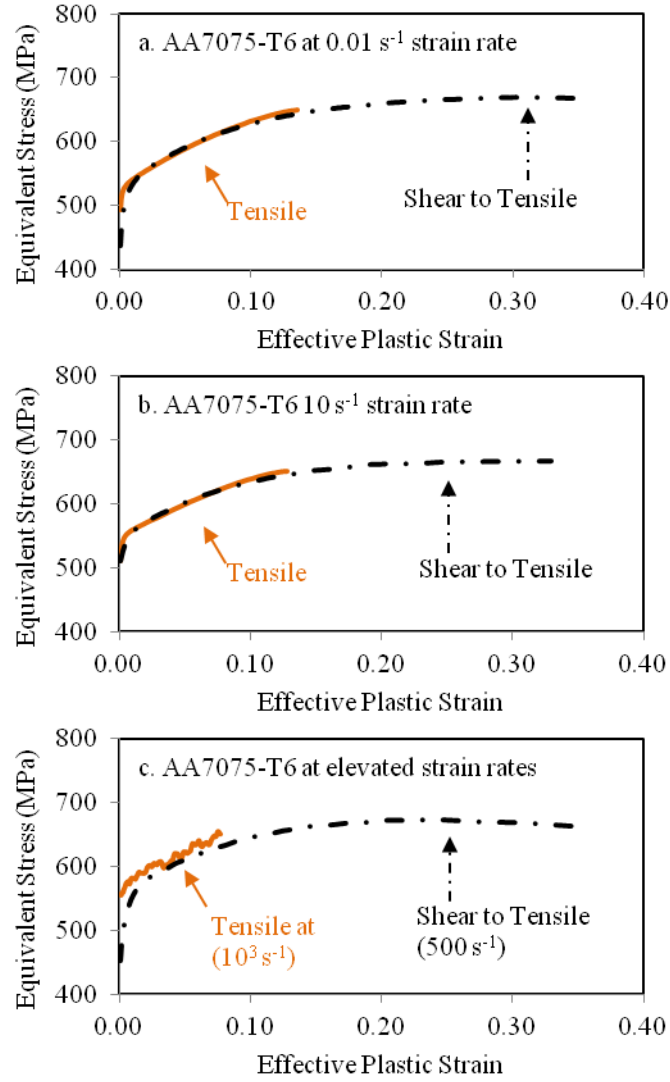
Figure 22: Effective stress-effective plastic strain response for the AA7075-T6 sheet alloy derived from tensile and shear tests at strain rates ranging from 0.01 to 500 s^{-1}.
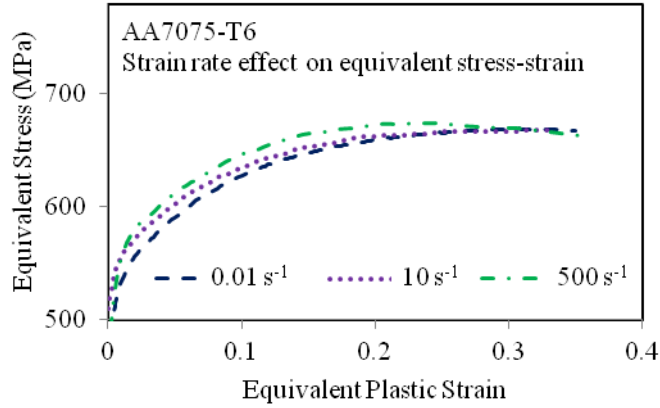
Figure 23: Effect of strain rate on the equivalent stress-equivalent plastic strain response derived from shear tests at strain rates ranging from 0.01 to 500 s^{-1}.

The temperature rise on the surface of the shear specimens was examined using infrared techniques (as described in Section 3.5) for strain rates of 10 and 500 s^{-1}. The lowest strain rate of 0.01 s^{-1} was assumed to be isothermal. As shown in Figure 24 (right) for a 500 s^{-1} strain rate test, the temperature rise occurred at the centre of the shear gauge region. The total temperature rise was found to be much lower at 10 s^{-1} (approximately 12°C) compared to the test at 500 s^{-1} (approximately 40°C), as shown in Figure 24 (left). The decrease in strength with increasing strain rate (shown in Figure 23) can be attributed to the increase of temperature due to the conversion of plastic deformation energy into heat and limited time for conduction at the higher rate, resulting in an induced softening.
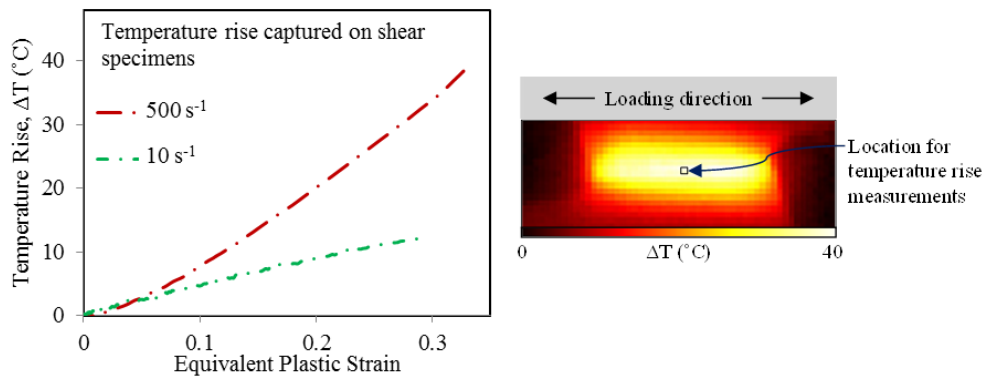
Figure 24: (Left) Temperature rise history of the AA7075-T6 shear specimens as a function of equivalent plastic strain at strain rates of 10 and 500 s^{-1} and (right) a contour plot of measured temperature rise within the gauge region of a shear specimen at a strain rate of 500 s^{-1}.

4.1.3 BIAXIAL CHARACTERIZATION RESULTS

The experimental stress-strain data from the through-thickness compression tests for the three materials are shown in Figure 25. The effect of friction between the platens and specimen surfaces on the flow

45

stress response was found to be small (less than 2%). The biaxial stress ratios were determined by normalizing the through-thickness compression stress with the tensile stress in rolling sheet direction. Equal-biaxial stress ratios (ratio of biaxial to RD uniaxial yield stress) of 1.021, 1.019, and 1.000 were calculated for AA7075-T6, AA7xxx-T76, and AA6013-T6, respectively. The equal-biaxial stress ratios were measured at effective plastic strains of 4.5%, 6.5%, and 5% for the AA7075-T6, AA7xxx-T76, and AA6013-T6, respectively. The average biaxial r-values were 0.92 $\pm$0.02, 0.71 $\pm$0.08, and 0.60 $\pm$0.03 for AA6013-T6, AA7075-T6, and AA7xxx-T76, respectively.
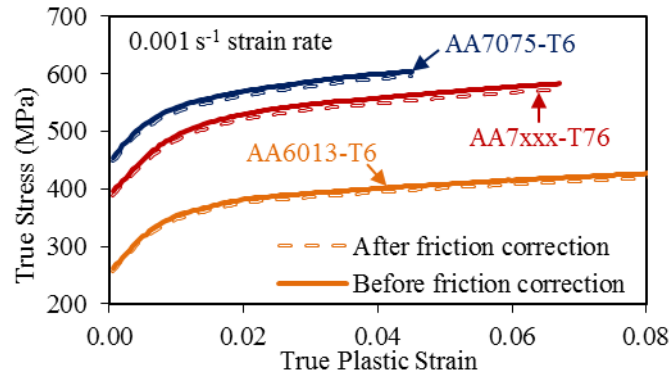
Figure 25: Stress-strain response of AA7075-T6, AA7xxx-T76, and AA6013-T6 under equal-biaxial tension (through-thickness compression) loading, as detailed in Appendix B.

4.2   CONSTITUTIVE MODEL DEVELOPMENT

As presented in Section 4.1, the significant anisotropy and dependency of stress on the strain rate for the 6000- and 7000-series aluminum alloys highlights the need for the development of an accurate constitutive model. A phenomenological plasticity modelling approach is taken in the current work. Assessment of the predictive capabilities of the developed model was done by comparison of predictions with tests, both in terms of macroscopic load-displacement response as well as local stress/strain predictions. A summary of the plasticity model development and resulting accuracy of the model is presented in this section, while more detailed explanations can be found in Appendices B and D.

4.2.1   HARDENING RESPONSE CALIBRATION

Three variations of the Hockett-Sherby hardening model (Hockett and Sherby, 1975) were fit to the experimental data. The simplest approach utilized the original Hockett-Sherby model, given by Eq. (4.1), that was fit using the equivalent stress-effective plastic strain data obtained from uniaxial tensile tests, as well as converted from the quasi-static shear tests. The next level of complexity entailed the development of a strain rate dependent Hockett-Sherby model that was fit to the high strain rate experimental data obtained from the uniaxial tensile tests. The most complex model comprised the development of a strain

rate and temperature dependent version of the Hockett-Sherby model that was fit to the equivalent stress-effective plastic strain data from the high strain rate shear tests.

4.2.1.1 BASELINE HOCKETT-SHERBY MODEL FIT

The baseline Hockett-Sherby model is given by

$$\sigma_{HS}(\varepsilon_p) = \sigma_S - (\sigma_S - \sigma_Y)\exp{(-N\varepsilon)^P} \qquad \text{Eq. (4.1)}$$

where, σ_Y is the yield stress, σ_S is the steady-state flow stress, and N and P are material constants. The material constants were fit to the equivalent stress-effective plastic strain data developed from the quasi-static tension and shear tests (Figure 21) since these data encompass a larger range of strain than in the uniaxial tensile tests (Figure 17). A non-linear regression analysis was performed for the model fitting using the statistical analysis software MYSTAT. As shown in Figure 26, excellent agreement between the model and test data with the calibration parameters provided in Table 5. Figure 26 also shows the extrapolation using the Hockett-Sherby model, which exhibits a saturation-like behavior at large strain levels.
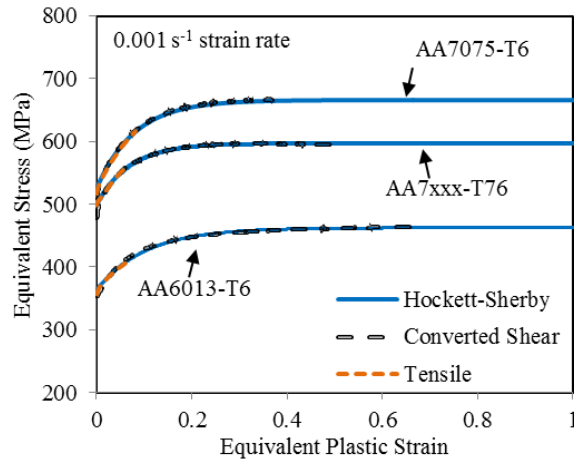
Figure 26: Hockett-Sherby [59] constitutive model fit to the uniaxial converted shear data for AA7075-T6, AA7xxx-T6, and AA6013-T6 sheet alloys along rolling direction at 0.001 s^{-1} strain rate.

4.2.1.2 RATE-SENSITIVE HOCKETT-SHERBY MODEL

A strain rate dependent term was coupled with the Hocket-Sherby hardening model. An exponential type strain rate term with a strain rate parameter A, as shown in Eq. (4.2), was fit to the experimental data.

Eq. (4.3) shows the Hockett-Sherby hardening function coupled with an exponential type strain rate term and is referred to as the extended Hockett-Sherby (EHS) model.

$$x(\dot{\varepsilon}) = (1 + \dot{\varepsilon})^A$$

Eq. (4.2)

$$\sigma_{EHS}(\varepsilon_p, \dot{\varepsilon}) = \sigma_{HS}(\varepsilon_p) \cdot x(\dot{\varepsilon})$$

Eq. (4.3)

As shown in Figure 27, good agreement was observed between the uniaxial tensile test data and the extended Hockett-Sherby (EHS) hardening model fit for all three sheet alloys at the intermediate (10 and 100 s^{-1}) and high (1,000 s^{-1}) strain rates. The measured and predicted true stress data at an effective plastic strain level of 6%, as shown in Figure 28, demonstrates a good agreement for the range of strain rate. The calibration parameters of the EHS model are shown in Table 5 for all three sheet alloys.
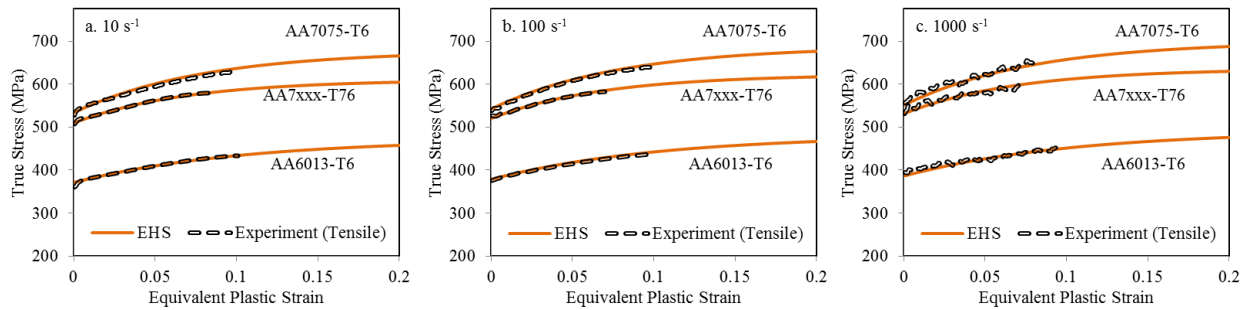
Figure 27: Comparison between the flow stress curve obtained through uniaxial tensile tests and predictions using extended Hockett-Sherby function.
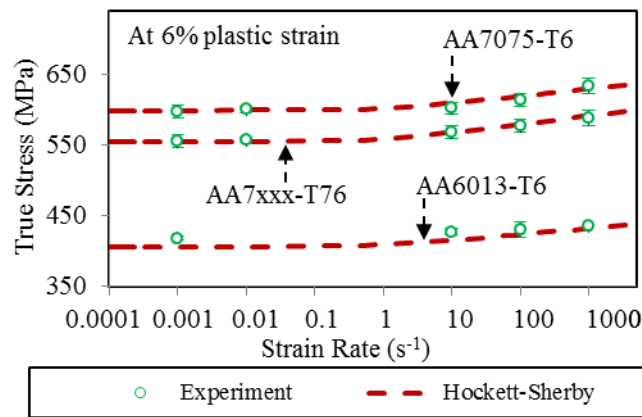
Figure 28: Comparison between measured tensile strength at 6% plastic strain (points) and predictions using extended Hockett-Sherby function (lines).

48

Table 5: Constitutive model parameters of the extended Hockett–Sherby (EHS) for AA6013-T6, AA7075-T6, and developmental AA7xxx-T76 sheet alloys. Reference strain rate is taken as 1 s^{-1}.

Materials	Hocket-Sherby hardening parameters				Strain rate parameter	R^2
	σ_Y (MPa)	σ_S (MPa)	N	P	d	
AA7075-T6	524	666	4.2	3.01	0.007	0.98
AA7xxx-T76	499	597	14.5	1.00	0.009	0.99
AA6013-T6	363	462	13.0	0.74	0.009	0.99

4.2.1.3 TEMPERATURE- AND RATE-SENSITIVE HOCKETT-SHERBY MODEL

To account for thermal softening due to adiabatic heating at elevated strain rates the Hockett-Sherby (EHS) model was further extended. A Johnson and Cook (1983) type thermal softening term, as shown in Eq. (4.5), was coupled with the EHS model in a multiplicative form to form the so-called HS-SRT form

$$\sigma_{HS-SRT}(\varepsilon_p, \dot{\varepsilon}, T) = \sigma_{HS}(\varepsilon_p) \cdot x(\dot{\varepsilon}) \cdot y(T) \qquad \text{Eq. (4.4)}$$

$$y(T) = 1 - nT^{*m} \qquad \text{Eq. (4.5)}$$

where, n and m are the material constants, and T^* is a form of homologous temperature,

$$T^* = \frac{T_S - T_R}{T_M - T_R} \qquad \text{Eq. (4.6)}$$

in which T_S is the temperature of the specimen, T_R is the room temperature (taken as 23 ºC), T_M is the melting temperature of the material (taken as 630 ºC for the AA7075-T6 sheet).

In the constitutive model calibration process, the temperature-equivalent plastic strain history obtained at the dynamic strain rate tests, as shown in Figure 24 (left), was used to describe the specimen temperature, T_S, shown in Eq. (4.6). As shown in Figure 29, HS-SRT model was fit to the experimental data with reasonable success for the 500 s^{-1} conditions. Good agreement was observed between the measured and predicted true stress-strain data for equivalent plastic strains up to fracture for the strain rate levels considered in the present study. Further details regarding the constitutive fitting of the HS-SRT model can be found in Appendix D. Table 6 shows the final calibration parameters of the HS-SRT model for the AA7075-T6 sheet alloy.

For comparison purposes, the predictions using the extended Hockett-Sherby model (Eq. (4.3) are also plotted in Figure 29. The EHS model was able to accurately predict the flow response for the 10 s^{-1} strain rate condition almost until fracture. However, for the 500 s^{-1} strain condition the EHS model provides good correlation only up to an equivalent plastic strain of approximately 0.15. For equivalent plastic strain levels larger than 0.15, the EHS model was not able to capture the material response at the strain of 500 s^{-1} since the temperature rise is higher and the EHS model does not capture thermal softening.
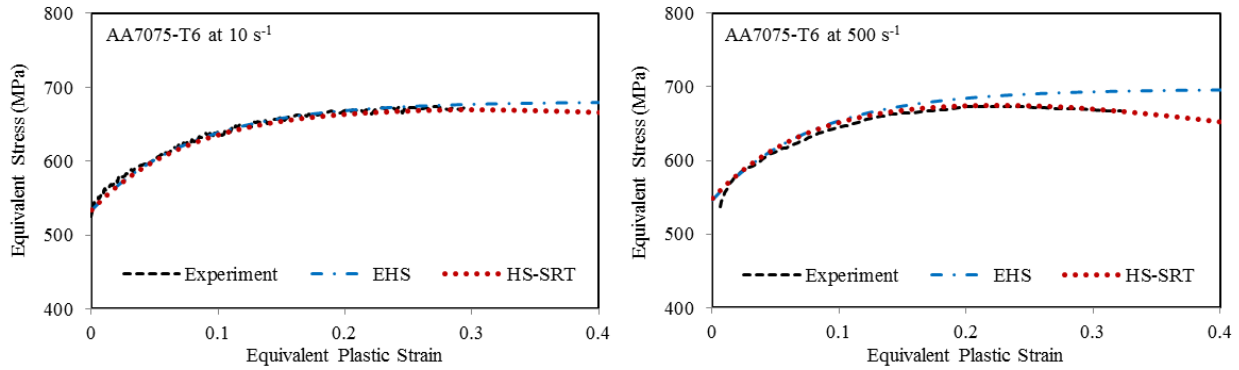
Figure 29: Comparison between the experimental flow stress curves obtained from shear tests for AA7075-T6 sheet alloy and the extended Hockett-Sherby (EHS) and the strain rate and temperature dependent Hockett-Sherby (HS–SRT) model fits at a strain rate of 10 and 500 s^{-1}.

Table 6: The strain rate and temperature dependent Hockett–Sherby (HS-SRT) constitutive model parameters for the AA7075-T6 sheet alloy along the rolling direction.

Materials	Hocket-Sherby hardening parameters				Strain rate parameter	Temperature parameters		R^2
	σ_Y	σ_S	N	P	d	n	M	
AA7075-T6	524	666	4.2	3.01	0.007	2.3	1.6	0.98

4.2.2 YIELD FUNCTION CALIBRATION

The quasi-static constitutive test data in Section 4.1 was also used to calibrate and select an appropriate yield function. A number of yield criteria were considered: the Barlat YLD2000 criterion in its (i) non-associated (NA) (Safaei *et al.*, 2013) and (ii) associated (Barlat *et al.*, 2003) forms along with the (iii) the Barlat YLD2004 (Aretz and Barlat, 2004; Barlat *et al.*, 2005) criterion under an associated flow rule only. Figure 30, Figure 31, and Figure 32 shows the results of the calibrated models in terms of yield loci, *r*–values, and uniaxial stress ratios for the AA6013-T6, AA7075-T6, and AA7xxx-T76 sheet alloys,

respectively. In addition, the equal-biaxial tension to RD yield stress ratio and shear to RD yield stress ratio were also used for the yield surface calibrations to enable a more accurate characterization of the anisotropic yielding response of the materials. Reasonably good agreement was observed between the experimental data and the Barlat YLD2000 yield function prediction in the first quadrant of the yield *loci,* as shown in Figure 30-33. However, the model exhibited lower accuracy in prediction of *r*–values and tensile yield stresses at the orientations of 15°, 30°, 60°, and 75° from the RD, particularly for the 7000-series alloys. Note that only the tensile data in the RD, DD, and TD directions were used to calibrate the associated YLD2000 model. The predicted data from the NA-YLD2000 and Barlat YLD2004 models for all materials were in good agreement with experimental shear, tensile, and equal-biaxial yield stress ratios and *r*–values at every 15° from the RD. Comparing the two models, it appeared that the Barlat YLD2004 has marginally higher accuracy than the NA-YLD2000 model for the majority of the loading conditions. It should be kept in mind that the YLD2000 model contains only eight calibration coefficients, and is readily available within commercial FEA software such as LS-DYNA, which makes it a practical choice for crash simulations. On the other hand, the NA-YLD2000 and YLD2004 models contain 16 and 14 coefficients, respectively, and currently require a user defined material model (UMAT) for FEA implementation. It is worth noting that the Barlat YLD2000 models are applicable only for 2D elements, while the Barlat YLD2004 model can be used only for 3D elements. Further details regarding the yield function calibration process and calibrated model parameters for different yield criteria are provided in Appendix B.
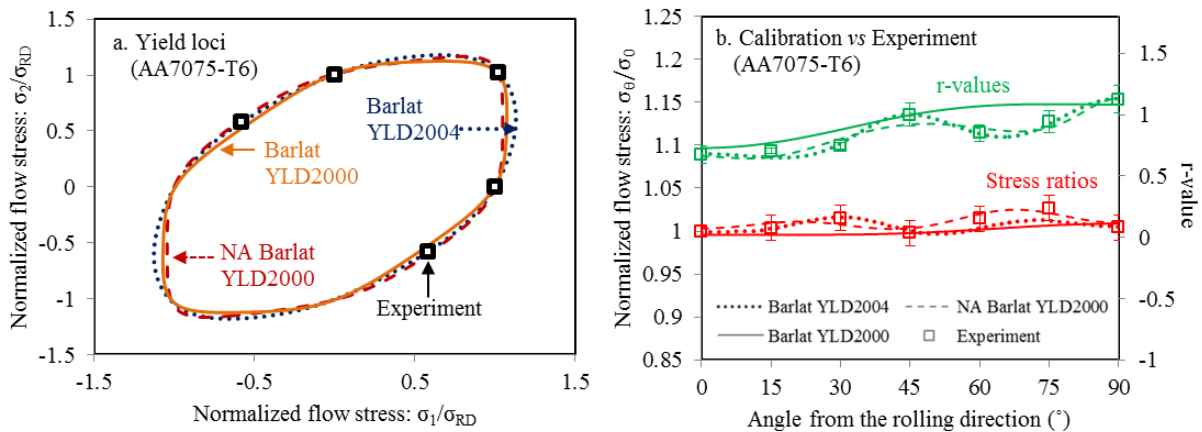
Figure 30: Model predictions compared with the experimental data in terms of (a) yield locus, (b) *r*–values and tensile stress ratios using associated Barlat YLD2000, NA-YLD2000, and Barlat YLD2004 yield functions for AA7075-T6.
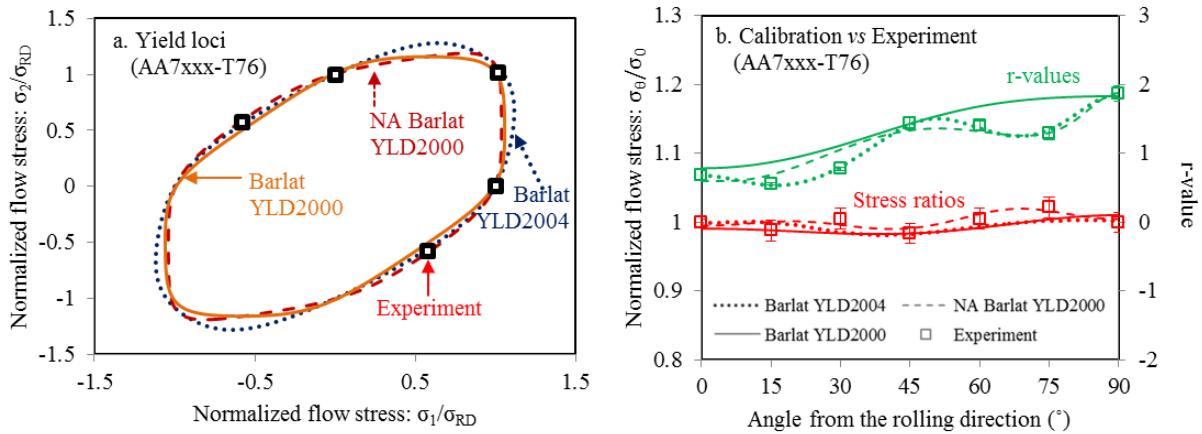
Figure 31: Model predictions compared with the experimental data in terms of (a) yield locus, (b) *r*–values and tensile stress ratios using associated Barlat YLD2000, NA-YLD2000, and Barlat YLD2004 yield functions for AA7xxx-T76.
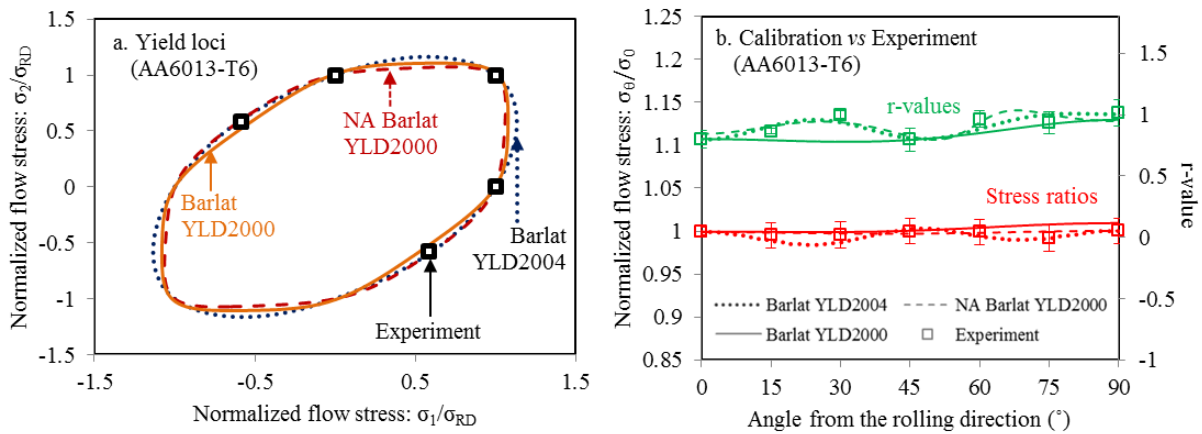
Figure 32: Model predictions compared with the experimental data in terms of (a) yield locus, (b) *r*–values and tensile stress ratios using associated Barlat YLD2000, NA-YLD2000, and Barlat YLD2004 yield functions for AA6013-T6.

4.3   FRACTURE CHARACTERIZATION

As presented in Sections 3.3 and 3.4, the characterization of the fracture response of the aluminum sheet alloys was done under both quasi-static and dynamic conditions for a range of stress states including shear, uniaxial tension, plane strain, and equal-biaxial loading. Quasi-static characterization was done for all three alloys, while the high strain rate fracture characterization work was limited to the AA7075-T6 sheet. A summary of the fracture characterization work is presented in this section, with more detailed narrative presented in Appendices C and D.

4.3.1 QUASI-STATIC FRACTURE TESTS

The experimental results from the quasi-static shear tests are shown in Figure 33. The shear fracture limit strains showed good repeatability for all three sheet alloys. The average maximum in-plane shear strain at fracture was found to be 72%, 31%, and 46% for AA6013-T6, AA7075-T6, and the developmental A7xxx-T76 sheet alloy, respectively. Utilizing Eq. (3.2), the average equivalent strain under shear loading condition was calculated to be 84%, 38% and 54% for the AA6013-T6, AA7075-T6, and A7xxx-T76, respectively. As discussed in Appendix B, the shear-to-tensile stress ratio was found to be 0.59, 0.58, and 0.58 for AA6013-T6, AA7075-T6, and developmental AA7xxx-T76 alloys, respectively, and these values were utilized in calculating the equivalent strain under shear loading. Among the three materials tested herein, the AA6013-T6 sheet has the highest fracture strains indicating the largest ductility, while the AA7075-T6 is found to be the least ductile material. The limit shear strains decrease with material strength, since the AA7075-T6 sheet demonstrated the highest strength compared to developmental AA7xxx-T76 and AA6013-T6 sheet materials, as can be seen in Figure 21.
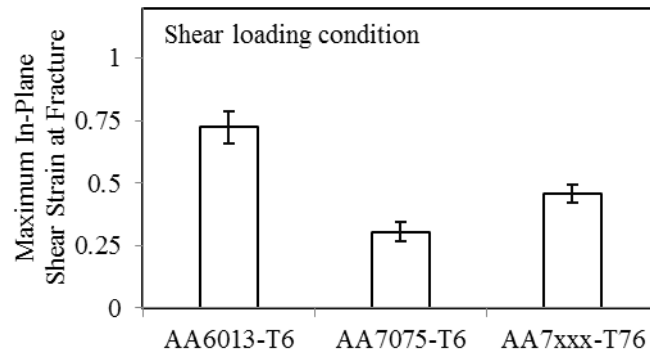
Figure 33: Maximum shear strains at fracture for the three sheet alloys under shear loading condition.

The experimental results from the conical hole expansion tests were used to obtain fracture strains for uniaxial tensile loading. Eq. (3.6) was used to calculate the equivalent fracture strains from the conical hole expansion data. The location of the fracture was found to be approximately consistent for all repeat tests for each specimen. As shown in Figure 34, the hole expansion results were fairly repeatable with the average equivalent fracture strains of 72%, 40%, and 64% for the AA6013-T6, AA7075T6, and developmental AA7xxx-T76 sheet alloys, respectively. As expected, the AA6013-T6 sheet alloy exhibited the largest equivalent strain at fracture, while the AA7075-T6 sheet alloy displayed the lowest ductility under uniaxial tensile loading, similar to the shear loading case.
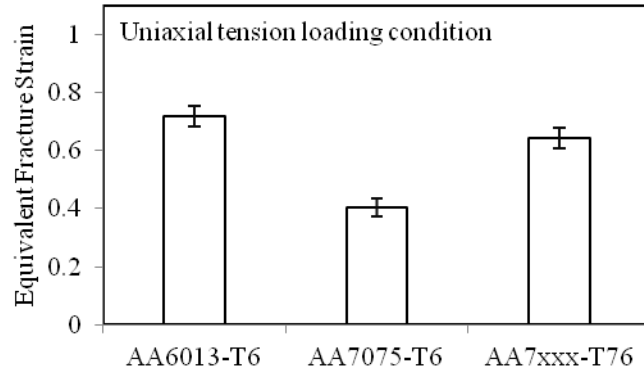
Figure 34: Equivalent Fracture strain of the three sheet alloys under uniaxial tensile loading condition.

V-bend tests were performed to obtain fracture strains under plane strain loading conditions. The comparison between the theoretical and experimental strain paths shown in Figure 35 indicates that the v-bend test induces a plane strain loading condition at the fracture location of the specimen up until fracture, since the minor true strain remains almost zero during the entire test period. The average major true strains at fracture were measured to be 0.43, 0.25, and 0.4 for the AA6013-T6, AA7075-T6, and developmental AA7xxx-T76 sheet alloys, respectively. Using Eq. (3.7), the average equivalent fracture strain for the v-bend tests was found to be 0.47, 0.28, and 0.43 for AA6013-T6, AA7075-T6, and AA7xxx-T76, respectively (also shown in Figure 36). Similar to shear and tensile tests, the strains at fracture were found to be highest for the AA6013-T6 sheet alloys among all three materials tested.
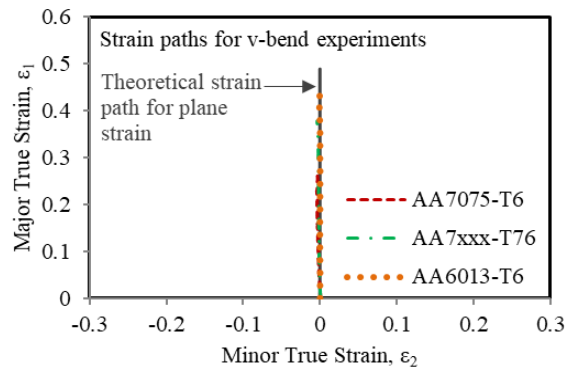
Figure 35: Comparison of strain paths from v-bend tests against the theoretical strain path for plane strain stress state.
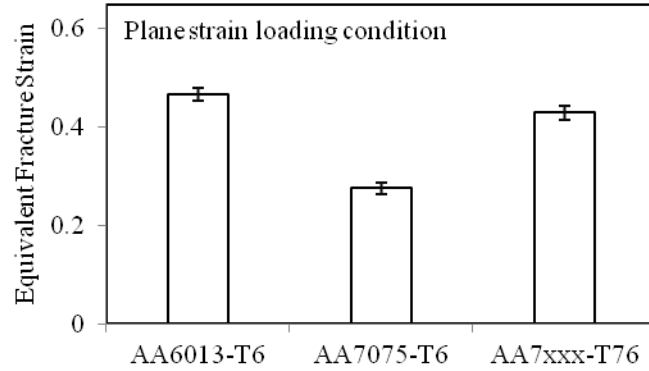
Figure 36: Major true strain at fracture for the three sheet alloys under plane strain loading condition.

Fracture initiation in an equal-biaxial dome test ideally occurs at the dome apex; however, depending on the hardening response of the material, sheet thickness, and friction condition between punch and specimen surface, hemispherical punches can result in strain localization and fracture initiation away from the dome apex. Unlike the results presented by Cheong *et al.* (2019; 2018) for DP980 and AA5182 sheet alloys, the fracture locations identified in the present study were not at the dome apex for the tests performed with 5mm and 10 mm punches. Although the fracture occurred near the dome apex for the 25 mm punch tests, the strain path did not correspond well to the theoretical strain path associated with equal-biaxial stretch, that is, $\varepsilon_1 = \varepsilon_2$, as seen in Figure 37. The deviation of strain path away from the theoretical strain path for equal-biaxial stretching can be attributed to the nature of the strain localization that occurred in the specimen using different sizes of punches.

Figure 38 shows the major and minor true strains extracted at dome apex and fracture location at the moment of fracture using different punch sizes. The equal-biaxial fracture strains selected in this work for inclusion in the fracture are indicated in Figure 38 using the red highlight around the bars for the selected punch size. The fracture strains were obtained from the fracture location of the 10 mm punch dome tests for the AA7xxx-T76 and AA6013-T6 sheet, since these tests resulted in strain paths closest to the theoretical biaxial strain path and the fracture location was very close to the dome apex. On the other hand, for the AA7075-T6 sheet, the 5 mm punch dome tests provided a strain path closest to the theoretical strain path with a fracture location near to the dome apex. The difference in the fracture response of the AA7075-T6 sheet, as compared to the AA6013-T6, and developmental AA7xxx-T76 alloys, in terms of the punch size for the dome tests, can be attributed to the constitutive response of the AA7075-T6 material which exhibited a higher hardening rate compared to the AA6013-T6 and AA7xxx-T76 alloys, as reported in Section 4.1. The equivalent strains at fracture for the equal-biaxial tests were calculated using Eq. (3.7) and found to be 0.44, 0.73, and 0.9 for the AA7075-T6, AA7xxx-T76, and AA6013-T6 sheet alloys, respectively.
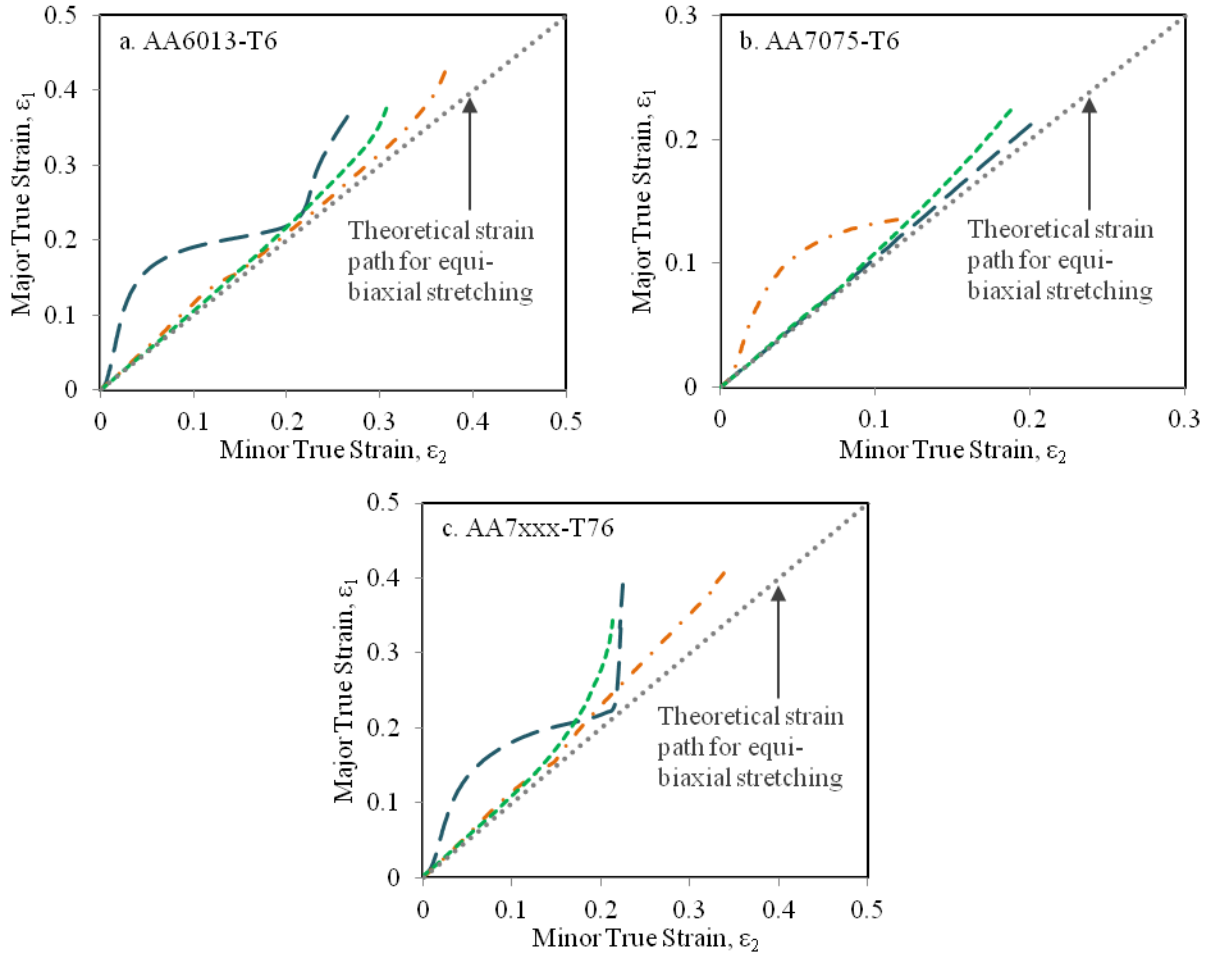
Figure 37: Comparison of strain paths obtained at the fracture location for the (a) AA6013-T6, (b) AA7075-T6, and (c) AA7xxx-T76 sheet alloys using different punch sizes.
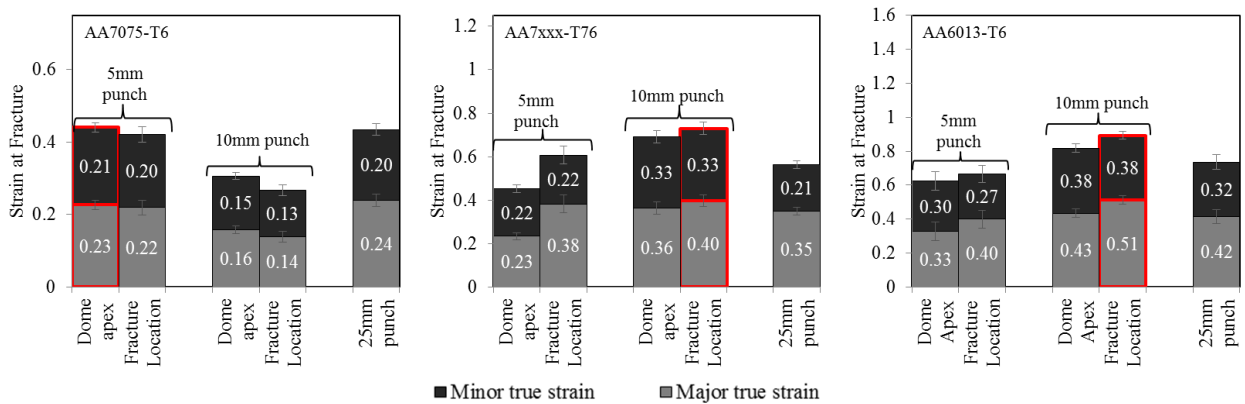
Figure 38: Comparison of average major and minor true strains extracted at the fracture initiation using different sizes of punches for the AA7075-T6, developmental AA7xxx-T76, and AA6013-T6 sheet alloys. Strains marked with a red border were selected for the material fracture characterization.

4.3.2 HIGH STRAIN RATE FRACTURE TESTS

Tests were conducted on the AA7075-T6 to better understand the effect of strain rate on the fracture response in stress states from simple shear to biaxial tension. Figure 39 compares the theoretical and measured strain paths for the shear tests at different strain rates, confirming that a simple shear state was maintained throughout the deformation until fracture. As shown in Figure 40, the equivalent strains at the onset of fracture were obtained with a reasonable level of variation for the shear tests performed at strain rates ranging from 0.01 to 500 s^{-1}. The average equivalent fracture strain obtained from the shear tests decreased from approximately 0.38 to 0.34 (4% decrease) as the strain rate increased from 0.01 to 10 s^{-1}, while the fracture strain increased by approximately 3% to 0.37 between strain rates of 10 and 500 s^{-1}.
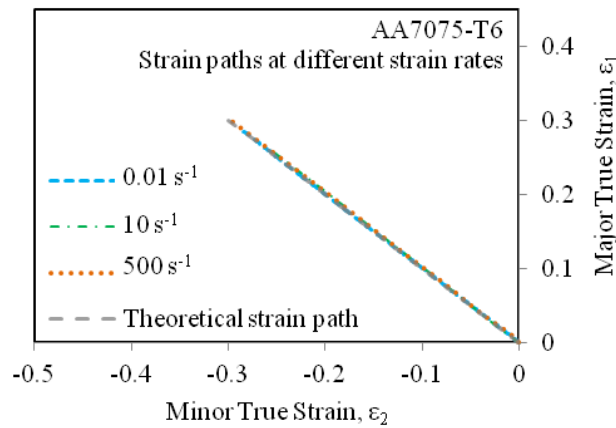
Figure 39: Average experimental shear strain paths for AA7075-T6 at various strain rates, compared with the theoretical strain path to confirm a simple shear loading condition. Note that all of the curves are coincident.
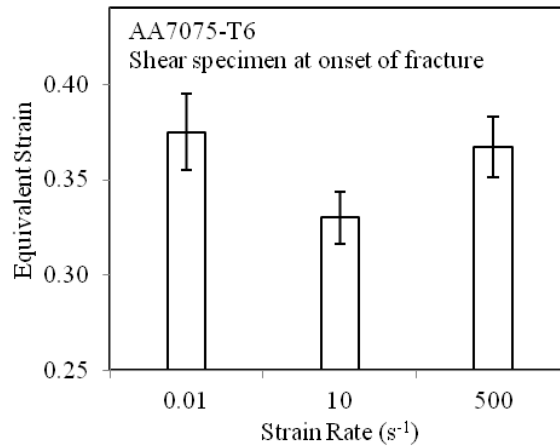
Figure 40: Effect of strain rate on fracture strain during shear tests for AA7075-T6 sheet.

57

As shown in Figure 41a, the hole tension (HT) specimen has a strong concentration of strain at the hole edge. The measured major and minor strains were used to calculate the equivalent strains using a work conjugate approach with the Barlat YLD2004 anisotropic yield function. The equivalent fracture strains for the hole tension tests in Figure 42a, were 0.32, 0.26, and 0.3 at strain rates of 0.01, 10, and 500 s^{-1}, respectively. Due to through thickness thinning near the hole edge the strains at the specimen mid-plane would be higher than the strains measured on the surface. Strain localization was also observed across the minimum section of the notch and grooved tension specimens, as shown in Figure 41b and Figure 41c, respectively. Figure 42b and Figure 42c show the equivalent strains at fracture as a function of strain rate for the notch and groove tension specimens, respectively. The effect of strain rate on the measured surface strains was found to be minimal for both of these specimens. For the notch tension tests, the average equivalent strain of approximately 0.21 was measured on the surface of the samples. Similarly, average equivalent strain of approximately 0.18 was measured on the surface of the groove tension specimens. Unlike the shear specimen, the hole tension, notch tension, and groove tension specimens experience a localized thickness reduction before fracture. The strains extracted on the surface of these specimens at the onset of the fracture using the DIC method will be lower than the strains attained at the specimen mid-plane. In addition, there will also be an increase in triaxiality at the specimen mid-plane as a consequence of localization. The determination of fracture strain and strain path at the mid-plane of the hole tension, notch tension, groove tension specimens therefore requires a hybrid experimental–numerical FE analysis utilizing an appropriate fracture model, as presented in Section 4.4 and Appendix D.
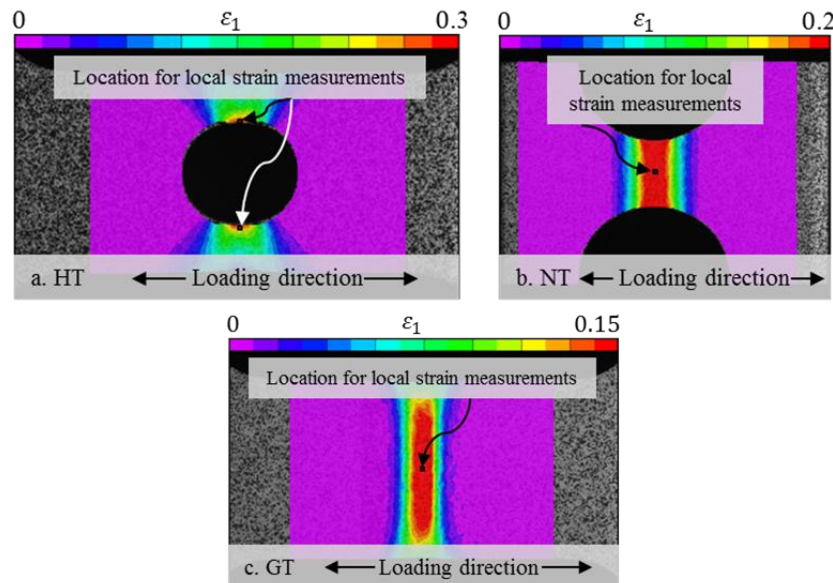
Figure 41: DIC contour plots of major principal strains corresponding to representative (a) hole tension (HT), (b) notch tension (NT), and (c) groove tension (GT) specimens prior to fracture for the AA7075-T6 sheet alloy at a strain rate of 10 s^{-1}.
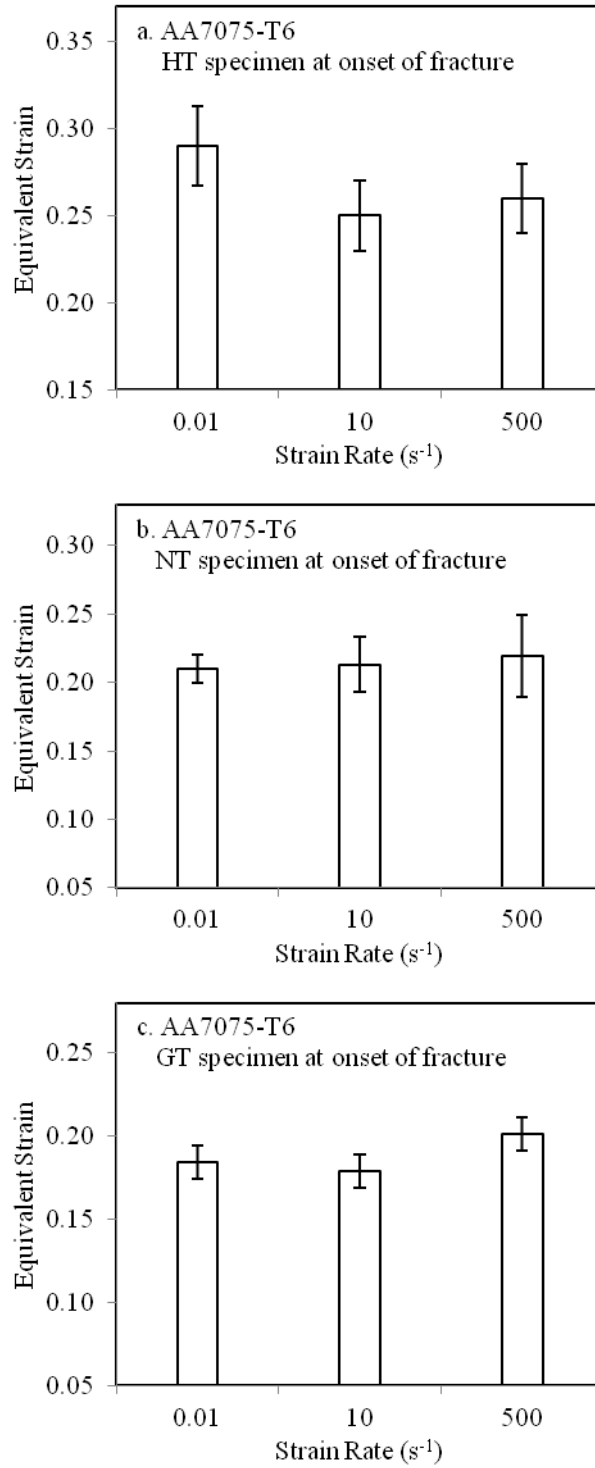
Figure 42: Surface equivalent strain of AA7075-T6 sheet alloy at the onset of fracture as a function of strain rate for the (a) hole tension, (b) notch tension, and (c) groove tension specimens.

4.4   FRACTURE MODEL DEVELOPMENT

The dependency of fracture strains on the stress triaxiality and Lode parameter, seen in the previous section, mandates the need for the development of an accurate fracture model. The experimental quasi-static fracture strain data were used to develop a quasi-static fracture model for the AA7075-T6, AA7xxx-T76, and AA6013-T6. A strain rate dependent fracture model was developed for the AA7075-T6. A summary of the fracture model development and resulting accuracy of the models is presented in this section, while more detailed explanations can be found in Appendices C and D.

4.4.1   QUASI-STATIC FRACTURE MODEL DEVELOPMENT

The quasi-static fracture experimental data from Section 4.3.1 was utilized for the calibration of fracture *loci* with an inherent plane stress assumption. As part of this research, a model incorporating an explicit stronger dependence of the intermediate principal stress using a Drucker-Prager fracture criterion was developed to better capture the fracture behavior in biaxial loading. Instead of selecting the Mohr-Coulomb yield criterion, the Drucker-Prager (1952) yield function was adopted is

$$\bar{\sigma}_{VM} + c(\sigma_1 + \sigma_2 + \sigma_3) = \beta \qquad \text{Eq. (4.7)}$$

in which c and β are material constants. To improve the flexibility of the DP model, the von Mises yield stress $(\bar{\sigma}_{VM})$ is replaced by the non-quadratic Hosford equivalent stress $(\bar{\sigma}_{Hosford})$, as shown in Eq. (2.8), in a manner similar to how the HC model was derived from the Mohr-Coulomb criterion such that

$$\bar{\sigma}_{Hosford} + c(\sigma_1 + \sigma_2 + \sigma_3) = \beta \qquad \text{Eq. (4.8)}$$

To allow for the difference between the uniaxial and equal-biaxial fracture states, the weighting of the intermediate principal stress must be different. This can be accomplished by scaling σ_2 by a constant, b, instead of c, to form a four-parameter *generalized Drucker-Prager* (GDP) fracture criterion

$$\bar{\sigma}_{Hosford} + c(\sigma_1 + \sigma_3) + b\sigma_2 = \beta \quad \text{or} \quad \bar{\sigma}_f[\eta, \bar{\theta}] = \frac{\beta}{g_{GDP}[\sigma/\bar{\sigma}_{VM}]} \qquad \text{Eq. (4.9)}$$

in which, $g_{GDP}[\sigma/\bar{\sigma}_{VM}]$, can be expressed as:

$$g_{GDP}[\sigma/\bar{\sigma}_{VM}] = \left\{ \frac{1}{2} (|f_1 - f_2|^a + |f_2 - f_3|^a + |f_1 - f_3|^a) \right\}^{\frac{1}{a}} + c(2\eta + f_1 + f_3) \\ + b(\eta + f_2) \qquad \text{Eq. (4.10)}$$

where f_1-f_3 are defined in Eq. (2.22).

The fracture locus can be explicitly coupled to the anisotropic yield function and hardening model by performing its calibration in stress space using the magnitudes of the fracture stresses. However, an alternative is to adopt an equivalent strain form of the fracture locus and use the integrated anisotropic equivalent strain in its calibration. To obtain an equivalent strain-based form of the HC and GDP models, the same functional form of the stress-based representation is adopted as

$$\varepsilon_{f,HC} = \frac{\beta'}{g_{HC}[\sigma/\bar{\sigma}_{VM}]} \qquad \text{and} \qquad \varepsilon_{f,GDP} = \frac{\beta'}{g_{GDP}[\sigma/\bar{\sigma}_{VM}]} \qquad \text{Eq. (4.11)}$$

The equivalent fracture strain data from the shear, hole expansion, v-bend, and equal-biaxial dome tests (presented in Section 4.3.1) were utilized for the calibration of the HC and GDP fracture model coupled with the Hockett-Sherby hardening law. The values of the parameters corresponding to the Hockett-Sherby model were already known from the constitutive model fitting work, as shown in Table 5. The agreement between the experimental data and the HC and GDP model fits is shown in Figure 43. The predictions of the GDP model were similar to those of the HC model, except that the strain to fracture under equi-biaxial loading was higher for uniaxial tension using the GDP model, in closer accord with the measured data. The calibrated model parameters to accurately capture the fracture strains of the materials using the GDP model are shown in Table 7. It is noted that the Hosford-Coulomb (HC) model parameters are same as the GDP model parameters except that $b = 0$ for the HC model. Overall, the fracture *loci* generated for the materials studied in this work exhibited a good correlation between material strength and fracture strains, with the AA7075-T6 possessing the lowest ductility, while the AA6013-T6 sheet alloy was the most ductile. It is important to note that, although four experimental data points were used to calibrate four parameters of the GDP fracture model, an additional experiment independent of the model fitting (as shown in 4.4.1.1) has been performed to offer confidence in the fracture model calibrations.
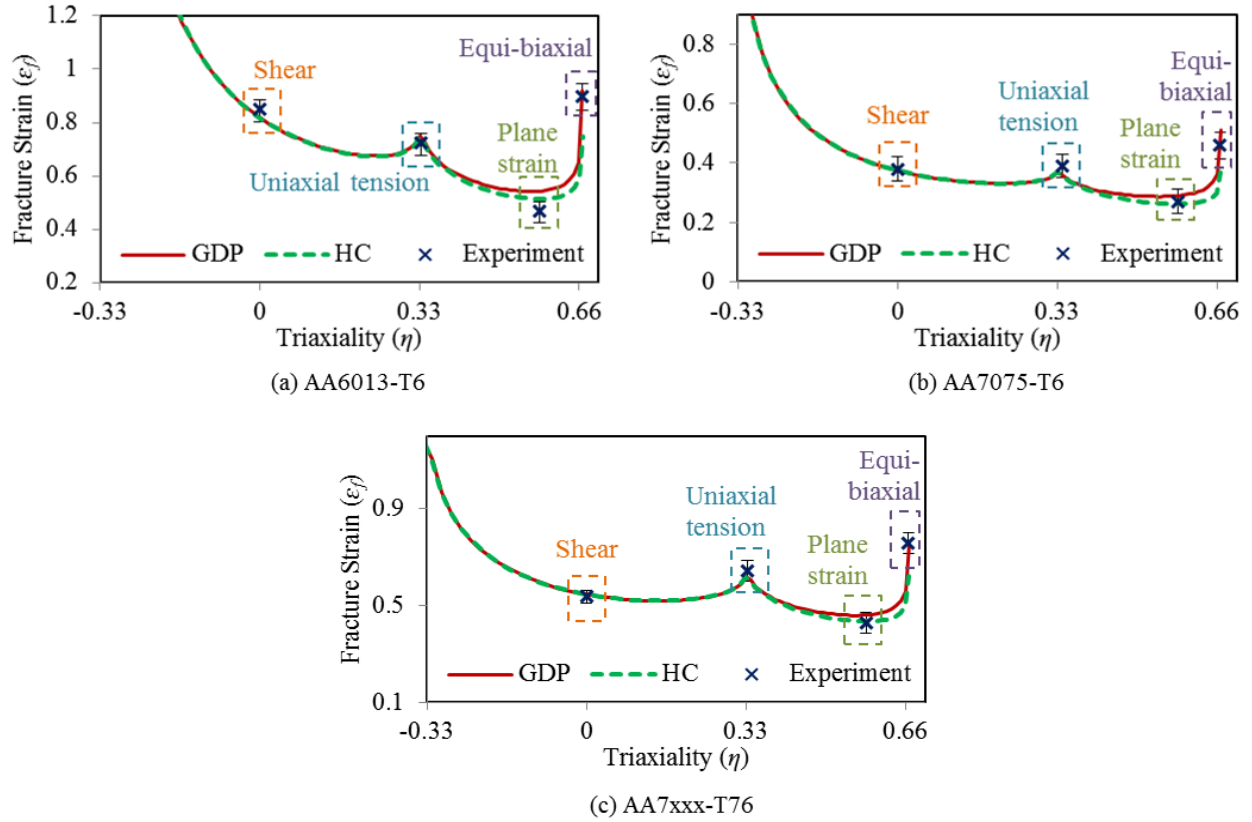
Figure 43: Comparison of fracture *loci* calibrated using the HC and GDP fracture models with the experimental data for the (a) AA6013-T6, (b) AA7075-T6, (c) developmental AA7xxx-T76 sheet alloys under plane stress condition.

Table 7: The generalized Drucker-Prager (GDP) fracture model parameters for the three sheet alloys. The Hosford-Coulomb (HC) model parameters are same as the GDP model parameters except $b = 0$ for the HC model.

Materials	β'	a	c	b
AA6013-T6	1.60	0.42	0.99	-0.26
AA7075-T6	0.63	0.50	0.63	-0.40
AA7xxx-T76	0.88	0.53	0.36	-0.20

4.4.1.1 EVALUATION OF THE QUASI-STATIC FRACTURE MODEL

The calibrated quasi-static fracture criteria were evaluated by performing numerical simulations on three-point bending model of a structural channel section and comparing the model results with the experimental data reported by Kim (2018). The plasticity models for the simulation work were those developed for these materials utilizing the Hockett-Sherby hardening law and Barlat YLD2000 yield criterion, as presented in section 4.2. In order to generalize the GDP fracture loci for non-proportional

loading, the phenomenological Generalized Incremental Stress State dependent damage Model (GISSMO) (Haufe *et al.*, 2010; Neukamm *et al.*, 2009) was implemented. The GDP fracture locus was input in a point-wise fashion to the GISSMO algorithm within the LS-DYNA (Livermore Software, 2012) finite element software. The structural hat channel shown was fabricated by attaching a formed hat section to a baseplate using 5 kN Spaenaur 310-041 steel break stem rivets with a pitch of 25 mm. The hat section and baseplate of the beam were modeled using 2.5 mm x 2.5 mm fully integrated shell elements with seven integration points through the thickness. The supports and indentor were modeled using shell elements with a size of 5 mm x 5 mm and were assigned a rigid non-deformable material model. A *CONSTRAINED_RIVET constraint was used to model the rivets joining the baseplate and the hat section, which tied the two nodes together without failure (since rivet failure was not observed in the experiments). A penalty function contact definition and coefficient of friction of 0.037 was set between all the contacting surfaces to correspond to the Teflon film placed between the fixtures and test article in the actual experiments. The indentor was prescribed a downward motion of 0.508 mm/s, while no mass scaling was used in the simulation. Further details regarding the numerical model are provided in Appendix C. The predicted and measured three-point bending force-displacement curves are shown in Figure 44 for all three sheet alloys. The predicted peak force from the simulations were found to be within 2% of the experimental peak force for the AA7075-T6 and AA6013-T6 sheet alloys, while less than 1% difference was found between the experimental and numerically predicted peak forces for the AA7xxx-T76 sheet alloy. The load-displacement behavior predicted by the numerical models was close to the experimental data. The difference between the predicted and measured absorbed energy was within 5% for all three alloys, as shown in Figure 44.

The pronounced drop in the measured load occurred at approximately 30.5 mm for the AA7075-T6 sheet was due to fracture initiation. The fracture initiation prediction by the simulation models were at approximately 31.8 mm, indicating a good agreement between the test and model prediction. The extent of fracture observed in the test and predicted in the numerical model are similar for the AA7075-T6 sample, as shown in Figure 45. The test specimen is shown at the end of the test, while the model is shown at the initiation of fracture (at an indentor displacement of 31.8 mm). For the AA7xxx-T76, the simulation predicted the onset of fracture late in the analysis at an indentor displacement of approximately 46 mm, while fracture was not observed during the test. Fracture was not predicted for the AA6013-T6, nor was it observed in the test up to a displacement of 67 mm.
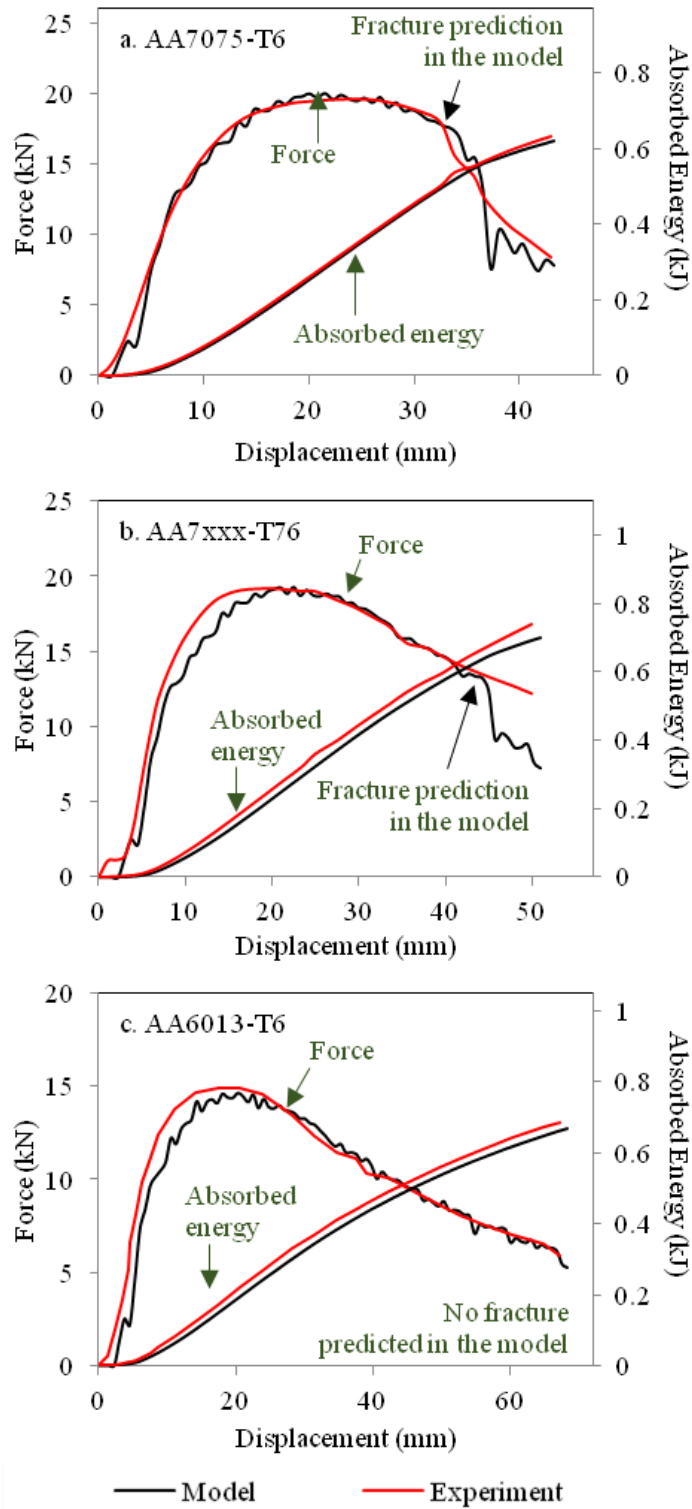
Figure 44: The predicted force-displacement and absorbed energy during quasi-static three-point bend tests compared with the experimental data for the (a) AA7075-T6, (b) AA7xxx-T76, and AA6013-T6 sheet alloy.

Figure 45: Visual comparison of the predicted and observed extent of fracture for the AA7075-T6 sheet alloy.

4.4.2 HIGH RATE FRACTURE MODEL FOR AA7075-T6

The hole tension and notched high rate fracture samples experience local thickness reduction and necking prior to fracture, making it necessary to determine the fracture strains and stress state at the specimen mid-plane through hybrid experimental–numerical FE analysis. For the shear specimens, the equivalent fracture strain data obtained from the high strain rate shear tests, as presented in Section 4.3.2, using the major and minor true stain directly extracted from the DIC data was used for the high strain rate model development.

All of the high strain rate fracture tests were simulated to determine the stress and strain history at the specimen surface and mid-plane using LS-DYNA. A half-symmetry model was used for shear specimen and quarter-symmetry models were developed for the HT, NT, and GT specimens, with appropriate symmetry boundary constraints. The AA7075-T6 sheet was modelled using the HS-SRT hardening model (Eq. (4.4), coupled with the anisotropic YLD2004 yield criterion (Barlat *et al.*, 2005), as calibrated in Section 4.2. These constitutive equations were implemented within a user defined material (UMAT) subroutine implemented within LS-DYNA. The temperature rise due to plastic work was calculated in the simulations based on the adoption of an effective Taylor-Quinney coefficient, which determines the fraction of plastic work converted to heat. As reported by Kapoor and Nemat-Nasser (1998) for the AA6061 at a strain rate of 3,000 s^{-1}, an adiabatic stress-strain curve is accurately traced with 100% of the plastic work converted to heat. However, the Taylor-Quinney coefficient is also commonly found in the literature to be less than unity and values ranging from 30 to 100% have been reported for dynamic conditions (Hodowany et al., 2000; Knysh and Korkolis, 2015; Lu et al., 2018; Smith, 2019; Vazquez-Fernandez et al., 2019; Zhang et al., 2018). In the current work, the Taylor-Quinney coefficient was taken as unity for the strain rate of 500 s^{-1}, while an effective Taylor-Quinney coefficient of 0.3 was adopted for the 10 s^{-1} strain rate conditions. For the quasi-static strain rate experiments, conduction will be significant, leading to a limited temperature rise corresponding to essentially isothermal conditions; thus, the current 0.01 s^{-1} experiments were treated as isothermal (no heat generation). The appropriateness of these values for the Taylor-Quinney coefficient is assessed through comparison of the measured and predicted temperature rise. Further details regarding the FEA model setup are provided in Appendix D.

Initial simulations were run without using a fracture criterion in order to focus on validation of the constitutive model for the range of strain rates and specimen geometries. The predicted force-displacement curves are compared with the experimental data in Figure 46 (the fracture predictions in the figure are discussed below). The black solid dot lines in Figure 46 represent the experimentally measured force-displacement curves from 3-5 repeat tests. As shown in Figure 46(c,f,i,l), the reduction in hardening due to the thermal softening effect is well captured in the simulations at a strain rate of 500 s⁻¹. Good agreement is observed between the model predictions and measured force-displacement curves (up to fracture) for all of the specimen geometries.
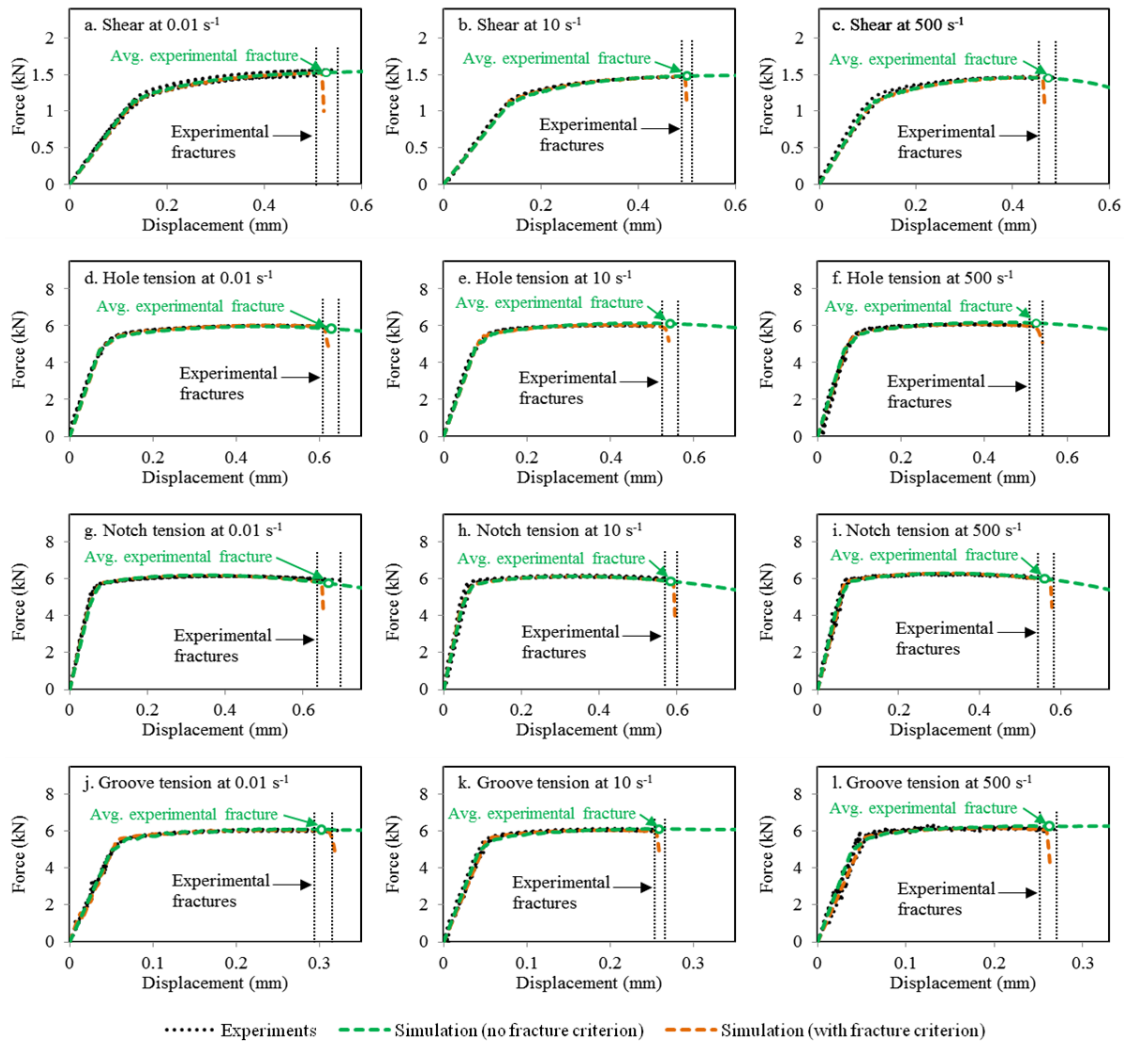
Figure 46: Predicted force-displacement curves of the AA7075-T6 specimens for the complete range of specimens and strain rates compared with the experimental data. The specimen geometry and strain rates are indicated in each figure. The vertical dotted lines indicate the range of fracture strain in the tests. Also shown are FE simulation results utilizing the rate- and temperature-dependent HS-SRT hardening model coupled with the YLD2004 yield criterion.

The measured temperature rise in the 500 s^{-1} HT, NT, and GT tests are shown in Figure 47. The corresponding temperature rise in the shear tests was shown previously in Figure 24. The highest temperature rise of 40°C was observed in the specimens exhibiting larger plastic strains prior to failure, namely the SH and HT specimens. These specimens also display a larger reduction in stress at large strain level under high rate loading (Figure 46), which is attributed to adiabatic heating.
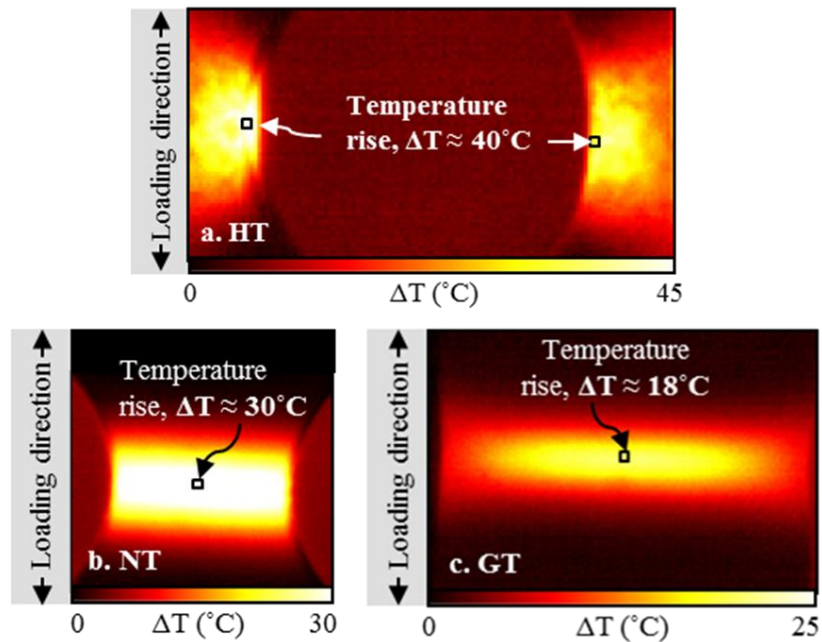
Figure 47: Contour plots of temperature increase due to plastic work in a representative (a) hole tension (HT), (b) notch tension (NT), and (c) groove tension (GT) tests near fracture for the AA7075-T6 sheet alloy at a strain rate of 500 s^{-1}.

The predicted temperature increase for the corresponding samples and loading rates is shown in Figure 48. The temperature rise at the mid-plane of the specimens was found to be approximately 55 °C, 42 °C, and 20 °C for the hole tension, notch tension, and groove tension specimen, respectively. The model prediction of temperature rise for the 10 s^{-1} and 500 s^{-1} specimens were within the variation of the experiment data, as shown in Table 8.
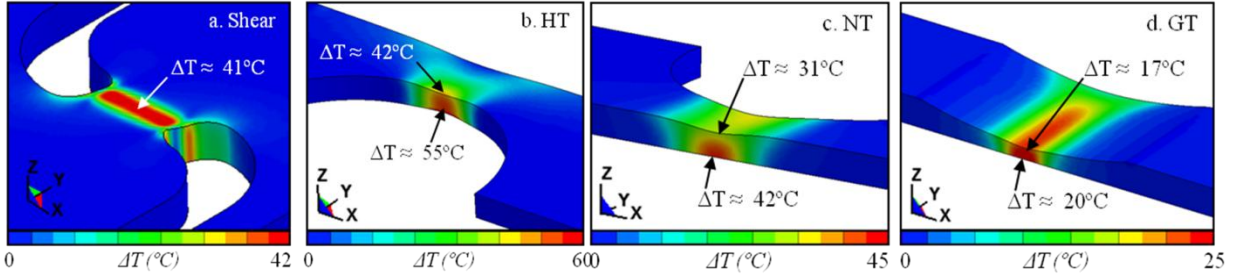
Figure 48: Contour plots of the temperature rise of the AA7075-T6 sheet alloy at the onset of fracture for the (a) shear, (b) hole tension (HT), (c) notch tension (NT), and (d) groove tension (NT) simulations at a strain rate of 500 s^{-1}.

Table 8: Measured heat rise from the tests compared with the corresponding predictions at the specimen surface from the models.

Strain Rate	10 s^{-1}		500 s^{-1}	
	Test	Simulation	Test	Simulation
SH	11±1 ℃	12 ℃	40±2 ℃	41 ℃
HT	21±2 ℃	20 ℃	40±2 ℃	42 ℃
NT	14±1 ℃	15 ℃	30±2 ℃	31 ℃
GT	17±2 ℃	18 ℃	18±3 ℃	17 ℃

To identify the strains at the onset of fracture for the hole tension, notch tension, and groove tension specimens, the strains were extracted from the element with the highest damage accumulation at the measured fracture displacement for that sample. Since the highest amount of strain is accumulated at the mid-plane of the hole tension, notch tension, and groove tension specimens, the element having the highest damage accumulation at the onset of fracture (designated the "critical element") was also found to be at the mid-plane of the specimens. Figure 49 shows the strains extracted from the surface and at the mid-plane of the hole tension, notch tension, and groove tension specimens at a displacement corresponding to the onset of fracture. For all of the specimen geometries, the strains acquired on the surface provided good agreement with the predictions, as shown in Figure 49. For the hole tension specimen, the fracture strain at the mid-plane of the specimen decreased from 0.37 to 0.32 for the increase in strain rate from 0.01 to 10 s^{-1}, while the fracture strain increased to 0.34 as the strain rate increased to 500 s^{-1}. A similar response is observed for the notch tension specimen for which the fracture strain at the mid-plane decreased from 0.36 to 0.31 between the strain rate of 0.01 and 10 s^{-1} and increased by 3% as the strain rate reached to 500 s^{-1}. For the groove tension specimen, an average strain of approximately 0.25 was found at the mid-plane of the specimen for all strain rates. Similar to the strain obtained on the surface of the groove specimen, the effect of strain rate was also found to be minimal for the fracture strains obtained at the mid-plane.
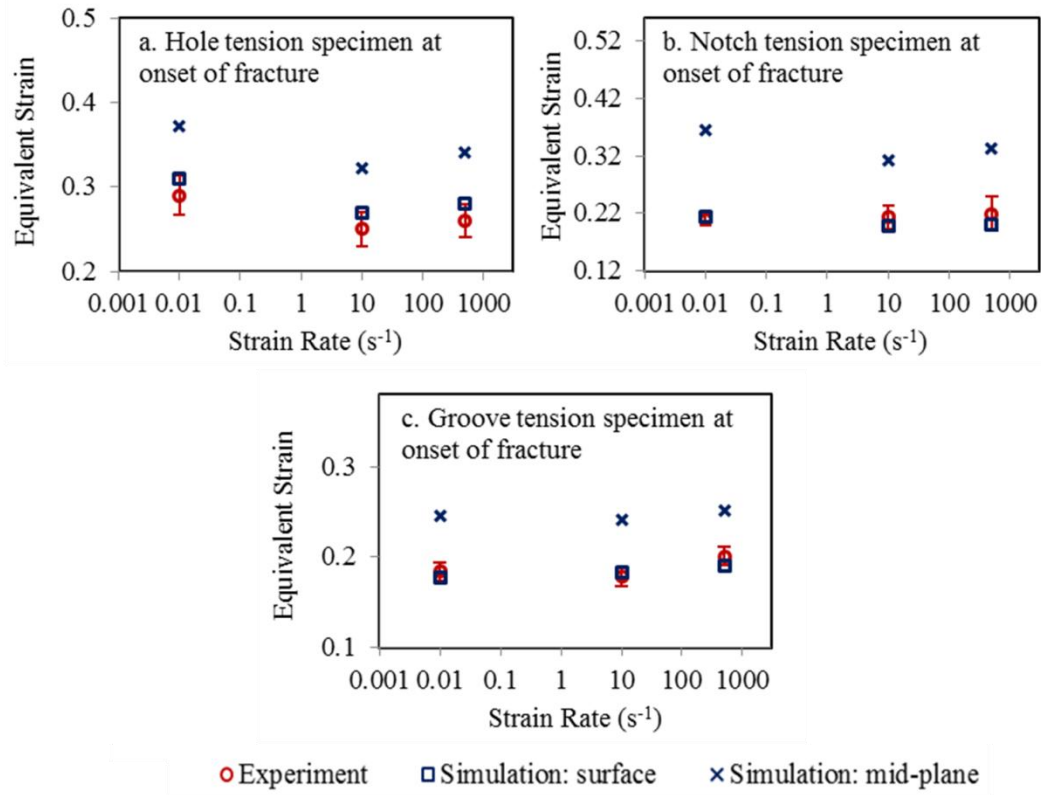
Figure 49: Comparison of the equivalent strain between tests and FE simulations at the onset of fracture as a function of strain rates for the (a) hole tension, (b) notch tension, and (c) groove tension specimen.

Figure 50 shows the evolution of the equivalent plastic strain from the simulation models as a function of the stress triaxiality and the Lode angle parameter for the AA7075-T6 alloy for different specimen geometries at the strain rate of 0.01, 10, and 500 s^{-1}. The effect of strain rate on the loading paths was marginal for all specimen geometries tested. The loading paths to fracture for the shear tests in the gauge region were found to be almost constant, corresponding to the shear stress states (shear: triaxiality $\approx$ 0, Lode angle parameter $\approx$ 0). Although a constant triaxiality of approximately 0.33 and a constant Lode parameter angle of approximately 0.9 is initially found at the mid-plane of the hole tension specimen, due to necking prior to fracture the traixiality and Lode angle parameter reach to 0.38 and 0.8, respectively. For the notch tension samples, the stress triaxiality and the Lode angle parameter increases constantly due to necking from an early stage of the plastic deformation. At the onset of fracture, the triaxiality and Lode angle parameters at the mid-plane of the notch tension specimen are found to be approximately 0.66 and -0.6, respectively. For the groove tension specimen, the stress triaxiality increases from 0.4 to approximately 0.62 at the onset of fracture, while the Lode angle parameter decreases from 0.9 to approximately 0.23 prior to fracture.
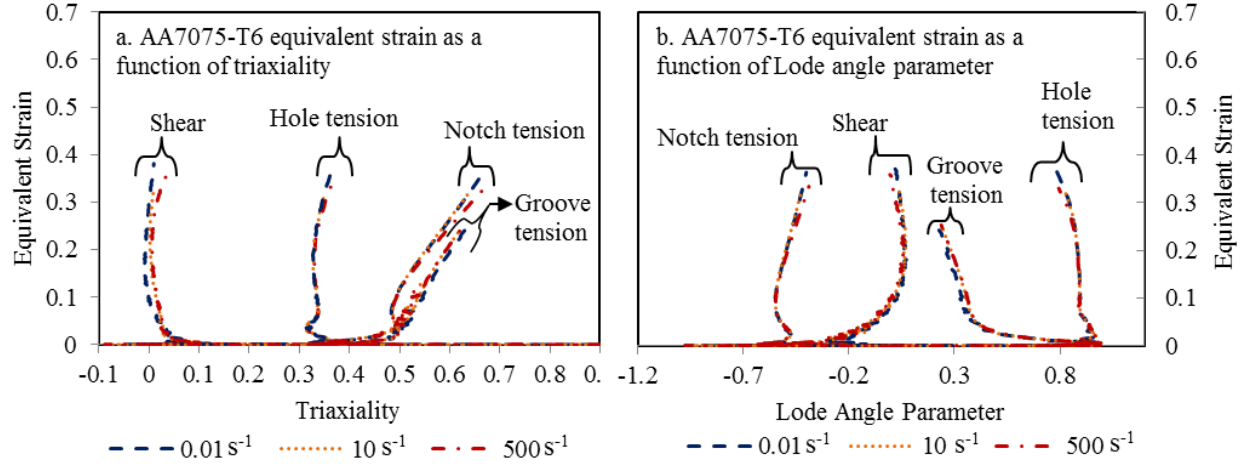
Figure 50: Loading paths to the onset of fracture displaying the equivalent strain as a function of (a) stress triaxiality and (b) lode angle parameter for the strain rate of 0.01, 10, and 500 s^{-1}.

The generalized Drucker-Prager (GDP) fracture model, as shown in Eq. (4.9), alone did not consider strain rate sensitivity; therefore, in order to capture the fracture strains at different strain rates, the material constants β, c, and b are defined in terms of a combined logarithmic and exponential type strain rate term:

$$\beta = \beta_1 \left[\beta_2 \ln \frac{\dot{\varepsilon}}{\dot{\varepsilon}_{ref}} + (1 + \dot{\varepsilon})^{\beta_3} \right] \qquad \text{Eq. (4.12)}$$

$$c = c_1 \left[c_2 \ln \frac{\dot{\varepsilon}}{\dot{\varepsilon}_{ref}} + (1 + \dot{\varepsilon})^{c_3} \right] \qquad \text{Eq. (4.13)}$$

$$b = b_1 \left[b_2 \ln \frac{\dot{\varepsilon}}{\dot{\varepsilon}_{ref}} + (1 + \dot{\varepsilon})^{b_3} \right] \qquad \text{Eq. (4.14)}$$

in which β_{1-3}, c_{1-3}, and b_{1-3} are to be calibrated based on the experimental fracture strain data. $\dot{\varepsilon}_{ref}$ is a reference strain rate, taken as 1 s^{-1} in this work. All 12 fracture tests were included in the calibration of the 10 parameters of the strain rate dependent GDP model. The fracture strains were obtained from the simple shear, hole tension, notch tension, and groove tension simulation models at onset of fracture and provided the fracture strain data close to shear, uniaxial tension, plane strain, and biaxial stress states, respectively. The 3D fracture surfaces for the AA7075-T6 sheet alloy at strain rates of 0.01, 10, and 500 s^{-1} are shown in Figure 51. The model was fit to the fracture strains with the model coefficients shown in Table 9. The

solid black lines in Figure 51 represent the plane stress fracture *loci* generated by the model for the different strain rate conditions. As shown in Figure 51, the strain rate dependent GDP model can be successfully fit to the experimental fracture strains (red data points) with the calibrated model coefficients shown in Table 9.
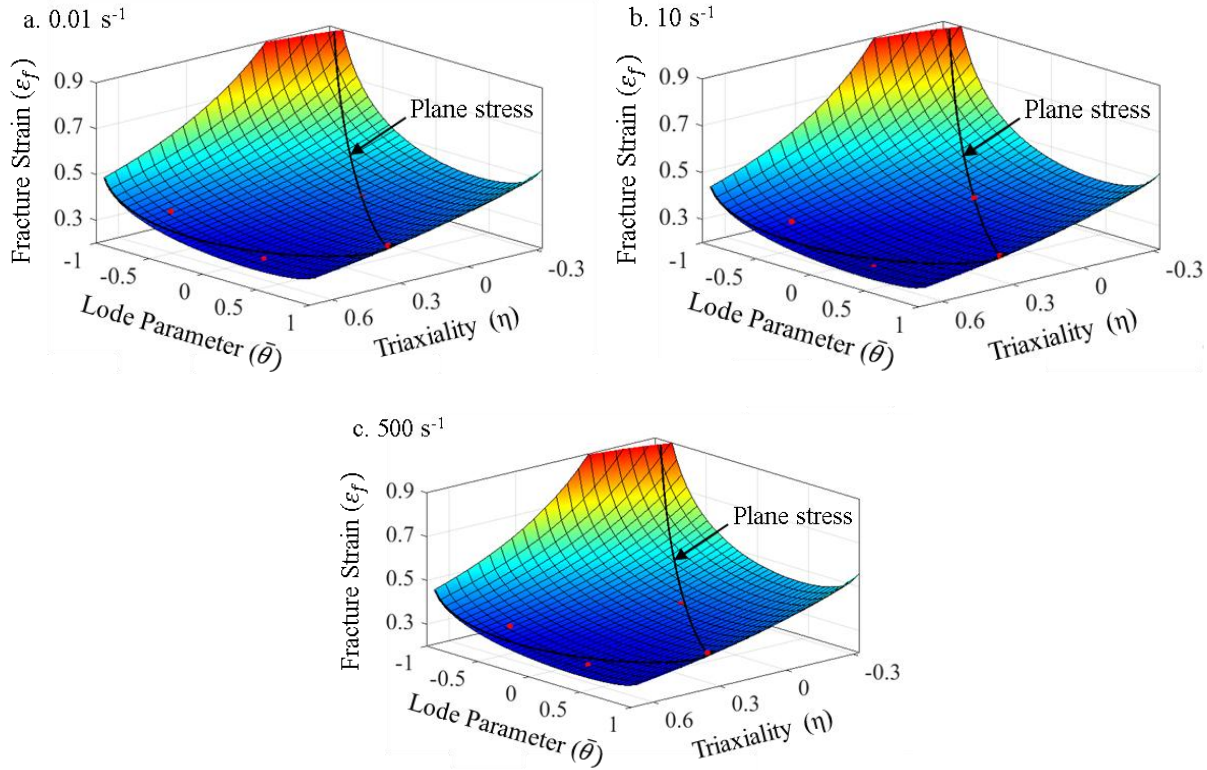
Figure 51: Strain rate dependent generalized Drucker-Prager (GDP) fracture surfaces for the AA7075-T6 sheet alloy at a strain rate of (a) 0.01, (b) 10, and (c) 500 s^{-1}.

Table 9: The strain rate dependent generalized Drucker-Prager (GDP) fracture model parameters for the AA7075-T6 sheet alloy.

	a	β_1	β_2	β_3	c_1	c_2	c_3	b_1	b_2	b_3
AA7075-T6	0.5	0.58	-0.02	0.03	0.79	0.04	-0.08	-0.52	0.05	-0.14

The fracture model fit quality was evaluated by re-running the simulation models utilizing the strain rate GDP model parameters shown in Table 9. To compare the simulation results with the experimental data, the measured force-displacement curves are plotted along with the simulation results in Figure 46 at strain rates ranging from 0.01 to 500 s^{-1}. Good agreement between the predicted and measured force-displacement curves is observed for all of the specimen geometries. The effect of the strain rate on the

hardening response, as well as the stress state dependent constitutive behavior is adequately captured by the numerical simulations. Figure 52 shows the comparison between the measured displacements at fracture for SH, HT, NT, and GT tests with the predictions from the corresponding simulations. The error bars for the experimental data indicate the minimum and maximum measured data points from the population of three to five repeat tests. In general, the displacement at fracture is predicted to be close to the average measured values and falls within the range of variation of the measured results, providing first-level validation of the strain rate dependent GDP model. The reasonable agreement between the experimental data and simulation results is seen as a first-level validation with respect to the model's ability to correctly predict the effect of strain rate on fracture initiation under different stress state conditions. More information regarding the fracture development and finite element analysis results can be found in Appendices C and D.
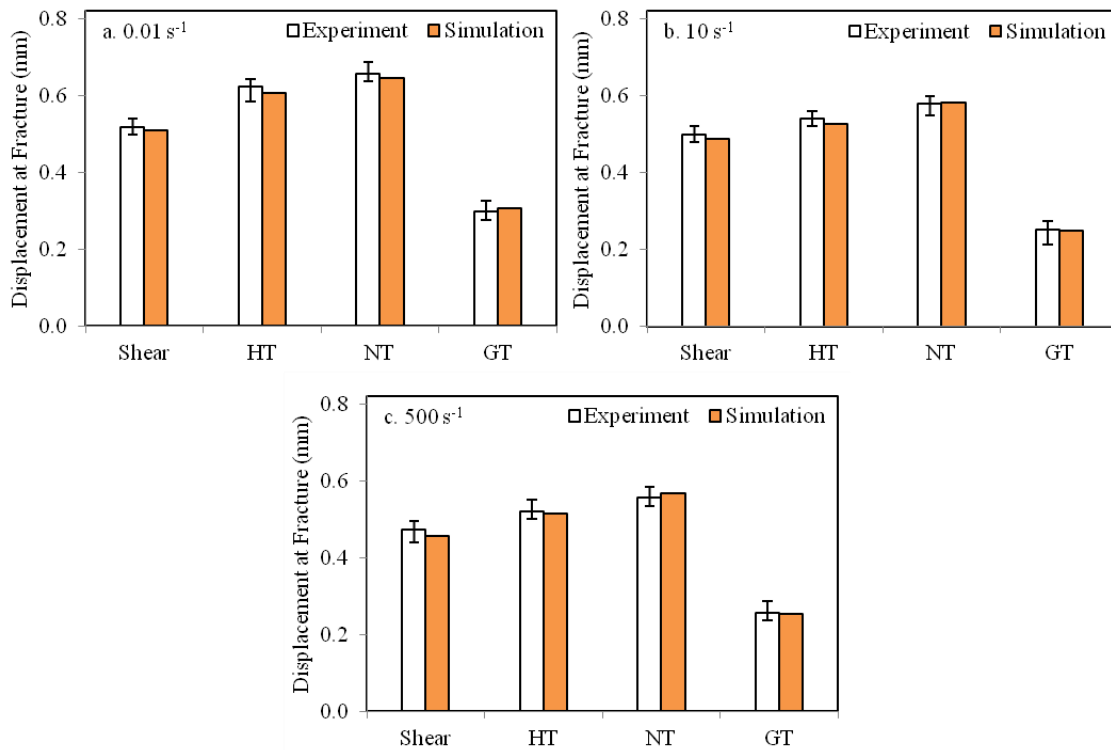
Figure 52: Measured displacements at fracture from different tests compared with the corresponding simulation results for the strain rate of (a) 0.01, (b) 10, and (c) 500 s^{-1}.

CHAPTER 5: SUMMARY AND OUTLOOK

5.1.   SUMMARY OF THE CONTRIBUTION

Within the scope of this thesis, novel techniques and data characterizing the effect of strain rate and stress state on the plasticity and fracture response of 6000- and 7000-series aluminum alloys at room temperature have been presented. The experimental data showed mild positive strain rate sensitivity on the strength of the AA6013-T6, AA7075-T6, and developmental AA7xxx-T6 sheet alloys, based on the uniaxial tensile tests. Notable plastic anisotropy was observed for all three alloys in terms of r–values, indicating the need for incorporating an appropriate yield function calibration. However, none of the materials considered showed definitive trends with respect to the dependency of anisotropy on strain rate. The r–values and flow stress ratios did not exhibit significant strain rate sensitivity, which supported the use of strain rate insensitive yield calibrations for dynamic strain rate applications. The AA7075-T6 sheet alloy displayed the highest strength among the three materials tested, while the AA6013-T6 sheet exhibited the largest ductility for stress states ranging from shear to equal-biaxial. One key outcome of this research was the development of an experimental methodology to obtain the hardening behavior to large strain levels using a shear test that can be adopted for elevated strain rate testing. The shear test performed at elevated strain rates for the AA7075-T6 sheet alloy revealed a reduction in strength at larger strain levels. In addition, the high rate fracture tests showed the strain rate effect on the fracture strains of the AA7075-T6 sheet. Slightly negative rate sensitivity of fracture strain was observed for the AA7075-T6 sheet between strain rates of 0.01 to 10 s^{-1}, whereas mild positive rate sensitivity was observed for strain rates above 10 s^{-1}. The high speed infrared imaging technique employed for the high strain rate tests revealed a substantial increase in temperature within the specimen gauge region for the 500 s^{-1} strain rate tests which are essentially adiabatic. The drop in hardening rate at elevated strain rate conditions was attributed to the increased temperature as the deformation becomes more adiabatic.

A highlight of this work was the development of an appropriate material model capable of accurately predicting the constitutive and fracture response of the materials. For quasi-static strain rate conditions, the Hockett-Sherby hardening law, coupled with the Barlat YLD2000, NA-YLD2000, and Barlat YLD2004 yield functions, were evaluated numerically and provided reasonable accuracy to predict the plasticity response of all three sheet alloys. Furthermore, the generalized Drucker-Prager (GDP) fracture model, developed as a part of this work, provided good predictions of fracture initiation for all three alloys.

A temperature dependent term was coupled with the strain rate sensitive Hockett-Sherby constitutive model, referred to herein as the HS-SRT model, and provided good predictions of the work hardening,

rate sensitivity, and thermal softening for the AA7075-T6 sheet alloy. The empirical HS-SRT constitutive model, coupled with Barlat YLD2004 yield function, captured the work hardening, rate sensitivity, and thermal softening rather well for the AA7075-T6 alloy at elevated strain rate. The strain rate dependent generalized Drucker-Prager (GDP) fracture model captured the equivalent fracture strains reasonably well for the AA7075-T6 sheet alloy under all of the stress state and strain conditions considered in the present work.

The current work demonstrated the importance of a comprehensive experimental program under different stress state and strain rate conditions in developing accurate material models suitable for forming or crash simulations. The developed framework in the present study has strong potential to accurately characterize materials with strong rate sensitivity of fracture.

5.2. CONCLUSIONS

The following conclusions are drawn from this research:

- The AA7075-T6 uniaxial tensile specimens exhibited the highest tensile strength, while the lowest tensile strength was measured for the AA6013-T6 specimens. All three alloys exhibited a mild positive strain sensitivity of flow stress based on the miniature dog-bone uniaxial tensile tests, with a 6% increase in flow stress for an increase in strain rate from 10^{-3} to 10^3 s^{-1}.

- All three alloys showed strong in-plane and transverse plastic anisotropy in terms of the measured r–values, with the highest r–value in the TD (90˚ to rolling) sheet orientation. The lowest r–values were measured in the rolling sheet direction or 15˚ to rolling direction for AA7075-T6 and AA7xxx-T76. The effect of strain rate on anisotropy was shown to be low.

- For quasi-static strain rate conditions, the AA7075-T6 sheet exhibited the lowest ductility, while the AA6013-T6 sheet was found to exhibit the highest ductility for all the stress states considered.

- The shear conversion methodology, developed as part of this research, proved an effective technique for extension of uniaxial tensile data beyond diffuse necking in a tensile test without the need for inverse modelling.

- The temperature rise in the shear specimens due to the plastic deformation was measured to be 40˚C for the 500 s^{-1} tests, compared to 12˚C at 10 s^{-1}. The increase in temperature on the surface of the hole tension, notch tension, and groove tension specimens was measured to be approximately 40˚C, 30˚C, and 18˚C, respectively, at a strain of 500 s^{-1}. This adiabatic temperature rise resulted in a loss in hardening due to thermal softening that was most evident in the high rate shear tests.

- The phenomenological temperature and strain rate-dependent Hockett–Sherby (HS-SRT) constitutive model accurately predicted the hardening response and strain rate sensitivity for sheet alloys considered in this study.

- The developed hardening models coupled with the Barlat YLD2000 and Barlat YLD2004 yield functions provided accurate predictions of load-displacement response for the range of tests considered.

- The elevated strain rate fracture tests on the AA7075-T6 involving the shear, hole tension, notch tension, and groove tension specimens, exhibited mild dependency of fracture strain on the strain rate, and indicated the need for a strain rate dependent fracture model.

- The proposed fracture model, referred to herein as the generalized Drucker-Prager (GDP) criterion distinguishes between the fracture strains under uniaxial *versus* biaxial tension, overcoming a limitation of the Hosford-Coulomb (HC) fracture model, and accurately captures the fracture strains of all three alloys for stress states ranging from shear to equi-biaxial tension.

- The strain rate dependent GDP fracture model, developed in the present study, successfully predicted the onset of fracture in the experiments on AA7075-T6 at strain rates ranging from 0.01 to 500 s^{-1}.

5.3. FUTURE WORK

The following recommendations are offered for future work to enhance the understanding of the behavior of high strength aluminum alloys and support the implementation of proposed constitutive and fracture models:

- The influence of anisotropy on the fracture response of these materials was not evaluated. Fracture characterization tests along different sheet orientations of the materials should be considered.

- The present work considered only proportional loading conditions. Constitutive and fracture characterization, as well as the modeling of the behavior of high strength aluminum alloys under non-proportional conditions should be considered in future work.

- The current study mostly concentrated on plasticity and fracture behavior of the high strength aluminum alloys from a macroscopic aspect. In order to further understand the active fracture mechanisms under different loading conditions and connect the macroscopic responses to the microstructure of the materials, micromechanical investigation of the fracture surface of the specimens utilizing SEM should be performed in future.

- Full scale structural dynamic crash tests and simulation models for the high strength aluminum alloys are left for future work. A comparison between the dynamic crash test data and simulation results will provide further validation of the proposed plasticity and fracture models.

REFERENCES

Abedini, A., Butcher, C., Anderson, D., Worswick, M., Skszek, T., 2015. Fracture Characterization of Automotive Alloys in Shear Loading. SAE Int. J. Mater. Manuf. 8, 774–782. https://doi.org/10.4271/2015-01-0528

Abedini, A., Butcher, C., Nemcko, M.J., Kurukuri, S., Worswick, M.J., 2017. Constitutive characterization of a rare-earth magnesium alloy sheet (ZEK100-O) in shear loading: Studies of anisotropy and rate sensitivity. Int. J. Mech. Sci. 128–129, 54–69. https://doi.org/10.1016/j.ijmecsci.2017.04.013

Anderson, D., Butcher, C., Pathak, N., Worswick, M.J., 2017. Failure parameter identification and validation for a dual-phase 780 steel sheet. Int. J. Solids Struct. 124, 89–107.

Ardell, A.J., 1985. Precipitation hardening. Metall. Trans. A 16, 2131–2165.

Aretz, H., Barlat, F., 2013. New convex yield functions for orthotropic metal plasticity. Int. J. Non. Linear. Mech. 51, 97–111.

Aretz, H., Barlat, F., 2004. General orthotropic yield function based on linear stress deviator transformations. Ghosh S, Castro GC, Lee JK Mater. Process. Des. Model. Simul. Appl. Proc. NUMIFORM 2004 Conf. Columbus, OH 147–151.

Bai, Y., Wierzbicki, T., 2015. A comparative study of three groups of ductile fracture loci in the 3D space. Eng. Fract. Mech. 135, 147–167.

Bai, Y., Wierzbicki, T., 2010. Application of extended Mohr-Coulomb criterion to ductile fracture. Int. J. Fract. 161, 1–20. https://doi.org/10.1007/s10704-009-9422-8

Bai, Y., Wierzbicki, T., 2008. A new model of metal plasticity and fracture with pressure and Lode dependence. Int. J. Plast. 24, 1071–1096. https://doi.org/https://doi.org/10.1016/j.ijplas.2007.09.004

Banabic, D., 2010. Plastic behaviour of sheet metal, Sheet Metal Forming Processes: Constitutive Modelling and Numerical Simulation, Springer-Verlag Berlin Heidelberg. https://doi.org/10.1007/978-3-540-88113-1

Banabic, D., 2000. Anisotropy of Sheet Metal, in: Banabic, D. (Ed.), Formability of Metallic Materials. Springer, Berlin, Heidelberg, pp. 119–172. https://doi.org/https://doi.org/10.1007/978-3-662-04013-3_4

Bao, Y., 2003. Prediction of ductile crack formation in uncracked bodies. Ph.D. thesis. Massachusetts Institute of Technology, USA.

Bardelcik, A., 2012. High Strain Rate Behaviour of Hot Formed Boron Steel with Tailored Properties. Ph.D. thesis. University of Waterloo, Canada.

Bardelcik, A., Salisbury, C.P., Winkler, S., Wells, M.A., Worswick, M.J., 2010. Effect of cooling rate on the high strain rate properties of boron steel. Int. J. Impact Eng. 37, 694–702.

Bardelcik, A., Worswick, M.J., Winkler, S., Wells, M.A., 2012. A strain rate sensitivity constitutive model for quenched steel with tailored properties. Int. J. Impact Eng. 50, 49–62.

Barlat, F., Aretz, H., Yoon, J.W., Karabin, M., Brem, J., Dick, R.E., 2005. Linear transformation-based anisotropic yield functions. Int. J. Plast. 21, 1009–1039.

Barlat, F., Brem, J.C., Yoon, J.W., Chung, K., Dick, R.E., Lege, D.J., Pourboghrat, F., Choi, S.H., Chu, E., 2003. Plane stress yield function for aluminum alloy sheets – part I: theory. Int. J. Plast. 19, 1297–1319. https://doi.org/10.1016/S0749-6419(02)00019-0

Barlat, F., Lege, D.J., Brem, J.C., 1991. A six-component yield function for anisotropic materials. Int. J. Plast. 7, 693–712.

Barlat, F., Lian, J., 1989. Plastic behavior and stretchability of sheet metals. Part I : A yield function for orthotropic sheets under plane stress conditions. Int. J. Plast. 5, 51–66.

Barlat, F., Maeda, Y., Chung, K., Yanagawa, M., Brem, J.C., Hayashida, F.Y., Lege, D.J., Matsui, K., Murtha, S.J., Hattori, S., Becker, R.C., Makosey, S., 1997. Yield function development for aluminum alloy sheets. J. Mech. Phys. Solids 45, 1727–1763.

Barlat, F., Richmond, O., 1987. Crystallographic texture, anisotropic yield surfaces and forming limits of

sheet metals. Mater. Sci. Eng. 91, 55–72.

Beaudoin, A.J., Dawson, P.R., Mathur, K.., Kocks, U.F., Korzekwa, D.A., 1994. Application of polycrystal plasticity to sheet forming. Comput. Methods Appl. Mech. Eng. 117, 49–70.

Becker, R.C., 1993. Simulations of earing in aluminum single crystals and polycrystals. Model. Simul. Mater. Sci. Eng. 1, 203–224.

Bhadauria, S.S., Hora, M.S., Pathak, K.K., 2009. Effect of Stress Triaxiality on Yielding of Anisotropic Materials under Plane Stress Condition. J. Solid Mech. 1, 226–232.

Børvik, T., Clausen, A.H., Eriksson, M., Berstad, T., Hopperstad, O.., Langseth, M., 2005. Experimental and numerical study on the perforation of AA6005-T6 panels. Int. J. Impact Eng. 32, 35–64.

Børvik, T., Hopperstad, O.S., Berstad, T., Langseth, M., 2001. A computational model of viscoplasticity and ductile damage for impact and penetration. Eur. J. Mech. A/Solids 20, 685–712.

Boyce, B.L., Dilmore, M.F., 2009. The dynamic tensile behavior of tough, ultrahigh-strength steels at strain-rates from 0.0002 s−1 to 200 s−1. Int. J. Impact Eng. 36, 263–271. https://doi.org/10.1016/j.ijimpeng.2007.11.006

Brar, N.S., Joshi, V.S., Harris, B.W., 2009. Constitutive model constants for AL7075T651 and Al7075T6. AIP Conf. Proc. 1195 1195, 945.

Butcher, C., Abedini, A., 2017. Shear confusion: Identification of the appropriate equivalent strain in simple shear using the logarithmic strain measure. Int. J. Mech. Sci. 134, 273–283.

Butcher, C., Anderson, D., Worswick, M.J., 2013. Predicting failure during sheared edge stretching using a damagebased model for the shear-affected zone. Int. J. Mater. Manuf. 6, 304–312.

Camacho, G.T., Ortiz, M., 1997. Adaptive lagrangian modelling of ballistic penetration of metallic targets. Comput. Methods Appl. Mech. Eng. 142, 269–301. https://doi.org/https://doi.org/10.1016/S0045-7825(96)01134-6

Campbell, J.D., Ferguson, W.G., 1970. The temperature and strain-rate dependence of the shear strength of mild steel. Philos. Mag. 21, 63–82. https://doi.org/10.1080/14786437008238397

Chakrabarty, D.J., Liu, J., Sawtell, R.R., Venema, G.., 2004. New generation high strength high damage tolerance 7085 thick alloy product with low quench sensitivity. Mater. Forum 28, 969–974.

Chandran, S., Liu, W., Lian, J., Münstermann, S., Verleysen, P., 2021. Strain rate dependent plasticity and fracture of DP1000 steel under proportional and non-proportional loading. Eur. J. Mech. - A/Solids EJMSOL 104. https://doi.org/https://doi.org/10.1016/j.euromechsol.2021.104446

Chen, Y., Clausen, A.H., Hopperstad, O.S., Langseth, M., 2009. Stress-strain behaviour of aluminium alloys at a wide range of strain rates. Int. J. Solids Struct. 46, 3825–3835. https://doi.org/10.1016/j.ijsolstr.2009.07.013

Chen, Z., Butcher, C., 2013. Micromechanics Modelling of Ductile Fracture, Springer Science + Business Media Dordrecht. https://doi.org/10.1007/978-94-007-6098-1

Chen, Z.T., 2004. The role of heterogeneous particle distribution in the prediction of ductile fracture. Ph.D. thesis. University of Waterloo, Canada.

Cheng, L., Xue, X.Y., Tang, B., Liu, D.G., Li, J.Z., Kou, H.C., Li, J.S., 2014. Deformation behavior of hot-rolled IN718 superalloy under plane strain compression at elevated temperature. Mater. Sci. Eng. A 606, 24–30.

Cheong, D.K., 2019. On the influence of the through-thickness strain gradients for characterization of formability and fracture of sheet metal alloys. Master Appl. Sci. thesis. University of Waterloo, Canada.

Cheong, K., Butcher, C., Dykeman, J., 2018. The Influence of the through-thickness strain gradients on the fracture characterization of advanced high strength steels. SAE Int. J. Mater. Manuf. 11. https://doi.org/10.4271/2018-01-0627

Cheong, K., Omer, K., Butcher, C., George, R., Dykeman, J., 2017. Evaluation of the VDA 238-100 tight radius bending test using digital image correlation strain measurement. J. Phys. Conf. Ser. 896, 12075. https://doi.org/10.1088/1742-6596/896/1/012075

Choi, Y., Ha, J., Lee, M.-G., Korkolis, Y.P., 2021. Effect of plastic anisotropy and Portevin-Le Chatelier bands on hole-expansion in AA7075 sheets in-T6 and-W tempers. J. Mater. Process. Technol. 296,

117211.

Clausen, A.H., Børvik, T., Hopperstad, O.S., Benallal, A., 2004. Flow and fracture characteristics of aluminium alloy AA5083-H116 as function of strain rate, temperature and triaxiality. Mater. Sci. Eng. A 364, 260–272. https://doi.org/10.1016/j.msea.2003.08.027

Cockcroft, M.G., Latham, D.J., 1968. Ductility and the workability of metals. J Inst Met. Inst. Met. 96, 33–39. https://doi.org/citeulike-article-id:4789874

Considère, A., 1885. No Title. Ann. des Ponts Chaussées 9, 574–775.

Coulomb, C.A., 1776. Essai sur une application des règles de maximis & minimis à quelques problèmes de statique, relatifs à l'architecture. Mémoire mécanique appliquée, Paris l'Imprimerie R.

Dieter, G.E., Kuhn, A.H., Semiatin, S.L., 2003. Handbook of workability and process design. ASM Int. Mater. Park.

Dong, S., Wang, Y., Xia, Y., 2006. A finite element analysis for using Brazilian disk in split Hopkinson pressure bar to investigate dynamic fracture behavior of brittle polymer materials. Polym. Test. 25, 943–952.

Drucker, D.C., Prager, W., 1952. Soil mechanics and plastic analysis or limit design. Q. Appl. Math. 10, 157–165.

Dunand, M., Mohr, D., 2017. Predicting the rate-dependent loading paths to fracture in advanced high strength steels using an extended mechanical threshold model. Int. J. Impact Eng. 108, 272–285.

Dunand, M., Mohr, D., 2011. On the predictive capabilities of the shear modified Gurson and the modified Mohr-Coulomb fracture models over a wide range of stress triaxialities and Lode angles. J. Mech. Phys. Solids 59, 1374–1394.

Dunand, M., Mohr, D., 2010. Hybrid experimental–numerical analysis of basic ductile fracture experiments for sheet metals. Int. J. Solids Struct. 47, 1130–1143. https://doi.org/10.1016/j.ijsolstr.2009.12.011

El-Magd, E., Abouridouane, M., 2006. Characterization, modelling and simulation of deformation and fracture behaviour of the light-weight wrought alloys under high strain rate loading. Int. J. Impact Eng. 32, 741–758. https://doi.org/10.1016/j.ijimpeng.2005.03.008

Erice, B., Roth, C.C., Mohr, D., 2018. Stress-state and strain-rate dependent ductile fracture of dual and complex phase steel. Mech. Mater. 116, 11–32. https://doi.org/10.1016/j.mechmat.2017.07.020

Everychina.com, 2021. JIMA Aluminum, T4/T6 6262 Aluminum Alloy Sheet , Car Drive System / Enganced Part Aluminium 6262 for sale – Automotive Aluminum Sheet manufacturer from china (108027306) [WWW Document]. URL http://aluminumalloyplate.sell.everychina.com/p-108027306-t4-t6-6262-aluminum-alloy-sheet-car-drive-system-enganced-part-aluminium.html (accessed 12.16.21).

Fang, J., Zhu, Z., Zhang, X., Xie, L., Huang, Z., 2021. Tensile Deformation and Fracture Behavior of AA5052 Aluminum Alloy under Different Strain Rates. J. Mater. Eng. Perform. https://doi.org/https://doi.org/10.1007/s11665-021-06112-5

Follansbee, P.S., Weertman, J., 1982. On the question of flow stress at high strain rates controlled by dislocation viscous flow. Mech. Mater. 1, 345–350.

Fourmeau, M., Børvik, T., Benallal, A., Hopperstad, O.., 2013. Anisotropic failure modes of high-strength aluminum alloy under various stress states. Int. J. Plast. 48, 34–53.

Fourmeau, M., Børvik, T., Benallal, A., Lademo, O.G.G., Hopperstad, O.. S., 2011. On the plastic anisotropy of an aluminum alloy and its influence on the constrained multiaxial flow. Int. J. Plast. 27, 2005–2025. https://doi.org/10.1016/j.ijplas.2011.05.017

Ghahremaninezhad, A., Ravi-Chandar, K., 2013. Crack nucleation from a notch in a ductile material under shear dominant loading. Int. J. Fract. 184, 253–266.

Gosh, A.K., 1977. Tensile instability and necking in materials with strain hardening and strain-rate hardening. Acta Metall. 24, 1413–1424.

Gray III, G.T. (Rusty), 2000. Classic Split-Hopkinson Pressure Bar Testing, in: H. Kuhn, D.M. (Ed.), ASM Handbook-Mechanical Testing and Evaluation. Materials Park, OH.

Gray III, G.T., Chen, S.R., Wright, W., Lopez, M.F., 1994. Constitutive equations for annealed metals

under compression at high strain rates and high temperatures, Los Alamos National Laboratory.

Gruben, G., Fagerholt, E., Hopperstad, O.S., Børvik, T., 2011. Fracture Characteristics of a Cold-Rolled Dual-Phase Steel. Eur. J. Mech. - A/Solids 30, 204–218.

Grytten, F., Holmedal, B., Hopperstad, O.S., Børvik, T., 2008. Evaluation of identification methods for YLD2004-18p. Int. J. Plast. 24, 2248–2277.

Gurson, A., 1977. Continuum theory of ductile rupture by void nucleation and growth: Part I- Yield criteria and flow rules for porous ductile media. J. Eng. Mater. Technol. 99, 2–15.

Gwozdz, M., Kwapisz, K., 2008. Influence of ageing process on the microstructure and mechanical properties of aluminum-silicon cast alloys - Al-9% Si-3% and Al-9% Si- 0.4% Mg. Bachelor degree thesis. Jonkoping University, Sweden.

Ha, J., Baral, M., Korkolis, Y.P., 2019. Ductile fracture of an aluminum sheet under proportional loading. J. Mech. Phys. Solids 132. https://doi.org/https://doi.org/10.1016/j.jmps.2019.103685

Ha, J., Baral, M., Korkolis, Y.P., 2018. Plastic anisotropy and ductile fracture of bake-hardened AA6013 aluminum sheet, International Journal of Solids and Structures. Elsevier Ltd. https://doi.org/10.1016/j.ijsolstr.2018.07.015

Hadianfard, M.J., Smerd, R., Winkler, S., Worswick, M., 2008. Effects of strain rate on mechanical properties and failure mechanism of structural Al-Mg alloys. Mater. Sci. Eng. A 492, 283–292. https://doi.org/10.1016/j.msea.2008.03.037

Hashemi, S., 2006. Foundations of materials science and engineering, McGraw-Hill.

Haufe, A., Neukamm, F., Feucht, M., DuBois, P., Borvall, T., 2010. A comparison of recent damage and failure models for steel materials in crashworthiness application in LS-DYNA, in: 11 International LS-DYNA Users Conference. Detroit, USA.

He, Z., Ma, J., Wang, H., Tan, G.E.B., Shu, D., Zheng, J., 2005. Dynamic fracture behavior of layered alumina ceramics characterized by a split Hopkinson bar. Mater. Lett. 59, 901–904. https://doi.org/10.1016/j.matlet.2004.11.054

Hershey, A.V., 1954. The plasticity of anisotropic aggregate of anisotropic face centered cubic crystals. J. Appl. Mech. Trans. ASME 21, 241–249.

Heuss, R., Müller, N., Sintern, W. van, Starke, A., Tschiesner, A., 2012. Lightweight, heavy impact; How carbon fiber and other lightweight materials will develop across industries and specifically in automotive. Adv. Ind. McKinsey Co.

Higashi, K., Mukai, T., Kaizu, K., Tsuchida, S., Tanimura, S., 1991. STRAIN RATE DEPENDENCE ON MECHANICAL PROPERTIES IN SOME COMMERCIAL ALUMINUM ALLOYS. J. Phys. IV 01, C3-341.

Hill, R., 1948. A theory of the yielding and plastic flow of anisotropic metals. Proc. R. Soc. Lond. A. Math. Phys. Sci. 193, 281–297.

Hockett, J.E., Sherby, O.D., 1975. Large strain deformation of polycrystalline metals at low homologous temperatures. J. Mech. Phys. Solids 23, 87–98. https://doi.org/10.1016/0022-5096(75)90018-6

Hodowany, J., Ravichandran, G., Rosakis, A.J., Rosakis, P., 2000. Partition of plastic work into heat and stored energy in metals. Exp. Mech. 40, 113–123. https://doi.org/http://dx.doi.org/10.1007/BF02325036

Hollomon, J.H., 1945. Tensile deformations. Trans. Metall. Soc. AIME 162, 268–290.

Hosford, W.F., 1992. The plasticity of crystal and polycrystals, Oxford University Press. Oxford, England.

Hosford, W.F., 1972. A generalized isotropic yield criterion. J. Appl. Mech. 39, 604–609.

Hua, X.H., Jain, M., Wilkinson, D.S., Mishra, R.K., 2008. Microstructure-based finite element analysis of strain localization behavior in AA5754 aluminum sheet. Acta Mater. 56, 3187–3201.

Inal, K., Wu, P.D., Neale, K.W., 2002. Large strain behaviour of aluminium sheets subjected to in-plane simple shear. Model. Simul. Mater. Sci. Eng. 10, 237–252.

ISO-12004-2, 2008. Sheet and Strip Determination of Forming Limit Curves – Part 2: Determination of Forming Limit Curves in the Laboratory. Met. Mater.

Jabra, J., Romios, M., Lai, J., Lee, E., Setiawan, M., Lee, E.W., Witters, J., Abourialy, N., Ogren, J.R.,

Clark, R., Oppenheim, T., Frazier, W.E., Es-Said, O.S., 2006. The Effect of Thermal Exposure on the Mechanical Properties of 2099-T6 Die Forgings, 2099-T83 Extrusions, 7075-T7651 Plate, 7085-T7452 Die Forgings, 7085-T7651 Plate, and 2397-T87 Plate Aluminum Alloys. JMEPEG ASM Int. 15, 601–607.

Jang, I., Bae, G., Song, J., Kim, H., Park, N., 2020. Fracture envelopes on the 3D-DIC and hybrid inverse methods considering loading history. Mater. Des. 194, 108934.

Johnson, G.R., Cook, W.H., 1985. Fracture characteristics of three metals subjected to various strains, strain rates, temperatures, and pressures. Eng. Fract. Mech. 21, 31–48.

Johnson, G.R., Cook, W.H., 1983. A constitutive model and data for metals subjected to large strains, high strain rates, and high temperatures. Proceeding 7th Int. Symp. mallistics 541–547.

Jurczak, W., 2012. Dynamic properties of 7000 - series aluminum alloys at large strain rates. Polish Marit. Res. 1 19, 38–43. https://doi.org/10.2478/v10012-012-0005-7.

Kafali, H., Ay, N., 2009. Mechanical Properties of 6013-T6 Aluminium Alloy Friction Stir Welded Plate. Aerosp. Sci. Aviat. Technol. ASAT- 13.

Kapoor, R., Nemat-Nasser, S., 1998. Determination of temperature rise during high strain rate deformation. Mech. Mater. 27, 1–2.

Kaps, L., Lipowsky, J.H., Meywerk, M., Werner, H., Scholz, S.P., 1999. Auswerteverfahren zur Weiterverarbeitung von Versuchsdaten. VDEH Work. Gr. intern Commun.

Kaufman, J.G., 2000. Introduction to Aluminum Alloys and Tempers, ASM International.

Kessler, L., Gerlach, J., 2006. The impact of materials testing strategies on the determination and calibration of different FEM material models. IDDRG 113–120.

Kim, S., 2018. Dynamic and Quasi-Static Response of Warm and Hot Formed Aluminum Beams Under Three-Point Bending by. Master Appl. Sci. thesis, Univ. Waterloo, Waterloo, ON, Canada.

Knysh, P., Korkolis, Y.P., 2015. Determination of the fraction of plastic work converted into heat in metals. Mech. Mater. 86, 71–80. https://doi.org/10.1016/j.mechmat.2015.03.006

Kubík, P., Šebek, F., Hůlka, J., Petruška, J., 2016. Calibration of ductile fracture criteria at negative stress triaxiality. Int. J. Mech. Sci. 108–109, 90–103. https://doi.org/https://doi.org/10.1016/j.ijmecsci.2016.02.001

Kubík, P., Šebek, F., Petruška, J., Hůlka, J., Park, N., Huh, H., 2018. Comparative investigation of ductile fracture with 316L austenitic stainless steel in small punch tests: Experiments and simulations. Theor. Appl. Fract. Mech. 98, 186–198.

Kuwabara, T., Ikeda, S., Kuroda, K., 1998. Measurement and analysis of differential work hardening in cold-rolled steel sheet under biaxial tension. J. Mater. Process. Technol. 80–81, 517–523.

Laughlin, D.E., Miao, W.F., 1998. The effects of Cu and Mn content and processing on precipitation hardening behaviour in Al-Mg-Si-Cu alloy 6022, in: Proceedings of the 1998 TMS Annual Meeting. San Antonio, TX, USA, pp. 63–79.

Lee, B.H., Reddy, N.S., Yeom, J.T., Lee, C.., 2007. Flow softening behavior during high temperature deformation of AZ31Mg alloy. J. Mater. Process. Technol. 187–188, 766–769.

Li, Q.M., Meng, H., 2003. About the dynamic strength enhancement of concrete-like materials in a split Hopkinson pressure bar test. Int. J. Solids Struct. 40, 343–360.

Liang, R., Khan, A.S., 1999. A critical review of experimental results and constitutive models for BCC and FCC metals over a wide range of strain rates and temperatures. Int. J. Plast. 15, 963–980.

Ling, Y., 1996. Uniaxial true stress-strain after necking. AMP J. Technol. 5, 37–48.

Livermore Software, 2012. LS-DYNA keyword user's manual, in: Anonymous : Livermore Software Technology Corporation, California, USA. Livermore Software Technology Corporation, California, USA.

Lode, W., 1926. Versuche über den Einfluss der mittleren Haupspannung auf das Fliessen der Metalle Eisen, Kupfer und Nickel. Zeitschrift für Phys. 36, 913–939.

Lou, Y., Huh, H., 2013. Extension of a shear-controlled ductile fracture model considering the stress triaxiality and the Lode parameter. Int. J. Solids Struct. 50, 447–455.

Lou, Y., Huh, H., Lim, S., Pack, K., 2012. New ductile fracture criterion for prediction of fracture

forming limit diagrams of sheet metals. Int. J. Solids Struct. 49, 3605–3615. https://doi.org/10.1016/j.ijsolstr.2012.02.016

Lou, Y., Yoon, J.W., Huh, H., 2014. Modeling of shear ductile fracture considering a changeable cut-off value for stress triaxiality. Int. J. Plast. 54, 56–80. https://doi.org/https://doi.org/10.1016/j.ijplas.2013.08.006

Lou, Y., Yoon Jeong, W., Huh, H., Chao, Q., Song, J.-H.H., Yoon, J.W., Huh, H., Chao, Q., Song, J.-H.H., 2018. Correlation of the maximum shear stress with micro-mechanisms of ductile fracture for metals with high strength-to-weight ratio. Int. J. Mech. Sci. 146–147, 583–601. https://doi.org/10.1016/j.ijmecsci.2018.03.025

Lu, J., Song, Y., Hua, L., Zheng, K., Dai, D., 2018. Thermal deformation behavior and processing maps of 7075 aluminum alloy sheet based on isothermal uniaxial tensile tests. J. Alloys Compd. 767, 856–869.

Ludwik, P., 1909. Elemente der technologischen Mechanik. Springer Verlag Berlin.

MacDougall, D., 2000. Determination of the Plastic Work Converted to Heat Using Radiometry. Exp. Mech. 40, 298–306.

Mason, J.J., Rosakis, A.J., Ravichandran, G., 1994. On the strain and strain rate dependence of the fraction of plastic work converted to heat: an experimental study using high speed infrared detectors and the Kolsky bar. Mech. Mater. 17, 135–145.

McClintock, F., 1968. A criterion for ductile fracture by the growth of holes. J. Appl. Mech. 35, 363–371.

Mellor, P.B., 1981. Sheet metal forming. ht. Met. Rev 26, 1–20.

Mellor, P.B., Parmar, A., 1978. Plasticity of sheet metal forming. Mech. Sheet Met. Forming, ed. D. P. Koistinen N. M. Wang, Plenum Press. New York 53–74.

Meyers, M.A., 1994. Dynamic behavior of materials. Wiley, New York, USA.

Minkina, W., Dudzik, S., 2009. Infrared thermography - Error and Uncertainties. John Wiley & Sons Ltd., Chichester, West Sussex, U.K. https://doi.org/10.1002/9780470682234

Mises, R. von, 1913. Mechanik der festen Körper im plastisch deformablen Zustand. Nachr. Ges. Wiss. Göttingen. Math.-Phys 1, 582–592.

Mohr, D., Henn, S., 2007. Calibration of Stress-triaxiality Dependent Crack Formation Criteria: A New Hybrid Experimental–Numerical Method. Exp. Mech. 47, 805–820.

Mohr, D., Henn, S., 2004. A New method for calibrating phenomenological crack formation criteria. Tech. Rep. 113, Impact Crashworthiness Lab. Massachusetts Inst. Technol.

Mohr, D., Marcadet, S.J., 2015. Micromechanically-motivated phenomenological Hosford-Coulomb model for predicting ductile fracture initiation at low stress triaxialities. Int. J. Solids Struct. 67–68, 40–55. https://doi.org/10.1016/j.ijsolstr.2015.02.024

Mohr, O., 1914. Abhandlungen aus dem Gebiete der Technischen Mechanik, W. Ernst & Sohn.

Mukhopadhyay, A.K., 2009. Microstructure and properties of high strength aluminum alloys for structural applications. Trans. Indian Inst. Met. 62, 113–122.

Nahshon, K., Xue, Z., 2009. A modified Gurson model and its application to punch-out experiments. Eng. Fract. Mech. 76, 997–1009.

Nakazima, K., Kikuma, T., Hasuka, K., 1968. Study on the Formability of Steel Sheets. Tech. Rep. 264, 8517–8530.

Nembach, E., 1997. Particle Strengthening of Metals and Alloys, John Wiley and Sons, Inc. New York, USA.

Neukamm, F., Feucht, M., Haufe, A., 2009. Considering damage history in crashworthiness simulations, in: 7th European LS-DYNA Conference. Stuttgart, Germany.

Nie, Y., Claus, B., Gao, J., Zhai, X., Kedir, N., Chu, J., Sun, T., Fezzaa, K., Chen, W.W., 2020. In Situ Observation of Adiabatic Shear Band Formation in Aluminum Alloys. Exp. Mech. 60, 153–163. https://doi.org/10.1007/s11340-019-00544-w

Nielson, K.L., Tvergaard, V., 2010. Ductile shear failure or plug failure of spot welds modelled by modified Gurson model. Eng. Fract. Mech. 77, 1031–1047.

Nishi, M., Matsua, K., Miura, N., Watanabe, K., Ikeno, S., Yoshida, T., Murakami, S., 2014. Effect of the

Zn/Mg Ratio on Microstructure and Mechanical Properties in Al-Zn-Mg Alloys. Mater. Sci. Forum 794–796, 479–482.

Noder, J., 2017. Characterization and simulation of warm forming of 6xxx and 7xxx series aluminum alloys. Master Appl. Sci. thesis. University of Waterloo, Canada.

Odeshi, A.G., Al-Ameeri, S., Bassim, M.N., 2005. Effect of high strain rate on plastic deformation of a low alloy steel subjected to ballistic impact. J. Mater. Process. Technol. 162–163, 385–391. https://doi.org/10.1016/j.jmatprotec.2005.02.157

Oh, S.I., Chen, C.C., Kobayashi, S., 1979. Ductile Fracture in Axisymmetric Extrusion and Drawing–Part 2: Workability in Extrusion and Drawing. J. Eng. Ind. 101, 36–44.

Omer, K., Abolhasani, A., Kim, S., Nikdejad, T., Butcher, C., Wells, M., Esmaeili, S., Worswick, M., 2018. Process parameters for hot stamping of AA7075 and D-7xxx to achieve high performance aged products. J. Mater. Process. Technol. 257, 170–179. https://doi.org/10.1016/j.jmatprotec.2018.02.039

Oosterkamp, L.D., Ivankovic, A., Venizelos, G., 1999. High strain rate properties of selected aluminium alloys. Mater. Sci. Eng. A 278, 225–235. https://doi.org/10.1016/S0921-5093(99)00570-5

Papasidero, J., Doquet, V., Mohr, D., 2015. Ductile fracture of aluminum 2024-T351 under proportional and non-proportional multi-axial loading: Bao-Wierzbicki results revisited. Int. J. Solids Struct. 69–70, 459–474.

Pathak, N., 2015. Characterization and Modelling of Sheared Edge Failure in Advanced High Strength Steel. PhD thesi. University of Waterloo, Canada.

Pathak, N., Butcher, C., Worswick, M.J., Bellhouse, E., Gao, J., 2017. Damage evolution in complex-phase and dual-phase steels during edge stretching. Materials (Basel). 10, 1944–1996.

Peirs, J., Verleysen, P., Degrieck, J., 2012. Novel Technique for Static and Dynamic Shear Testing of Ti6Al4V Sheet. Exp. Mech. 52, 729–741. https://doi.org/10.1007/s11340-011-9541-9

Peirs, J., Verleysen, P., Tirry, W., Rabet, L., Schryvers, D., Degrieck, J., 2011a. Dynamic shear localization in Ti6Al4V. Procedia Eng. 10, 2342–2347.

Peirs, J., Verleysen, P., Van Paepegem, W., Degrieck, J., 2011b. Determining the stress-strain behaviour at large strains from high strain rate tensile and shear experiments. Int. J. Impact Eng. 38, 406–415. https://doi.org/10.1016/j.ijimpeng.2011.01.004

Pérez-Castellanos, J.-L., Rusinek, A., 2012. Temperature increase associated with plastic deformation under dynamic compression: application to aluminum alloy Al6082. J. Theor. Appl. Mech. 50, 377–398.

Pinlung, S.B., 2015. 7xxx Aluminum Sheets for Automotive Applications. Masters Appl. Sci. Thesis. University of Windsor, Canada.

Plunkett, B., Lebensohn, R.A., Cazacu, O., Barlat, F., 2006. Anisotropic yield function of hexagonal materials taking into account texture development and anisotropic hardening. Acta Mater. 54, 4159–4169.

Prillhofer, R., Rank, G., Berneder, J., Antrekowitsch, H., Uggowitzer, P.J., Pogatscher, S., 2014. Property criteria for automotive Al-Mg-Si sheet alloys. Mater. J. 7, 5047–5068. https://doi.org/10.3390/ma7075047

Rahmaan, T., Bardelcik, A., Imbert, J., Butcher, C., Worswick, M.J., 2016. Effect of strain rate on flow stress and anisotropy of DP600, TRIP780, and AA5182-O sheet metal alloys. Int. J. Impact Eng. 88, 72–90. https://doi.org/10.1016/j.ijimpeng.2015.09.006

Reyes, A., Hopperstad, O.S., Lademo, O.G., Langseth, M., 2006. Modeling of textured aluminum alloys used in a bumper system: material tests and characterization. Comput. Mater. Sci. 37, 246–268.

Rice, J., Tracey, D., 1969. On the ductile enlargement of voids in triaxial stress fields. J. Mech. Phys. Solids 17, 201–217.

Rittel, D., Zhang, L.H., Osovski, S., 2017. The dependence of the Taylor–Quinney coefficient on the dynamic loading mode. J. Mech. Phys. Solids 107, 96–114.

Roth, C.C., 2015. Experimental and Numerical Investigation of Ductile Fracture Initiation at Low, Intermediate and High Strain Rates. PhD thesis. École Polytechnique, France.

Roth, C.C., Mohr, D., 2016. Ductile fracture experiments with locally proportional loading histories. Int. J. Plast. 79, 328–354. https://doi.org/10.1016/j.ijplas.2015.08.004

Roth, C.C., Mohr, D., 2015. Experimental investigation on shear fracture at high strain rates. EPJ Web Conf. 94, 1078.

Roth, C.C., Mohr, D., 2014. Effect of strain rate on ductile fracture initiation in advanced high strength steel sheets: Experiments and modeling. Int. J. Plast. 56, 19–44. https://doi.org/10.1016/j.ijplas.2014.01.003

Rusinek, A., Klepaczko, J.R., 2009. Experiments on heat generated during plastic deformation and stored energy for TRIP steels. Mater. Des. 30, 35–48.

Safaei, M., Zang, S., Lee, M., Waele, W. De, 2013. Evaluation of anisotropic constitutive models: mixed anisotropic hardening and non-associated flow rule approach. Int. J. Mech. Sci. 73, 53–68. https://doi.org/10.1016/j.ijmecsci.2013.04.003

Sakurai, T., 2008. The latest trends in aluminum alloy sheets for automotive body panels. Mater. Process Res. Sect. Alum. Sheets Coils Dep. Moka Plant, Alum. Copp. Co. KOBELCO TE.

Salisbury, C., Worswick, M.J., Mayer, R., 2006. High rate constitutive modeling of aluminum alloy tube. J. Phys. IV 134, 43–48.

Salisbury, C.P., 2001. Spectral analysis of wave propagation through a polymeric Hopkinson bar. Master Appl. Sci. thesis. University of Waterloo, Canada.

Sasso, M., Forcellese, A., Simoncini, M., Amodio, D., Mancini, E., 2015. High strain rate behaviour of AA7075 aluminum alloy at different initial temper states. Key Eng. Mater. 651–653, 114–119. https://doi.org/10.4028/www.scientific.net/KEM.651-653.114

Scales, M., Tardif, N., Kyriakides, S., 2016. Ductile failure of aluminum alloy tubes under combined torsion and tension. Int. J. Solids Struct. 97–98, 116–128.

Sligtenhorst, C.V., Cronin, D.S., Brodland, G.W., 2006. High strain rate compressive properties of bovine muscle tissue determined using a split Hopkinson bar apparatus. J. Biomech. 39, 1852–1858.

Smerd, R., Winkler, S., Salisbury, C., Worswick, M., Lloyd, D., Finn, M., 2005. High strain rate tensile testing of automotive aluminum alloy sheet. Int. J. Impact Eng. 32, 541–560. https://doi.org/10.1016/j.ijimpeng.2005.04.013

Smerd, R.O., 2005. Constitutive Behavior of Aluminum Alloy Sheet at High Strain Rates. Master Appl. Sci. thesis. University of Waterloo, Canada.

Smith, J.L., 2019. Full-Field Measurement of the Taylor-Quinney Coefficient in Tension Tests of Ti-6Al-4V, Aluminum 2024-T351, and Inconel 718 at Various Strain Rates. The Ohio State University.

Stachowicz, F., 2008. Estimation of hole-flange ability for deep drawing steel sheets. Arch. Civ. Mech. Eng. 8, 167–172. https://doi.org/10.1016/S1644-9665(12)60203-9

Steglich, D., Tian, X., Bohlen, J., Kuwabara, T., 2014. Mechanical testing of thin sheet magnesium alloys in biaxial tension and uniaxial compression. Exp. Mech. 54, 1247–1258. https://doi.org/10.1007/s11340-014-9892-0

Swift, M.W., 1952. Plastic instability under plane stress. J. Mech. Phys. Solids 1, 1–18. https://doi.org/10.1016/0022-5096(52)90002-1

Tajally, M., Emadoddin, E., 2011. Mechanical and anisotropic behaviors of 7075 aluminum alloy sheets. Mater. Des. 32, 1594–1599. https://doi.org/10.1016/j.matdes.2010.09.001

ten Kortenaar, L., 2016. Failure Characterization of Hot Formed Boron Steels with Tailored Mechanical Properties. Master Appl. Sci. thesis. University of Waterloo, Canada.

Thomesen, S., Hopperstad, O.S., Myhr, O.R., Børvik, T., 2020. Influence of stress state on plastic flow and ductile fracture of three 6000-series aluminium alloys. Mater. Sci. Eng. A 783, 139295.

Thompson, A.C., 2006. High Strain Rate Characterization of Advanced High Strength Steels. Master Appl. Sci. thesis. University of Waterloo, Canada.

Tian, H., Baral, M., Korkolis, Y.P., Brownell, B., 2017. Earing in cup-drawing of anisotropic Al-6022-T4 sheets. Int. J. Mater. Form. 10:3, 329–343.

Touloukian, Y.S., DeWitt, D.P., 1970. Thermophysical properties of matter, Thermal radiative properties - Metallic elements and alloys, Vol 7. IFI/Plenum, New York.

Tresca, H., 1864. Mémoire sur l'écoulement des corps solides soumis à de fortes pressions. Comptes Rendus hebdomadaíres des séances l'Académie des Sci. Paris 59, 754–758.

Tvergaard, V., Needleman, A., 1984. Analysis of the cup-cone fracture in a round tensile bar. Acta Metall. 32, 157–169.

US Department of Energy, 2015. Chapter 8: Advancing Clean Transportation and Vehicle Systems and Technologies | Connected and Automated Vehicles Technology Assessment. Quadrenn. Technol. Rev. 11.

Van Liempta, P., Sietsmaa, J., 2016. A physically based yield criterion I. Determination of the yield stress based on analysis of pre-yield dislocation behaviour. Mater. Sci. Eng. A 662, 80–87.

Vazquez-Fernandez, N.I., Soares, G.C., Smith, J.L., Seidt, J.D., Isakov, M., Gilat, A., Kuokkala, V.T., Hokka, M., 2019. Adiabatic Heating of Austenitic Stainless Steels at Different Strain Rates. J. Dyn. Behav. Mater. 5, 221–229. https://doi.org/10.1007/s40870-019-00204-z

VDA 238 100, 2017. Plate bending test for metallic materials.

Vic-3d Software Manual [WWW Document], 2021. . Version 8.4. URL http://www.correlatedsolutions.com/supportcontent/VIC-3D-8-Manual.pdf

Voce, E., 1948. The relationship between stress and strain for homogeneous deformation. J. Inst. Met. 74, 537–562.

Weertman, J., Vreeland Jr, T., Jassby, K.M., 1973. Dislocation mechanics at high strain rates. Metall. Eff. High Strain Rates 319–333.

Winkler, S., Thompson, A., Salisbury, C., Worswick, M., Riemsdijk, I., Mayer, R., 2008. Strain rate and temperature effects on the formability and damage of advanced high-strength steels. Metall. Mater. Trans. A 39, 1350–1358. https://doi.org/10.1007/s11661-008-9495-4

Wolverton, C., 2001. Crystal structure and stability of complex precipitate phases in Al-Cu-Mg-(Si) and Al-Zn-Mg alloys. Acta Mater. 49, 3129–3142.

Wu, X.Z., Xiao, D.H., Zhu, Z.M., Li, X.X., Chen, K., 2014. Effects of Cu/Mg ratio on microstructure and properties of AA7085 alloys. Trans. Nonferrous Met. Soc. China 24, 2054–2060. https://doi.org/10.1016/S1003-6326(14)63311-2

Xiao, G., Yang, Q., Li, L., Zeng, J., 2016. Constitutive analysis of 6013 aluminum alloy in hot plane strain compression process considering deformation heating integrated with heat transfer. Met. Mater. Int. 22, 58–68. https://doi.org/10.1007/s12540-015-5296-7

Yoon, J.W., Barlat, F., Dick, R.E., Karabin, M.E., 2006. Prediction of six or eight ears in a drawn cup based on a new anisotropic yield function. Int. J. Plast. 22, 174–193.

Young, R.F., Bird, J.E., Duncan, J.L., 1981. An automated hydraulic bulge tester. J. Appl. Metalwork. 2, 11–18.

Zerilli, F.J., Armstrong, R.W., 1987. Dislocation-mechanics-based constitutive relations for material dynamics calculations. J. Appl. Phys. 61, 1816–1825. https://doi.org/10.1063/1.338024

Zhang, J.Q., Di, H.S., Wang, X.Y., Cao, Y., Zhang, J.C., Ma, T.J., 2013. Constitutive analysis of the hot deformation behavior of Fe–23Mn–2Al–0.2C twinning induced plasticity steel in consideration of strain. Mater. Des. 44, 354–364.

Zhang, T., Guo, Z.-R., Yuan, F.-P., Zhang, H.-S., 2018. Investigation on the plastic work-heat conversion coefficient of 7075-T651 aluminum alloy during an impact process based on infrared temperature measurement technology. Acta Mech. Sin. 34. https://doi.org/https://doi.org/10.1007/s10409-017-0673-8

APPENDIX A: T. Rahmaan, A. Abedini, C. Butcher, N. Pathak, and M.J. Worswick, Investigation into the shear stress, localization and fracture behaviour of DP600 and AA5182-O sheet metal alloys under elevated strain rates, International Journal of Impact Engineering, Vol. 108, pp. 303-321, 2017.

Accessible through the link below as well as the University of Waterloo's

Institutional Repository (UW Space)

https://www.sciencedirect.com/science/article/pii/S0734743X17301331

APPENDIX B: T. Rahmaan, J. Noder, A. Abedini, P. Zhou, C. Butcher, M.J. Worswick, Anisotropic plasticity characterization of 6000- and 7000-series aluminum sheet alloys at various strain rates, International Journal of Impact Engineering, Vol. 135, 103390, 2020.

Accessible through the link below as well as the University of Waterloo's

Institutional Repository (UW Space)

https://www.sciencedirect.com/science/article/pii/S0734743X18312399

APPENDIX C: T. Rahmaan, C. Butcher, S. Kim, M.J. Worswick, Characterization and prediction of fracture in 6000- and 7000-series aluminum alloy sheet under various stress states, Thin-Walled Structures, Vol. 173, 108958, 2022.

Accessible through the link below as well as the University of Waterloo's

Institutional Repository (UW Space)

https://www.sciencedirect.com/science/article/abs/pii/S0263823122000428

APPENDIX D: T. Rahmaan, C. Butcher, K. Daun, M.J. Worswick, High strain rate fracture characterization of AA7075-T6 sheet metal alloy under various stress states, Submitted to the International Journal of Impact Engineering, 2022.

Accessible through the University of Waterloo's Institutional Repository (UW Space)

APPENDIX E: Additional publications stemming from this research

A. Abedini, C. Butcher, T. Rahmaan, and M.J. Worswick, Evaluation and calibration of anisotropic yield criteria in shear loading: Constraints to eliminate numerical artefacts, International Journal of Solids and Structures, Vol. 151, pp 118-134, 2018.

T. Rahmaan, P. Zhou, C. Butcher, P. Zhou, M.J. Worswick, Strain rate and thermal softening effects in shear testing of AA7075-T6 sheet, EPJ Web of Conferences, 183: 02037, 2018.

J. Noder, A. Abedini, T. Rahmaan, S. DiCecco, C. Butcher, M.J. Worswick, An experimental and numerical investigation of non-isothermal cup drawing of a 7xxx-T76 aluminum alloy sheet, IOP Conf. Series: Materials Science and Engineering, 418: 012019, 2018.

S. Kim, K. Omer, T. Rahmaan, C. Butcher, M.J. Worswick, Effects of die quench forming on sheet thinning and 3-point bend testing of AA7075-T6, AIP Conference Proceedings, 1896: 080015, 2017.

T. Rahmaan, C. Butcher, M.J. Worswick, Constitutive response of AA7075-T6 aluminum alloy sheet in tensile and shear loading, Experimental and Applied Mechanics, 4: 115-122, 2016.

T. Rahmaan, C. Butcher, A. Abedini, M.J. Worswick, Effect of strain rate on shear properties and fracture characteristics of DP600 and AA5182-O sheet metal alloys, EPJ Web of Conferences, 94: 01033, 2015.